UNIVERSITÀ POLITECNICA DELLE MARCHE
SCUOLA DI DOTTORATO DI RICERCA IN INGEGNERIA INDUSTRIALE
CURRICULUM IN INGEGNERIA MECCANICA

Constitutive behaviour identification of anisotropic plasticity using non-linear VFM

Ph.D. Dissertation of:
Attilio Lattanzi

Advisor:
Prof. Marco Rossi

Coadvisor:
Prof. Dario Amodio

Curriculum Supervisor:
Prof. Ferruccio Mandorli

XVI edition - new series

Università Politecnica delle Marche
Scuola di Dottorato di Ricerca in Ingegneria Industriale
Curriculum in Ingegneria Meccanica

Constitutive behaviour identification of anisotropic plasticity using non-linear VFM

Ph.D. Dissertation of:
Attilio Lattanzi

Advisor:
Prof. Marco Rossi

Coadvisor:
Prof. Dario Amodio

Curriculum Supervisor:
Prof. Ferruccio Mandorli

XVI edition - new series

Università Politecnica delle Marche
Scuola di Dottorato di Ricerca in Ingegneria Industriale
Facoltà di Ingegneria
Via Brecce Bianche – 60131 Ancona (AN), Italy

Alla materia che costituisce i miei sogni e le mie aspirazioni,
per la loro pazienza e supporto: la mia famiglia, e te.

Acknowledgments

Although the following dissertation represent an individual work, I could never explore the depths without the guidance and support of a lot of people.

I owe my deepest gratitude to my supervisor Dr. Marco Rossi, who sets up my the qualities required for being a good scientist and engineer. His guidance and cheerful enthusiasm have been an essential source of inspiration. Also, my personal and technical growth could not have happened without the support of my research group at Università Politecnica delle Marche. So, I would like to thank Prof. Marco Sasso, Gianluca Chiappini, Edoardo Mancini and Prof. Dario Amodio for their teachings and the joyous time spent together.

I am deeply grateful to Prof. Frédéric Barlat and all the guys of MML Group at GIFT-Postech, which have taken me with my most sincerely honour during my semester abroad. Their intellectual inputs and spurring insights helped me to push forward my research.

I wish to express my special gratitude to Dr. Sam Coppieters from KU Leuven, who inspected and examined my thesis together with Prof. Barlat: their precious suggestions have been a fundamental improvement to this dissertation.

Ancona, 15th *February 2017*

Attilio Lattanzi

Abstract

The Virtual Fields Method (VFM) is an inverse technique that allows to identify the material parameters of a constitutive model using full-field strain data. In this research activity, the VFM is employed to characterize the anisotropic plasticity behaviour of metals. This aspect, in fact, is particularly important in many industrial processes such as sheet metal stamping and metal forming in general. So, the VFM is used accordingly with its formulation for the finite deformation theory. In such application, the identification of material parameters is performed through an iterative procedure; in this, the algorithm for the integration of constitutive equations has significant effects on accuracy and computational time. A fast computational method for stress reconstruction from strain data in general plasticity is formalized and validated. This algorithm, called Direct Method, is implemented in the VFM and will be exploited for all the analysis given below.

The VFM, and the inverse methods in general, allow to consider heterogeneous strain fields for the identification, in order to introduce as much informations about the material as possible. This, also, leads to the development on new experimental procedures capable of collecting a large amount of material data. Employing the Digital image Correlation (DIC) as main tool for the full-field measurement, new experimental procedures are proposed, facing such problems as the optimization of specimens for the elasto-plastic behaviour characterization, the evaluation of the volume displacement from surface DIC measurements, the characterization of sheet metals through-thickness behaviour at large strains. The methodology applied relies on both numerical analysis and experimental validation.

The last part is focused on the identification of the material parameters of an anisotropic plasticity model, the YLD2000-2D yielding criterion. The results coming from the inverse identification by means of VFM are compared with the standard procedure based on the uniaxial test at three material orientations and the equi-biaxial stress state by means of bulge test. This experimental investigation is extended on two AHSS steels, the BH-340 and TRIP-780, widely employed in automotive applications.

Sommario

Il Virtual Fields Method (VFM) è una tecnica di identificazione inversa che permette di calibrare i paramtri di un generico modello costitutivo del materiale, impiegando campi di deformazioni misurati tramite tecniche full-filed. Nel lavoro di ricerca intrapreso, il VFM è utilizzato per la caratterizzazione del comportamento anisotropro del materiale in condizioni di plasticità. Tale aspetto, infatti, è particolarmente rilevante in molte applicazioni industriali come, ad esempio, processi di stampaggio e, più genericamente, di formatura. Dunque, il VFM è utilizzato secondo la sua formulazione per la teoria delle grandi deformazioni. In tali impieghi, l'identificazione dei parametri caratteristici del materiale è realizzata attraverso un processo iterativo; ne consegue che l'algoritmo d'integrazione delle equazioni costitutive adottato ha effetti sostanziali sull'accuratezza dei risultati e sui tempi di calcolo. A tal fine, un nuovo metodo computazionale per la ricostruzione delle tensioni di Cauchy è qui formulato ed analizzato. Grazie alle sue performances computazionali, questo algoritmo, definito Direct Method, costituisce uno degli strumenti fondamentali impiegati nella presente tesi.

Il VFM, e più in generale i metodi inversi, permettono di considerare campi di deformazioni eterogenei ai fini dell'identificazione. Questo ha portato allo sviluppo di nuove procedure sperimentali, capaci di raccogliere un gran numero di informazioni sul comportamento del materiale. L'attività di ricerca si è dunque interessata anche dello studio di nuovi protocolli sperimentali, affrontando tre temi principali: l'ottimizzazione di provini per la caratterizzazione del comportamento elasto-plastico di lamiere, la valutazione del campo di deformazione all'interno del materiale a partire da misure di superficie tramite DIC, la caratterizzazione del comportamento lungo lo spessore di laminati sottili. La metodologia seguita si basa sull'impiego di analisi numeriche non-lineari agli Elementi Finiti come strumento di sviluppo e la successiva verifica sperimentale.

La parte finale è dedicata all'identificazione dei parametri costitutivi di un modello di plasticità anisotropa complessa, lo YLD2000-2D. I risultati derivanti la calibrazione effettuata con il VFM sono confrontati con la procedura standard, la quale prevede l'impiego di dati da prove uniassiali a tre differenti orientazioni del materiale e relativi alla condizione di equi-biassialità, ottenuta tramite bulge test. Tale attività sperimentale è applicata a due acciai AHSS impiegati nell'industria dell'automotive: il BH-340 ed il TRIP-780.

Contents

1 Introduction 1

1.1 Introduction 1

2 Plasticity theoretical framework 3

2.1 Introduction 3

2.2 Fundamentals of plasticity 3

2.2.1 The Yield Function 4

2.2.2 Plastic Flow rule 6

2.2.3 Consistency Condition 6

2.2.4 Hardening rule 7

2.3 Anisotropic Plasticity Criteria 7

2.3.1 Hill48 material model 7

2.3.2 YLD2000-2D material model 8

3 The Direct Method for stress integration 11

3.1 Introduction 11

3.2 Explicit and implicit schemes for elasto-plastic constitutive equations 12

3.2.1 Cutting Plane algorithm 14

3.2.2 Multi-stage return mapping algorithm 16

3.3 The Direct method for stress integration 20

3.3.1 Numerical implementation 23

3.3.2 Validation on numerical data 27

4 The Virtual Fields Method for large strain problems 41

4.1 Introduction 41

4.2 The Principle of Virtual Work for finite strains 42

4.3 The non-linear Virtual Fields Method 44

5 Development and validation of new testing protocols 45

5.1 Introduction 45

5.2 Evaluation of volume displacement from surface DIC measurement 47

5.2.1 Numerical validation 50

5.2.2 Application on experimental data 54

5.3 Test for sheet metals through-thickness behaviour characterization 58
5.3.1 FE analysis on numerical 2D model 59
5.3.2 Synthetic images generation and DIC measurement . . . 62
5.3.3 Application of non-linear VFM 64
5.3.4 Assessment of specimen width 68
5.4 Validation of experimental set-up simulator for specimen optimization 73
5.4.1 Simulated experiment and results 75
5.4.2 Experimental validation 77

6 Identification of anisotropic plasticity models: the YLD2000-2D 85
6.1 Introduction 85
6.2 Calibration of BH-340 steel 88
6.2.1 Standard calibration procedure 88
6.2.2 VFM identification procedure 92
6.2.3 Comparison of identification results 96
6.3 Calibration of TRIP-780 steel 99
6.3.1 Standard calibration procedure 99
6.3.2 VFM identification procedure 101
6.3.3 Comparison of identification results 106

7 Conclusions and future developments 109
7.1 The Direct Method for integration of elasto-plastic constitutive equations 110
7.2 Development and validation of new experimental protocols . . . 111
7.3 Identification of anisotropic plasticity models: the YLD2000-2D 114

List of Figures

2.1 Schematic of hardening/softening curve. 4

3.1 Return path according to the Cutting Plane algorithm. 16
3.2 Graphical representation of multi-stage return mapping method. 18
3.3 Yield surface representation in the π-plane. 21
3.4 Flow diagram for implementation of direct stress integration method. 24
3.5 Specimen geometry. Dimensions are in mm. 28
3.6 Comparison between reconstructed stresses, equivalent plastic strain and resulting data from FEA at integration point A. . . 29
3.7 Comparison between reconstructed stresses, equivalent plastic strain and resulting data from FEA at integration point B. . . 30
3.8 Cauchy stress comparison for notched specimen with material orientation at 0°, modelled using Hill48. 31
3.9 Cauchy stress comparison for notched specimen with material orientation at 30°, modelled using YLD2000-2D. 32
3.10 Interal Work evaluation and comparison using Hill48 model at different R_{th} values. 33
3.11 Interal Work evaluation and comparison using YLD2000-2D model. 34
3.12 Stress integration at different strain increments, using Hill48 material model. 35
3.13 Stress integration at different strain increments, using YLD2000-2D material model. 35
3.14 Stress integration from strain field affected by noise, using Hill48 material model. 36
3.15 Stress integration from strain field affected by noise, using YLD2000-2D material model. 37
3.16 Computational time evaluation using Matlab®. 38
3.17 Computational time evaluation using Fortran95 language for Hill48. 39

4.1 Kinematic of material body finite strains. 42

5.1 Application of the IGM method for cylindrical geometry. 49
5.2 FE models used in numerical validation. The central cross section reveals the strain localization within the necking zone. 51

5.3 Comparison of reconstructed internal points with the FEA reference data for the cylindrical specimen. 51

5.4 Comparison of the strain field evaluated in the necking zone of specimen with the reconstruction method. Two paths in the central section and a path in the axial direction are depicted. . 53

5.5 Experimental set-up with 360° DIC acquisition equipment. . . 54

5.6 Vertical displacement obtained from 360°-DIC measurement. . 55

5.7 Three-dimensional reconstruction of the deformation of the cylindrical specimen and pictures of the specimen. 57

5.8 Strain distribution across two orthogonal cross sections of the specimen showing the strain concentration at its centre. 57

5.9 Plots of the principal strain along three different radial paths in the central section of the specimen. 58

5.10 Experimental apparatus and specimen specifications for metal sheet through-thickness testing used in FEA. Dimensions are in mm. 60

5.11 Results of FEA simulation, calculated with respect to global reference system. 62

5.12 Synthetic reference and deformed images. 64

5.13 Strain fields comparison between FEA data and DIC measurement. 65

5.14 Sheet metal through-thickness test schematic view. 66

5.15 Schematic view of the selected nodes at three different levels of specimen width. 69

5.16 Stress comparison for 5 mm width specimen. 70

5.17 Stress comparison for 2 mm width specimen. 71

5.18 Stress comparison for 1 mm width specimen. 72

5.19 Optimization process flowchart. 74

5.20 Specimen geometry and design variables. Dimensions are expressed in mm. 76

5.21 Resulting identification error for all 50 configurations with datasets coming from FEA and simulated experiments. 77

5.22 Comparison of predicted stress-strain curves from geometries having the best identification performances. 78

5.23 Equivalent plastic strain distribution for the three geometries. . 79

5.24 Details of notched specimens used for the experimental validation. 80

5.25 Results from uniaxial tensile test on AISI304 81

5.26 Overview of experimental activity results. 83

5.27 Statistical comparison in terms of average stress-strain curve and standard deviation trends for the three geometries considered. 84

6.1 Specimen geometry for VFM identification (units: mm). 86

6.2 Schematic of the reference frame used in the VF definition. . . 86
6.3 Uniaxial test experimental setup. 88
6.4 BH-340 uniaxial tensile test results. 89
6.5 Bulge test experimental setup. 90
6.6 BH-340 bulge test pressure and measured principal strains. . . 91
6.7 BH-340 equi-biaxial stress-strain curve and R-value. 91
6.8 Flow stress trends at different Plastic Work for BH-340. 93
6.9 BH-340 flow stresses plot in the π-plane. 93
6.10 Anisotropy coefficients and predicted tricomponent yield surface for BH-340 steel. 94
6.11 Example of measured strain fields on BH-340 specimens' surfaces at different material orientations. 95
6.12 Effects of smoothing application on strain fields for BH-340 specimen oriented at 90° with respect to RD. The reference frame is local. 95
6.13 Comparison of predicted yield surfaces from different calibration procedures for BH-340 97
6.14 Comparison of anistropy of uniaxial yield stress and R-value for BH-340. 98
6.15 TRIP-780 uniaxial tensile test results. 100
6.16 Bulge test results for TRIP-780 102
6.17 Flow stress trends at different Plastic Work for TRIP-780. . . . 103
6.18 TRIP-780 low stresses plot in the π-plane. 103
6.19 Anisotropy coefficients and predicted tricomponent yield surface for TRIP-780 steel. 104
6.20 Example of measured strain fields on TRIP-780 specimens' surfaces at different material orientations. The reference frame is local. 105
6.21 Effects of smoothing application on strain fields for TRIP-780 specimen oriented at 90° with respect to RD. 105
6.22 Comparison of predicted yield surfaces from different calibration procedures for TRIP-780 107
6.23 Comparison of anistropy of uniaxial yield stress and R-value for TRIP-780. 107

List of Tables

3.1 FE model characteristics and constitutive parameters used. . . 28

5.1 Mesh details and material parameters used in the finite element model. 50
5.2 Number of points used in the various steps of the reconstruction process. 56
5.3 FE model constitutive parameters. 61
5.4 Identification results via non-linear VFM for sheet metal through-thickness test. 68
5.5 Lankford parameters evaluation and Swift hardening law characterization for AISI304. 80

6.1 Summary of uniaxial test results for BH-340. 88
6.2 Settings used for the DIC measurements on BH-340 uniaxial and bulge tests, and performance analysis. 89
6.3 Bulge test equipment specifications. 90
6.4 Input data for YLD2000-2D calibration on BH-340 steel. 92
6.5 Settings used for the DIC measurements and performance analysis on BH-340 notched specimens. 96
6.6 Identified YLD2000-2D coefficients with non-linear VFM for BH-340. 97
6.7 Comparison of predicted flow stress at the equi-biaxial stress state for BH-340. 99
6.8 Settings used for the DIC measurements on TRIP-780 uniaxial and bulge tests, and performance analysis. 100
6.9 Summary of uniaxial test results for TRIP-780. 101
6.10 Input data for YLD2000-2D calibration on TRIP-780 steel. . . 101
6.11 Settings used for the DIC measurements and performance analysis on TRIP-780 notched specimens. 104
6.12 Identified YLD2000-2D coefficients with non-linear VFM for TRIP-780. 106
6.13 Comparison of predicted flow stress at the equi-biaxial stress state for TRIP-780. 108

Chapter 1

Introduction

1.1 Introduction

In the engineering design process the conception of a product crucially relies on the correct knowledge of material behaviour and its characterization. In fact, for any application, the material has to achieve the required functions, becoming an essential stage of the project development [1]. However, the material response can be extremely various and heterogeneous, and among the years an enormous number of mathematical models has been introduced. Obviously, the accuracy of the mechanical behaviour prediction depends first on the employed model and, second, on its calibration.

Looking into a specific problem, sheet metals forming represents a widely diffused industrial process. In particular, under plastic deformation sheet metals often exhibit an anisotropic behaviour, mainly due to its texture and texture evolution during the plastic deformation. In fact, the rolling manufacturing process gives to blank sheets preferential orientations, which can have a relevant influence on the whole sheet metal forming process. Nowadays, being able to correctly simulate the behaviour of sheet metals through the Finite Element Analysis (FEA) is a fundamental task for the process design. Thereby, several anisotropic plasticity models are successfully implemented, each of them requiring the identification of a set of constitutive parameters.

In the field of experimental mechanics many techniques have been studied to face the issue of material properties identification. The common approach, essentially, considers to produce an homogeneous stress state, which is basically deduced from the measured load. However, in the recent years, the diffusion of full-field measurement techniques was followed by the development of methods to characterize inversely even complex material models. Many inverse methods can be found in literature [2, 3], the most widespread ones able to retrieve the material parameters from a full-field measurement are the Finite Element Model Updating (FEMU), and the Virtual Fields Method (VFM) [4]. In particular, the latter one offers the main advantage of higher computational efficiency compared to FEMU, since no Finite Element simulations must be iteratively performed to reach the identification. This aspects, in fact, becomes particularly important in non-linear problems applications.

The purpose of this thesis and research activity in general, thus, is to deeply analyse benefits and drawbacks of non-linear VFM application to identify the metals anisotropic plasticity behaviour.

Anyway, this Introduction Chapter does not have the aim to anticipate and summarize the contents of this thesis work, but it represents the "bunch of keys" necessary to open each chapter's "door". Hence, no more general informations about the state of art will be reported here, since each chapter contains its introduction framework.

Chapter 2 illustrates the indispensable theoretical basis of Plasticity on which this thesis relies. Such fundamental concepts of Yield Surface, Flow Rule, Hardening Rule are provided, so that in Chapter 3 they will be exploited to formalise a new method for elasto-plastic integration of constitutive equations. The *Direct Method* for stress state reconstruction is, then, validated and compared to other traditional stress integration algorithms. In particular, the Direct Method is particularly suitable to be implemented with the VFM technique, whose formulation for non-linear problems is described in Chapter 4. VFM, and inverse identification techniques in general, represent a powerful tools thanks to their ability to employ a large amount of material data. Thereby, they inspire new ideas for experimental procedures development. So, Chapter 5 introduces new experimental protocols to be employed in inverse calibration of material models. All these concepts converge in the Chapter 6, where the VFM is applied to calibrate the YLD2000-2D material model. This also represents the main experimental part, where the VFM identification results are compared with the traditional calibration procedure on two AHSS steels.

Chapter 2

Plasticity theoretical framework

2.1 Introduction

From its early origin traced back to a series of studies by Tresca [5] in 1872, which was followed by the observations of Bauschinger in 1886 and von Mises [6] in 1928, theory of plasticity is enriched with significant scientific inputs and experiences among the year, becoming nowadays a well-established and mature topic of solid mechanics. Research community has reached a deep understanding of governing equations, and, in the last decades, the increasing computational power in numerical simulations made possible to solve also highly complex problems.

The aim of this Chapter, thus, is to make an essential overview on elasto-plastic problem, furnishing the basis of the theoretical framework on which the following Chapters of this thesis rely. However, plasticity represents an incredibly wide research area, and the dissertation will be limited to the fundamental concepts of rate-independent plasticity like yielding criterion, plastic flow rule hardening behaviour and anisotropic plasticity. More complete treatise of this topic can be found in [7, 8, 9, 10].

2.2 Fundamentals of plasticity

One of the simplest way to determine the stress-strain relation of an elasto-plastic material is represented by the uniaxial loading/unloading test, whose general results are reported in Figure 2.1. Starting from zero stress level (point O), the material point is loaded until point A describing a linear path. If the same material point is unloaded from A to O and again loaded to A, it follows the same path without exhibiting memory of the previous load. Thus, the material does not accumulate a permanent deformation, and remains into the elastic range.

Now, the load increase exceeding point A and arriving to point B through a non-linear path. Unloading again to point C, the material shows a memory in

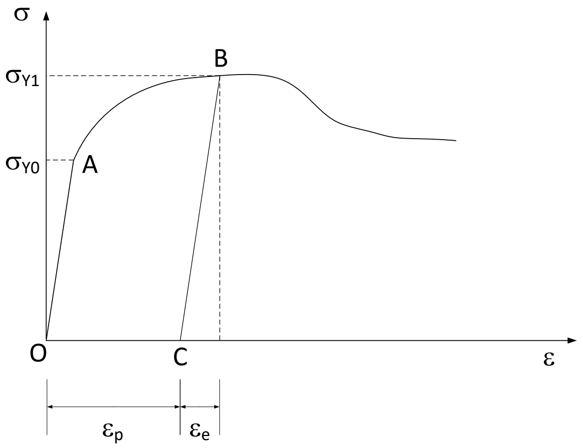

Figure 2.1: Schematic of hardening/softening curve.

the elasto-plastic regime keeping a permanent deformation. Thereby, the total strain can be divided in two parts: the elastic and plastic.

$$\varepsilon = \varepsilon_e + \varepsilon_p \, . \tag{2.1}$$

So, basically, when material behaviour changes from elastic to elasto-plastic, it *yields*. In this case the material point yields first at point A, and successively at point B, whose stresses σ_{Y0} and σ_{Y1} are obviously called yield stresses. Moreover, looking at the curve, when the yield stress increase, material exhibit strain hardening, while it is called strain softening in case of decreasing yield stress trend. In general, this behaviour is mathematically considered through the *hardening rule*. Also a third case can be distinguished when the yield stress remains constant, and it is called perfectly-plastic behaviour.

2.2.1 The Yield Function

The same conclusions can be extended to the multiaxial loading case, where the yield stress scalar quantity becomes a surface function of the whole stress tensor. In other words, if we consider a Cartesian reference system where principal stresses are taken as coordinates, the yield point can be represented according to the stress state with which is experimentally obtained. Displaying the yielding points coming from different loading conditions (i.e. pure shear, biaxial stress state, traction-torsion, etc. [11, 12]), they can shape a surface that can be described by a certain mathematical function: the *yield surface*.

Since the uniform hydrostatic stress accordingly has no influence on yielding, the yielding surface can be expressed in function of the second and third deviatoric stress common invariants assuming the following general form:

$$\phi(J_2, J_3) = const\,. \tag{2.2}$$

As already observed, elasto-plastic materials behaviour has memory of its loading history, and the material state must contain this kind of informations. Thus, the plastic internal variables ξ_i are introduced so that the constitutive equations can be expressed as follows:

$$\boldsymbol{\sigma} = \boldsymbol{\sigma}(\boldsymbol{\varepsilon}, \xi_i) \tag{2.3}$$

Practically, ξ_i can represent a scalar parameter, a second order tensor, etc. Usually these internal plastic variables ξ_i can represent an hardening variable that defines the size of yield surface, or anisotropic plasticity parameters which consider the texture of material, or even variables connected to back stress. Thereby, it is possible to define the *yield function* such that:

$$\begin{cases} \phi(\boldsymbol{\sigma}, \xi_i) > 0 & \text{outside the surface} \\ \phi(\boldsymbol{\sigma}, \xi_i) = 0 & \text{on the surface} \\ \phi(\boldsymbol{\sigma}, \xi_i) < 0 & \text{inside the surface} \end{cases} \tag{2.4}$$

where the domain inside yield surface is purely elastic. The outer domain is actually inaccessible by the material state.

Now, let's consider a stress state that lies on the yield surface ($\phi(\boldsymbol{\sigma}) = 0$). In order to observe how the yield surface behaves when the material point is exposed to variable loading conditions, a scalar quantity l called *loading index* is introduced, which is defined as the scalar product between the rate of stress $d\boldsymbol{\sigma}$ and the normal $\hat{n}$ to the yield surface at the current stress point:

$$l = d\boldsymbol{\sigma}\,\hat{n} = d\boldsymbol{\sigma}\,\frac{\partial \phi}{\partial \boldsymbol{\sigma}} \tag{2.5}$$

This can help us to define a loading/unloading criterion such as the event can be distinguished in:

$$\begin{cases} l > 0 & \text{elasto-plastic loading} \\ l = 0 & \text{neutral loading (elastic)} \\ l < 0 & \text{unloading (elastic)} \end{cases} \tag{2.6}$$

This principle is particularly important for the integration of elasto-plastic constitutive equations, since it helps to know whether the updated stress will rely inside the yield surface (unloading) or the yield locus is exceeded.

2.2.2 Plastic Flow rule

Up until this point the necessary conditions to initiate yielding have been reported. Therefore, what it is to be analysed regards what will happens when loading continues and plastic flow occurs.

Considering the stress-strain relation is rate-independent, the plastic strain rate $d\boldsymbol{\varepsilon}_p$ may be defined as:

$$d\boldsymbol{\varepsilon}_p = f(\boldsymbol{\sigma}, \xi_i) \tag{2.7}$$

where f represents an homogeneous and order 1 function that does not have dependency on stress rate $d\boldsymbol{\sigma}$, and the plastic internal variables ξ_i are related to the hardening behaviour of material. In particular, the function f represents magnitude and direction of plastic strain rate. So, the direction of can be derived form the potential function ψ, also know as *plastic potential*; viz.:

$$d\boldsymbol{\varepsilon}_p = d\lambda \frac{\partial \psi(\boldsymbol{\sigma}, \xi_i)}{\partial \boldsymbol{\sigma}} \tag{2.8}$$

the parameter $d\lambda$ is also called *plastic consistency parameter*, and is necessary positive during plastic flow because deformation is an irreversible phenomenon. Define the normal to plastic potential surface as $\hat{r} = \dfrac{\partial \psi}{\partial \boldsymbol{\sigma}}$, it follows:

$$d\boldsymbol{\varepsilon}_p = d\lambda\, \hat{r}\,. \tag{2.9}$$

Eq. 2.9 indicates that there is a relation between the direction of plastic flow and the plastic potential ψ, called *flow rule.* In addition, when the plastic potential is equal to the yield function $\psi = \phi$, also $\hat{r} = \hat{n}$ the flow rule is defined as *associated*, otherwise, when $\psi \neq \phi$ and consequently $\hat{r} \neq \hat{n}$, it is called *non-associated* flow rule.

2.2.3 Consistency Condition

When a material point is loaded, the stress point moves away from the yield locus, going outward the yield surface in case of hardening behaviour (or inward for softening materials). However, the material point cannot be defined in the outer domain of yield surface, therefore the yield surface must be modified. In other words, it can change its shape, size or location so that the updated point is still on the yield surface. This requirement represents an important basic principle of plasticity theory and is called *Consistency Condition.*

Assuming associated Flow Rule, basically Consistency Condition can be mathematically expressed as:

$$d\phi(\boldsymbol{\sigma}, \xi_i) = 0 \tag{2.10}$$

that, according to the chain rule, becomes:

$$\frac{\partial \phi}{\partial \boldsymbol{\sigma}} : d\boldsymbol{\sigma} + \frac{\partial \phi}{\partial \xi_i} : d\xi_i = 0 \tag{2.11}$$

2.2.4 Hardening rule

The way how yield surface modify due to the loading increment is regulated by the *hardening rule*. Thereby, the hardening behaviour is classified as *isotropic* when the yield surface expands (or contract) uniformly in all directions, keeping fixed its centre during the loading path.

On the contrary, when the yield surface maintains its shape unmodified but translates its centre, hardening rule is defined *kinematic*. This approach is typically used, for instance, in pressure-dependent plasticity materials such as soil, or to predict the Bauschinger effect introducing a back stress tensor function only of pure deviatoric stresses. Several formulations of kinematic hardening rules can be founded in literature, as the classical Prager's rule [13, 14] or the Chaboche model for non-linear kinematic hardening [15].

However, kinematic hardening rules represents just a small classification of the larger group of *Anisotropic* hardening models, which includes for example combined isotropic-kinematic hardening, or two yield surfaces plasticity model [16], or dislocation-based hardening model [17].

2.3 Anisotropic Plasticity Criteria

2.3.1 Hill48 material model

The first definition of anisotropic yield criterion can be traced in 1928, when von Mises proposed a yield function based on single crystal plasticity. In 1948, Hill formulated a quadratic yield function as generalization of the isotropic von Mises criterion, assuming that the material shows anisotropic behaviour on three symmetry planes. This criterion [18], commonly called Hill48, is still widely used in metal sheet forming applications thanks to its simplicity. Material parameters of Hill48 model can be calibrated either employing directional R-values [19] from tree different material texture orientations or directional flow stresses (0°, 45°, 90° and equi-biaxial stress state).

The R-value based Hill48 function can be expressed as follows:

$$\begin{aligned} 2\phi(\boldsymbol{\sigma}) =& f(\sigma_{yy} - \sigma_{zz}) + g(\sigma_{zz} - \sigma_{xx}) + h(\sigma_{xx} - \sigma_{yy}) \\ &+ 2l\sigma_{xz}^2 + 2m\sigma_{yz}^2 + 2n\sigma_{xy}^2 = 1 \end{aligned} \tag{2.12}$$

under the assumption that the material presents only normal anisotropy, the six coefficients can be obtained from the ratio between the transverse strain and the through-tickness strain from uniaxial tensile test. So:

$$\begin{aligned} &f = \frac{1}{1+R_0}\frac{R_0}{R_{90}}; \quad g = \frac{1}{1+R_0}; \quad h = \frac{R_0}{1+R_0}; \\ &l = \frac{3}{2}; \quad m = \frac{3}{2}; \quad n = \left(\frac{1}{2} + R_{45}\right)\frac{R_0}{R_{90}}. \end{aligned} \tag{2.13}$$

Due to its quadratic order, the Hill48 anisotropy function can predict only two or four ears in the deep drown cup test. However, albeit the Hill48 is one of the simplest and most user friendly anisotropic criteria, it has some relevant drawbacks. In fact, and R-value-based and stress-based Hill48 versions are not accurate to respectively predict anisotropy of flow stress and the Lankford parameter R.

2.3.2 YLD2000-2D material model

The YLD2000-2D yielding criterion [20] describes the anisotropic behaviour of material by means of the application of linear transformations on two isotropic functions of deviatoric stress tensor $\boldsymbol{s}$. Thus the yield criterion is defined as follows:

$$\phi = \phi' + \phi'' = 2\bar{\sigma}^a \tag{2.14}$$

where the two functions can be expressed as:

$$\phi' = |X'_1 - X'_2|^a \tag{2.15}$$

$$\phi'' = |2X''_2 + X''_1|^a + |2X''_1 + X''_2|^a \tag{2.16}$$

the exponent a depends from the crystal structure of material, and regulates the curvature of yield surface vertices. In fact, convexity is ensured when $a \geq 1$. Usually the a value is equal to 6 in case of BCC materials or 8 for FCC materials, as explained by Logan and Hosford in [21]. $\bar{\sigma}$ indicates the equivalent stress. Observing the two functions, the X'_j and X''_j (with $j = 1, 2$) represent respectively the principal values of $\boldsymbol{X}'$ and $\boldsymbol{X}''$ tensors. Indicating with x the RD and y the TD directions, such tensors are defined as linear transformation of stress deviator:

$$\begin{Bmatrix} X'_{xx} \\ X'_{yy} \\ X'_{xy} \end{Bmatrix} = \begin{bmatrix} C'_{11} & C'_{12} & 0 \\ C'_{21} & C'_{22} & 0 \\ 0 & 0 & C'_{33} \end{bmatrix} \begin{Bmatrix} s_{xx} \\ s_{yy} \\ s_{xy} \end{Bmatrix} \tag{2.17}$$

and

$$\begin{Bmatrix} X''_{xx} \\ X''_{yy} \\ X''_{xy} \end{Bmatrix} = \begin{bmatrix} C''_{11} & C''_{12} & 0 \\ C''_{21} & C''_{22} & 0 \\ 0 & 0 & C''_{33} \end{bmatrix} \begin{Bmatrix} s_{xx} \\ s_{yy} \\ s_{xy} \end{Bmatrix} \tag{2.18}$$

Moreover, for simplicity these equations can be applied to the Cauchy stress tensor $\boldsymbol{\sigma}$ through $\boldsymbol{T}$:

$$\boldsymbol{X}' = \mathbf{C}'\boldsymbol{s} = \mathbf{C}'\mathbf{T}\boldsymbol{\sigma} = \mathbf{L}'\boldsymbol{\sigma} \tag{2.19}$$

$$\boldsymbol{X}'' = \mathbf{C}''\boldsymbol{s} = \mathbf{C}''\mathbf{T}\boldsymbol{\sigma} = \mathbf{L}''\boldsymbol{\sigma} \tag{2.20}$$

with

$$\mathbf{T} = \begin{bmatrix} \frac{2}{3} & -\frac{1}{3} & 0 \\ -\frac{1}{3} & \frac{2}{3} & 0 \\ 0 & 0 & 1 \end{bmatrix} \tag{2.21}$$

The two tensors $\mathbf{L}'$ and $\mathbf{L}''$ are function of eight independent coefficients α_i:

$$\mathbf{L}' = \frac{1}{3} \begin{bmatrix} 2\alpha_1 & -2\alpha_1 & 0 \\ 2\alpha_2 & 2\alpha_2 & 0 \\ 0 & 0 & 3\alpha_7 \end{bmatrix} \tag{2.22}$$

$$\mathbf{L}'' = \frac{1}{9} \begin{bmatrix} 8\alpha_5 - 2\alpha_3 - 2\alpha_6 + 2\alpha_4 & -4\alpha_6 - 4\alpha_4 - 4\alpha_5 + \alpha_3 & 0 \\ -4\alpha_3 - 4\alpha_5 - 4\alpha_4 + \alpha_6 & 8\alpha_4 - 2\alpha_6 - 2\alpha_3 + 2\alpha_5 & 0 \\ 0 & 0 & 9\alpha_8 \end{bmatrix} \tag{2.23}$$

It is worth noting that when all α_i coefficients are equal to 1 and the exponent $a = 2$ the function reduces to the isotropic von Mises case. Calibration of these anisotropy coefficients requires eight input data from both flow stresses and R-value Lankford parameters. These inputs are retrieved experimentally from uniaxial tensile test at three directions with respect to the rolling direction (RD) (0°, 45°, 90°) and from balanced biaxial stress state, which can be achieved through hydraulic bulge test or biaxial tensile test on cruciform specimens. However, if the R-value from equi-biaxial condition is not available, it can be predicted with another yield function, as YLD96 for example, or assuming that $L''_{12} = L''_{21}$.

The YLD2000-2D demonstrates to be a very robust yield criterion in several application, resulting, also, successfully implemented for Finite Element Analysis [22, 23, 24] and inverse methods [25, 26].

Chapter 3

The Direct Method for the integration of elasto-plastic constitutive equations

3.1 Introduction

The computation of the stress field from the strain history is a well-known problem in elasto-plasticity. The stress depends in a non-linear way on the strain history and, in general, does not exist a closed form solution to obtain the stress from the strain. The problem is tackled using numerical algorithms, which often express the rate of stress and the hardening variables depending on the rate of strains. So, in mathematical terms, it represents an initial value problem that is generally structured as follows:

$$\dot{y}(t) = f[y(t)]\,; \quad t \in [0, T] \tag{3.1}$$

$$y(0) = y_n\,; \tag{3.2}$$

where f is a smooth function and t is time. The aim is to find:

$$y_{n+1}(t + \Delta t) = y_n + \Delta y\,. \tag{3.3}$$

Numerically, the exact value of y_{n+1} is approximated as:

$$y_{n+1} = y_n + f(y_{n+h})\,\Delta t \tag{3.4}$$

$$y_{n+h} = h\,y_{n+1} + (1-h)y_n \tag{3.5}$$

with $h \in [0, 1]$ represents a scalar parameter. Eq. 3.5 is also called *generalized midpoint rule*, and, depending on the value of h, several numerical integration algorithms can be generated. Among them, when $h = 0$ the equation displays the well known *Euler Forward* method (explicit), while $h = 1$ indicates the *Euler Backward* scheme (implicit) [8, 9].

Generally, in the context of inverse characterization problems, implicit integration algorithms are predominantly implemented due to their unconditional stability. These algorithms usually employ the Newton-Raphson method to integrate the constitutive relations, which requires a certain amount of iterations to reach the convergence. This aspect, in fact, is particularly relevant in the case of non-linear VFM identification method, that is intrinsically an iterative procedure. For this reason, a new computational algorithm (Direct Method) capable of integrate directly the plasticity constitutive equation is introduced.

In this Chapter, therefore, the first Section is dedicated to an essential overview on the widely diffused algorithms for the integration of elasto-plastic constitutive equations, reporting the basic difference between explicit and implicit strategies [27]. The dissertation continues focusing on some traditional implicit algorithms, like the Cutting Plane algorithm [28] and the Potential Residuals [29, 30, 22], implemented in such applications like FEA and inverse methods.

The second Section, instead, is addressed to formalise and discuss a new method for stress integration in inverse identification applications, called Direct Method. Here, the algorithm performances in terms of accuracy of stress calculation for the two anisotropic plasticity material described in Section 2.3 are discussed, making a comparison with FEA data. Secondly, also computational time are evaluated through a benchmark in two programming languages.

3.2 Explicit and implicit schemes for elasto-plastic constitutive equations

As already observed, the Consistency Condition, which states that the loaded material point must relies inside the yield function domain, can be written as follows according to the chain rule:

$$d\phi(\boldsymbol{\sigma}, \xi_i) = \frac{\partial \phi}{\partial \boldsymbol{\sigma}} d\boldsymbol{\sigma} + \frac{\partial \phi}{\partial \xi_i} d\xi_i = 0\,; \tag{3.6}$$

Since the aim is to determine the plastic multiplier $d\lambda$, let introduce the stress increment as function of elastic strain increment $d\boldsymbol{\varepsilon}_e$:

$$d\boldsymbol{\sigma} = \boldsymbol{C}_e\, d\boldsymbol{\varepsilon}_e = \boldsymbol{C}_e(d\boldsymbol{\varepsilon} - d\boldsymbol{\varepsilon}_p)\,, \tag{3.7}$$

where $\boldsymbol{C}_e$ indicates the Elastic stiffness matrix. The incremental plastic strain can be, moreover, expressed as:

$$d\boldsymbol{\varepsilon}_p = d\lambda \frac{\partial \phi}{\partial \boldsymbol{\sigma}}\,; \tag{3.8}$$

in this way Eq. 3.7 can be rewritten as:

$$d\boldsymbol{\sigma} = \boldsymbol{C}_e \left(d\boldsymbol{\varepsilon} - d\lambda \frac{\partial \phi}{\partial \boldsymbol{\sigma}} \right) \tag{3.9}$$

Consequently, by substituting Eq. 3.9 into Eq. 3.6, the plastic multiplier is determined as:

$$d\lambda = \frac{\dfrac{\partial \phi}{\partial \boldsymbol{\sigma}} \boldsymbol{C}_e \, d\boldsymbol{\varepsilon}}{\dfrac{\partial \phi}{\partial \boldsymbol{\sigma}} \boldsymbol{C}_e \dfrac{\partial \phi}{\partial \boldsymbol{\sigma}} - \dfrac{\partial \phi}{\partial \xi_i}} \tag{3.10}$$

Then, the internal plastic variables increment $d\xi_i$ is introduced as follows:

$$d\xi_i = d\lambda \, h(\boldsymbol{\sigma}, \xi_i) \tag{3.11}$$

where $h(\boldsymbol{\sigma}, \xi_i)$ can be defined as the plastic moduli.

So, once the plastic multiplier $d\lambda$ is determined, according with this theoretical framework the updated state variables at time step $n + \Delta n$ can be easily calculated as:

$$\boldsymbol{\sigma}(n + \Delta n) = \boldsymbol{\sigma}(n) + d\boldsymbol{\sigma} \tag{3.12a}$$

$$\boldsymbol{\varepsilon}_p(n + \Delta n) = \boldsymbol{\varepsilon}_p(n) + d\boldsymbol{\varepsilon}_p \tag{3.12b}$$

$$\xi_i(n + \Delta n) = \xi_i(n) + d\xi_i \tag{3.12c}$$

Such integration scheme is indicated as first-order *Euler Forward* explicit, and is relatively easy to implement. Nonetheless, its main disadvantage is related to its explicit nature, since it is *conditionally stable* [31]. In fact, the forward process do not ensure that The Consistency Condition is satisfied for the submitted strain increment at time $t + \Delta t$, leading the solution to "drift" away from the yield locus.

In implicit problems one of the first algorithm which permits to calculate the stress field from the strain increment is the *Radial Return*, whose first formulation was proposed by Wilkins [32]. However, the Radial Return belong to a wider class known as *Elastic Predictor-Plastic Corrector* algorithms.

Basically, the stress calculation in plastic regime is made considering two phases. In the first phase, the whole strain increment is applied as elastic strain, and the calculated corresponding stress state is defined Elastic Predictor. So, the Elastic Predictor represents a trial stress state, that is corrected applying a certain amount of plastic strain (Plastic Corrector) in order to "relax" the Elastic Predictor onto a suitably updated yield surface. This approach, in fact, makes that the material point must lie on the yielding surface according to the Consistency Condition, and, so, represents a *Backward Euler* method.

Usually, these approaches involve the Newton-Raphson method to reach convergence at the loading step. The Euler Backward overtakes the forward integration problems since it is intrinsically *stable.* For the sake of clarity and to complete this essential overview, here two implicit stress integration schemes are reported: the so called Cutting Plane and Multi-stage return mapping algorithms.

3.2.1 Cutting Plane algorithm

In literature several implicit algorithms facing the integration of elasto-plastic constitutive equations can be found. For instance, [28] reports the so called Cutting-Plane algorithm, which follows the Elastic Predictor-Plastic Corrector approach. The peculiarity is that the yield surface is linearised during the relaxation phase, making a series of straight lines ("cuts") with the plane $\phi = 0$.

$$d\boldsymbol{\varepsilon} = d\boldsymbol{\varepsilon}_e + d\boldsymbol{\varepsilon}_p \tag{3.13a}$$

$$d\boldsymbol{\sigma} = \boldsymbol{C}_e(d\boldsymbol{\varepsilon} - d\boldsymbol{\varepsilon}_p) \tag{3.13b}$$

$$d\boldsymbol{\varepsilon}_p = d\lambda \, \frac{\partial \phi}{\partial \boldsymbol{\sigma}} \tag{3.13c}$$

$$d\xi_i = d\lambda \, h(\boldsymbol{\sigma}, \xi_i) \tag{3.13d}$$

Now, let introduce a specified strain rate $\boldsymbol{d}(t)$, this set of constitutive equations can be split up into the elastic and plastic parts:

$$\begin{array}{lll}
\textit{Elastic} & \textit{Plastic} & \\
d\boldsymbol{\varepsilon} = \boldsymbol{d}(t); & d\boldsymbol{\varepsilon} = d\boldsymbol{\varepsilon}_e + d\boldsymbol{\varepsilon}_p = 0; & (3.14) \\
d\boldsymbol{\sigma} = \boldsymbol{C}_e d\boldsymbol{\varepsilon}; & d\boldsymbol{\sigma} = -\boldsymbol{C}_e d\boldsymbol{\varepsilon}_p; & (3.15) \\
d\boldsymbol{\varepsilon}_p = 0; & d\boldsymbol{\varepsilon}_p = d\lambda \, \dfrac{\partial \phi}{\partial \boldsymbol{\sigma}}; & (3.16) \\
d\xi_i = 0; & d\xi_i = d\lambda \, h(\boldsymbol{\sigma}, \xi_i)\,. & (3.17)
\end{array}$$

In such configuration the response of material is governed by the elastic part, while the inelastic response in "frozen". The material behaviour described by such equations, in fact, represents the actual response when the strain increment is obviously purely elastic, and also reproduces the Elastic Predictor condition, which is the starting point for the integrations of plasticity constitutive equations. In this latter case, according to the Radial Return mapping scheme, the relaxation equations for the stresses and plastic internal variables can be expressed respectively as:

$$d\boldsymbol{\sigma} = -d\lambda \, \boldsymbol{C}_e \, \frac{\partial \phi}{\partial \boldsymbol{\sigma}}; \qquad d\xi_i = d\lambda \, h(\boldsymbol{\sigma}, \xi_i); \tag{3.18}$$

Eq. 3.18 define the Plastic Corrector, which permits to relax the elastically predicted stresses onto a suitably updated yield surface. Since associative flow rule is assumed, the return path is normal to the yield surface, tracking the steepest descent corresponding to the yield function ϕ. For basic material models as von Mises yield surface and isotropic hardening, the return path is easy to determine, otherwise iterative numerical algorithms are usually involved. At every iteration j, The Cutting Plane algorithm considers that the yield surface is linearised around the current values of state variables $\boldsymbol{\sigma}^{(j)}(n+1)$ and $\xi_i^{(j)}(n+1)$, so:

$$\phi^{(j+1)} = \phi^{(j)} + \frac{\partial \phi^{(j)}}{\partial \boldsymbol{\sigma}^{(j)}(n+1)} \Delta \boldsymbol{\sigma}^{(j)} + \frac{\partial \phi^{(j)}}{\partial \xi_i^{(j)}(n+1)} \Delta \xi_i^{(j)} \approx 0 \tag{3.19}$$

on the other hand, the relaxation equations can be discretied as follows:

$$\begin{aligned} \Delta \boldsymbol{\sigma}^{(j)} &= -\Delta\lambda \, \boldsymbol{C}_e \, \frac{\partial \phi^{(j)}}{\partial \boldsymbol{\sigma}^{(j)}(n+1)}; \\ \Delta \xi_i^{(j)} &= \Delta\lambda \, h[\boldsymbol{\sigma}^{(j)}(n+1), \xi_i^{(j)}(n+1)]. \end{aligned} \tag{3.20}$$

$\Delta\lambda$ indicates an incremental plastic parameter, which can be determined combining Eq. 3.19 and Eq. 3.20:

$$\Delta\lambda = \frac{\phi^{(j)}}{\dfrac{\partial \phi^{(j)}}{\partial \boldsymbol{\sigma}^{(j)}(n+1)} \boldsymbol{C}_e \dfrac{\partial \phi^{(j)}}{\partial \boldsymbol{\sigma}^{(j)}(n+1)} - \dfrac{\partial \phi^{(j)}}{\partial \xi_i^{(j)}(n+1)} \, h[\boldsymbol{\sigma}^{(j)}(n+1), \xi_i^{(j)}(n+1)]} \tag{3.21}$$

Then, once $\Delta\lambda$ is calculated and substituted into Eq. 3.20, the updated stress variables are obtained from:

$$\begin{aligned} \boldsymbol{\sigma}^{(j+1)}(n+1) &= \boldsymbol{\sigma}^{(j)}(n+1) + \Delta \boldsymbol{\sigma}^{(j)} \\ \xi_i^{(j+1)}(n+1) &= \xi_i^{(j)}(n+1) + \Delta \xi_i^{(j)}. \end{aligned} \tag{3.22}$$

Starting from the initial conditions given by the Elastic Predictor, the algorithm iteratively updates the state variables until the Plastic Consistency condition is restored. Figure 3.1 depicts the numerical implementation of the Cutting Plane algorithm. At each iteration steps, the updated stress are calculated from the projection of the previous iteration $\boldsymbol{\sigma}^{(j)}(n+1)$ onto a straight "cut" resulting from the linearization of the yield function at $\boldsymbol{\sigma}^{(j)}(n+1)$.

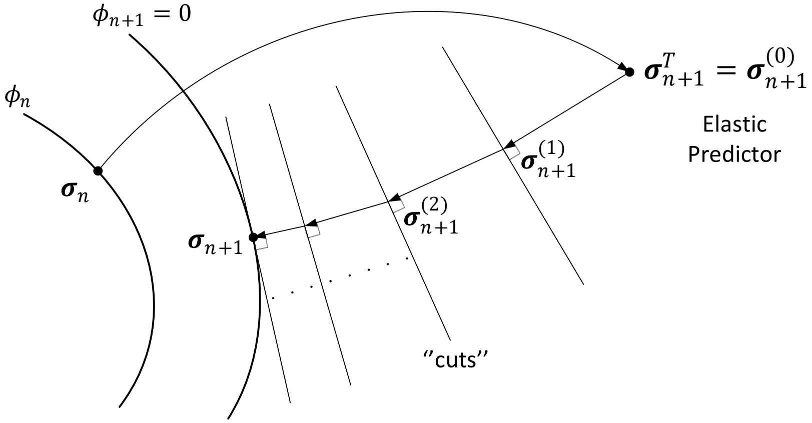
$\phi_{n+1} = 0$
ϕ_n
$\boldsymbol{\sigma}_n$
$\boldsymbol{\sigma}_{n+1}$
$\boldsymbol{\sigma}^T_{n+1} = \boldsymbol{\sigma}^{(0)}_{n+1}$
Elastic Predictor
$\boldsymbol{\sigma}^{(1)}_{n+1}$
$\boldsymbol{\sigma}^{(2)}_{n+1}$
"cuts"

Figure 3.1: Return path according to the Cutting Plane algorithm.

In conclusion, although the Cutting Plane method is usually categorized as implicit algorithm, actually it has both implicit and explicit characteristics, thus is also defined as semi-explicit scheme [33, 34].

3.2.2 Multi-stage return mapping algorithm

An example of fully-implicit algorithm based on Elastic Predictor-Plastic Corrector approach is furnished by Yoon et al. in [29, 30, 22]. This scheme controls the potential residual based on the incremental deformation theory, which permits to separate rotation and deformation by the Polar Decomposition, according to the minimum plastic work path. Moreover, it employs a multi stage return mapping procedure, permitting, thus, to converge even for large strain increments up to 10%. Such method is particularly suitable in case of non-quadratic yield functions, but, compared to the Cutting Plane, requires the calculation of both $\partial\bar{\sigma}/\partial\boldsymbol{\sigma}$ and $\partial^2\bar{\sigma}/(\partial\boldsymbol{\sigma}\,\partial\boldsymbol{\sigma})$. This stress integration scheme is also relevant since here it is exploited to validate and compare the results of the Direct Method for the integration of elasto-plastic constitutive equations.

For the sake of clarity, let consider a generic yielding function ϕ with the assumption of associative plastic flow and isotropic hardening. Indicating with $\bar{\sigma}$ the effective stress, $\sigma_Y = \sigma_Y(\bar{\varepsilon}_p)$ a generic work-hardening law and $\bar{\varepsilon}_p$ the equivalent plastic strain, these hypothesis allows to consider as main plastic internal variable ξ_i the equivalent plastic strain. Thus, the Consistency Condition, which stipulates that the resulting effective stress must rely on the hardening curve, can be written as follows:

$$\phi = \bar{\sigma}(\boldsymbol{\sigma}(n) + \Delta\boldsymbol{\sigma}) - \sigma_Y(\bar{\varepsilon}_p(n) + \Delta\bar{\varepsilon}_p) = 0 \tag{3.23a}$$

where, analogously to the Cutting Plane algorithm:

$$\Delta\boldsymbol{\sigma} = \boldsymbol{C}_e(\Delta\boldsymbol{\varepsilon} - \Delta\boldsymbol{\varepsilon}_p) \tag{3.23b}$$

$$\Delta\boldsymbol{\varepsilon}_p = \Delta\lambda\frac{\partial\bar{\sigma}}{\partial\boldsymbol{\sigma}} \tag{3.23c}$$

In the incremental deformation theory it is worth noting that the equivalent plastic strain increment can be obtained involving an homogeneous first order function represented by the equivalent stress $\bar{\sigma}(\boldsymbol{\sigma}) = \boldsymbol{\sigma}\frac{\partial\bar{\sigma}}{\partial\boldsymbol{\sigma}}$ and the associative flow rule:

$$\Delta\bar{\boldsymbol{\varepsilon}}_p = \frac{\boldsymbol{\sigma} : \Delta\boldsymbol{\varepsilon}_p}{\bar{\sigma}(\boldsymbol{\sigma})} = \frac{\boldsymbol{\sigma} : \Delta\lambda\frac{\partial\bar{\sigma}}{\partial\boldsymbol{\sigma}}}{\bar{\sigma}(\boldsymbol{\sigma})} = \Delta\lambda \tag{3.24a}$$

and:

$$\Delta\boldsymbol{\varepsilon}_p = \Delta\lambda\frac{\partial\bar{\sigma}}{\partial\boldsymbol{\sigma}} = \Delta\bar{\varepsilon}_p\frac{\partial\bar{\sigma}}{\partial\boldsymbol{\sigma}} \tag{3.24b}$$

Introducing the trial stress $\boldsymbol{\sigma}^T = \boldsymbol{\sigma}(n) + \boldsymbol{C}_e\Delta\boldsymbol{\varepsilon}$, according to the Elastic Predictor-Plastic Corrector scheme Eq. 3.23a can be rewritten as:

$$\phi = \bar{\sigma}\left(\boldsymbol{\sigma}^T - \Delta\lambda\boldsymbol{C}_e\frac{\partial\bar{\sigma}}{\partial\boldsymbol{\sigma}}\right) - \sigma_Y[\bar{\varepsilon}_p(n) + \Delta\lambda] = 0 \tag{3.25}$$

that represent a non-linear equation to solve for $\Delta\lambda$ usually employing the Newton-Raphson method. If the strain increment is too large the iterative method cannot reach the solution convergence, hence, the basic idea under the multi-stage return mapping algorithm is to divide the potential residual and to solve each stage of subdivision. In this way, the Eq. 3.25 is expressed for the subdivision k as:

$$\phi_{(k)} = \bar{\sigma}(\boldsymbol{\sigma}^T - \Delta\lambda_{(k)}\boldsymbol{C}_e\boldsymbol{m}_{(k)}) - \sigma_Y[\bar{\varepsilon}_p(n) + \Delta\lambda_{(k)}] = R_{(k)} \tag{3.26}$$

where $\boldsymbol{m} = \frac{\partial\bar{\sigma}}{\partial\boldsymbol{\sigma}}$ and $R_{(0)} = \phi(\Delta\lambda = 0)$, so $R_{(0)} > R_{(1)} > \cdots > R_{(k)} > \cdots > R_{(N)} = 0$. The subdivision is made such that $\Delta R = (R_{(k)} - R_{(k+1)}) < \sigma_{Y0}$, i.e. the size of each potential residual subdivision should be lower then the first yield stress.

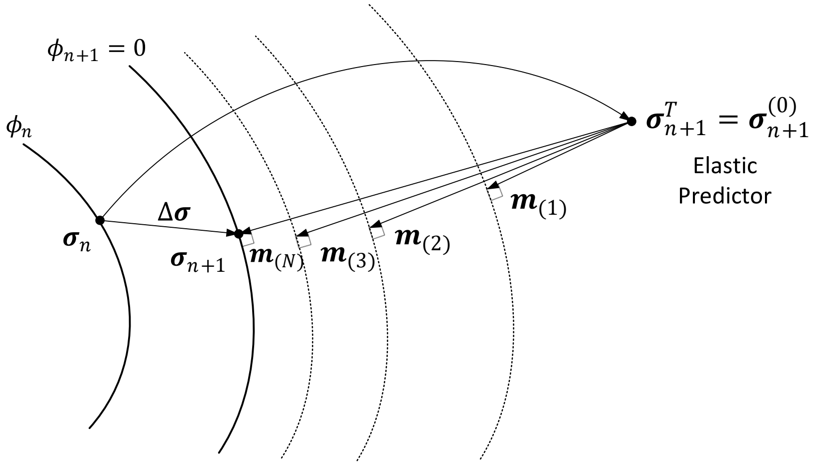
$\phi_{n+1} = 0$
ϕ_n
$\boldsymbol{\sigma}^T_{n+1} = \boldsymbol{\sigma}^{(0)}_{n+1}$
Elastic
Predictor
$\Delta\boldsymbol{\sigma}$
$\boldsymbol{m}_{(1)}$
$\boldsymbol{\sigma}_n$
$\boldsymbol{m}_{(2)}$
$\boldsymbol{\sigma}_{n+1}$
$\boldsymbol{m}_{(N)}$
$\boldsymbol{m}_{(3)}$

Figure 3.2: Graphical representation of multi-stage return mapping method.

Figure 3.2 depicts the integration scheme of multi-stage return mapping algorithm: after computing the trial stress $\boldsymbol{\sigma}^T$, the direction of the first stage $\boldsymbol{m}_{(1)}$ is estimated from the direction of $\boldsymbol{m}_{(0)}$ which is the corresponding normal to the yield surface at $\boldsymbol{\sigma}^T$. Therefore, the calculation $\boldsymbol{m}_{(1)}$ involves a set of non-linear equation solved with the Euler Backward method. Once the first stage is solved, analogously the direction of $\boldsymbol{m}_{(2)}$ is obtained from $\boldsymbol{m}_{(1)}$, which is the normal to the yield surface at $\boldsymbol{\sigma}_{(1)} = \boldsymbol{\sigma}^T - \Delta\lambda \boldsymbol{C}_e \boldsymbol{m}_{(1)}$. The procedure ends when the potential residual equal to zero or within a prescribed tolerance.

Considering the generic k-th stage, its solution is achieved with the following Euler Backward scheme. Eq. 3.26 can be rearranged as:

$$\phi = \bar{\sigma}(\boldsymbol{\sigma}_{(k)}) - \sigma_{Y(k)} - R_{(k)} = 0 \tag{3.27a}$$

where:

$$\boldsymbol{\sigma}_{(k)} = \boldsymbol{\sigma}^T - \Delta\lambda_{(k)} \boldsymbol{C}_e \boldsymbol{m}_{(k)} \tag{3.27b}$$

$$\sigma_{Y(k)} = \sigma_Y[\bar{\varepsilon}_p(n) + \Delta\lambda_{(k)}] = \sigma_Y[\bar{\varepsilon}_p(n)] + \Delta\lambda_{(k)}\, h \tag{3.27c}$$

and h is the hardening modulus of the stress-strain curve.

The Eq. 3.27 permit to define the three following functions:

$$g_1\left(\Delta\lambda^{(j)}_{(k)}\right) = \bar{\boldsymbol{\sigma}}_{(k)} - \sigma_Y[\bar{\varepsilon}_p] - R_{(k)} \tag{3.28a}$$

$$g_2\left(\Delta\lambda_{(k)}^{(j)}\right) = \boldsymbol{C}_e^{-1}(\boldsymbol{\sigma}_{(k)} - \boldsymbol{\sigma}^T) + \Delta\lambda_{(k)}^{(j)}\boldsymbol{m}_{(k)}^{(j)} \tag{3.28b}$$

$$g_3\left(\Delta\lambda_{(k)}^{(j)}\right) = h^{-1}[\sigma_{Y(k)} - \sigma_Y(n)] - \Delta\lambda_{(k)}^{(j)}\boldsymbol{m}_{(k)}^{(j)} \tag{3.28c}$$

that are linearized around the current state variables at each Newton-Raphson j-th iteration to obtain:

$$g_1\left(\Delta\lambda_{(k)}^{(j)}\right) + \boldsymbol{m}_{(k)}^{(j)}\Delta\boldsymbol{\sigma}_{(k)}^{(j)} - \Delta\sigma_{Y\,(k)}^{(j)} = 0 \tag{3.29}$$

Defining:

$$\boldsymbol{E}_{(k)}^{(j)} = \boldsymbol{C}_e^{-1} - \Delta\lambda\frac{\partial\boldsymbol{m}_{(k)}^{(j)}}{\partial\boldsymbol{\sigma}_{(k)}^{(j)}} \tag{3.30}$$

the quantities $\Delta\boldsymbol{\sigma}_{(k)}^{(j)}$ and $\Delta\sigma_{Y\,(k)}^{(j)}$ are defined as:

$$\Delta\boldsymbol{\sigma}_{(k)}^{(j)} = -\left(E_{(k)}^{(j)}\right)^{-1}\left[g_2\left(\Delta\lambda_{(k)}^{(j)}\right) + \boldsymbol{m}_{(k)}^{(j)}\delta\Delta\lambda_{(k)}^{(j)}\right] \tag{3.31a}$$

$$\Delta\sigma_{Y\,(k)}^{(j)} = h^{(j)}\left[-g_3\left(\Delta\lambda_{(k)}^{(j)}\right) + \delta\Delta\lambda_{(k)}^{(j)}\right] \tag{3.31b}$$

$$\delta\Delta\lambda_{(k)}^{(j)} = \frac{g_1\left(\Delta\lambda_{(k)}^{(j)}\right) - \boldsymbol{m}_{(k)}^{(j)}\left(\boldsymbol{E}_{(k)}^{(j)}\right)^{-1}g_2\left(\Delta\lambda_{(k)}^{(j)}\right) + g_3\left(\Delta\lambda_{(k)}^{(j)}\right)h^{(j)}}{\boldsymbol{m}_{(k)}^{(j)}\left(\boldsymbol{E}_{(k)}^{(j)}\right)^{-1}\boldsymbol{m}_{(k)}^{(j)} + h^{(j)}} \tag{3.31c}$$

when the i-th iteration is solved, the following variables are updated:

$$\Delta\lambda_{(k)}^{(j+1)} = \Delta\lambda_{(k)}^{(j)} + \delta\Delta\lambda_{(k)}^{(j)} \tag{3.32a}$$

$$\boldsymbol{\sigma}_{(k)}^{(j+1)} = \boldsymbol{\sigma}_{(k)}^{(j)} + \Delta\boldsymbol{\sigma}_{(k)}^{(j)} \tag{3.32b}$$

$$\sigma_{Y\,(k)}^{(j+1)} = \sigma_{Y\,(k)}^{(j)} + \Delta\sigma_{Y\,(k)}^{(j)} \tag{3.32c}$$

When the Consistency Condition is restored all state variables are updated.

3.3 The Direct method for stress integration

In this Section a new computational method for stress integration of elasto-plastic constitutive equations is formalised and deeply analysed, starting from its first formulation reported in [35, 26]. Compared to other traditional methods based on Newton-Raphson iterations, the proposed algorithm allows to retrieve the stress state directly from the plastic strain increment, characteristic that makes it particularly suitable for inverse identification methods like the non-linear VFM. In this way, in fact, it is possible to avoid convergence problems due to submission of too large strain increments or use Potential Residuals [30], reducing computational time for stress reconstruction. Also, its application is particularly indicated in case of strain maps obtained from experimental full-field measurement with DIC techniques, thanks to its small sensitivity to noise.

According to the notation previously introduced, the flow rule defines the direction of the plastic flow during plasticity, and it is derived from plastic potential ψ. Calling $d\boldsymbol{\varepsilon}_p$ the plastic strain rate, this can be obtained from the plastic potential as:

$$d\boldsymbol{\varepsilon}_p = d\lambda \frac{\partial \psi\left(\boldsymbol{\sigma}, \xi_i^{\psi}\right)}{\partial \boldsymbol{\sigma}} \tag{3.33}$$

where ξ_i^{ψ} are constitutive parameters relative to plastic potential function, $d\lambda$ is a scalar multiplier also called *plastic consistency parameter*. Similarly to the yield criterion, the equation $\psi = 0$ represents a surface in the stress space. The direction of plastic flow can be accordingly considered a vector normal to this surface, as illustrated Figure 3.3. Thus, Eq. 3.33 can be used to calculate its versor $\widehat{\boldsymbol{n}}_p = d\boldsymbol{\varepsilon}_p / \left|d\boldsymbol{\varepsilon}_p\right|$, which is the direction of the plastic flow:

$$\widehat{\boldsymbol{n}}_p = \frac{\partial \psi\left(\boldsymbol{\sigma}, \xi_i^{\psi}\right)}{\partial \boldsymbol{\sigma}} \Bigg/ \left|\frac{\partial \psi\left(\boldsymbol{\sigma}, \xi_i^{\psi}\right)}{\partial \boldsymbol{\sigma}}\right| \tag{3.34}$$

Two important observations can be taken:

- The normal does not depend on the scalar multiplier $d\lambda$;
- In case of convex surfaces, every normal correspond to a unique stress state.

Therefore, if the constitutive parameters are known, the stress state in a material point can be directly derived from the direction of the plastic strain: this consideration is the basis for the proposed stress computation algorithm. The approach is general and can be applied to every plasticity model that involves a convex surface for the plastic potential. Here, we limit the study to

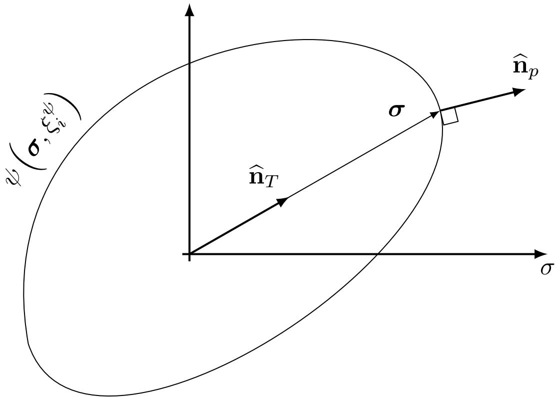

Figure 3.3: Yield surface representation in the π-plane.

associated flow rule, in this case, the plastic potential is the same as the yield criterion, i.e. $\psi = \phi$.

Under this condition, using the yield criterion previously defined as $\phi\left(\boldsymbol{\sigma}, \xi_i\right) = \bar{\sigma}\left(\boldsymbol{\sigma}, \xi_i\right) - \sigma_Y = 0$, Eq. 3.34 becomes:

$$\widehat{\mathbf{n}}_p = \frac{\partial \bar{\sigma}\left(\boldsymbol{\sigma}, \xi_i\right)}{\partial \boldsymbol{\sigma}} \Bigg/ \left| \frac{\partial \bar{\sigma}\left(\boldsymbol{\sigma}, \xi_i\right)}{\partial \boldsymbol{\sigma}} \right| \tag{3.35}$$

The stress tensor $\boldsymbol{\sigma}$ can be represented in the stress space as vector, so, if the equivalent stress function is linear with respect to a scalar parameter:

$$\bar{\sigma}\left(\alpha \boldsymbol{\sigma}, \xi_i\right) = \alpha \, \bar{\sigma}\left(\boldsymbol{\sigma}, \xi_i\right) \,, \tag{3.36}$$

it may be convenient to express the stress in terms of its versor $\widehat{\mathbf{n}}_T$ and its absolute value:

$$\boldsymbol{\sigma} = \left|\boldsymbol{\sigma}\right| \widehat{\mathbf{n}}_T \tag{3.37}$$

and define the normalized equivalent stress as:

$$\widehat{\sigma} = \bar{\sigma}\left(\widehat{\mathbf{n}}_T, \xi_i\right) \tag{3.38}$$

Now, Eq. 3.35 can be rewritten in terms of $\widehat{\mathbf{n}}_T$ as

$$\widehat{\mathbf{n}}_p = \frac{\partial \bar{\sigma}\left(\widehat{\mathbf{n}}_T, \xi_i\right)}{\partial \boldsymbol{\sigma}} \Bigg/ \left| \frac{\partial \bar{\sigma}\left(\widehat{\mathbf{n}}_T, \xi_i\right)}{\partial \boldsymbol{\sigma}} \right| = \mathfrak{G}\left(\widehat{\mathbf{n}}_T, \xi_i\right) \tag{3.39}$$

that can be view as a function $\mathfrak{G}$, which associate the stress direction to the plastic flow direction. If such function is invertible, it is possible to obtain the stress versor from the plastic flow direction:

$$\widehat{\mathbf{n}}_T = \mathfrak{G}^{-1}\left(\widehat{\mathbf{n}}_p, \xi_i\right) \tag{3.40}$$

The norm of stress tensor can be retrieved coupling the definition of equivalent stress with Eq. 3.38, viz:

$$|\boldsymbol{\sigma}| = \sigma_Y \, \widehat{\sigma}^{-1} \, ; \tag{3.41}$$

finally, using Eq. 3.37, Eq. 3.41 and Eq. 3.40, the Cauchy stress tensor can be derived directly from the direction of the plastic flow as:

$$\boldsymbol{\sigma} = \sigma_Y \widehat{\sigma}^{-1} \mathfrak{G}^{-1}\left(\widehat{\mathbf{n}}_p, \xi_i\right) \tag{3.42}$$

If hardening is considered, the yield stress σ_Y and the constitutive parameters ξ_i are modified during the plastic deformation. So, in case of isotropic hardening, σ_Y is modified while the yield surface expands with deformation. Usually the hardening law has this form:

$$\sigma_Y = \sigma_Y\left(\bar{\varepsilon}_p, \xi_i^H\right) \tag{3.43}$$

where ξ_i^H are hardening law material parameters and $\bar{\varepsilon}_p$ is a scalar value that represent the equivalent cumulated plastic strain. Therefore, during plastic deformation the Cauchy stress is a function of the stress direction, the total equivalent plastic strain and the constitutive parameters, i.e. $\boldsymbol{\sigma}(\widehat{\mathbf{n}}_p, \bar{\varepsilon}_p, \xi_i, \xi_i^H)$.

The equivalent plastic strain is defined so that the plastic work can be expressed in terms of the equivalent stress:

$$\int_{\bar{\varepsilon}_p(0)}^{\bar{\varepsilon}_p(t)} \sigma_Y d\bar{\varepsilon}_p = \int_{\boldsymbol{\varepsilon}_p(0)}^{\boldsymbol{\varepsilon}_p(t)} \boldsymbol{\sigma} : d\boldsymbol{\varepsilon}_p \tag{3.44}$$

where $\boldsymbol{\varepsilon}_p$ is the plastic strain tensor. The infinitesimal increment of plastic strain $d\bar{\varepsilon}_p$ can be derived from Eq. 3.44 and expressed in terms of the stress and plastic flow versor. It follows:

$$d\bar{\varepsilon}_p = \widehat{\mathbf{n}}_T : \widehat{\mathbf{n}}_p \left|d\boldsymbol{\varepsilon}_p\right| \widehat{\sigma}^{-1} \tag{3.45}$$

This approach allows to derive directly the stress from the plastic flow and can be used in all those problem where the deformation is known *a priori*. The main drawbacks of such technique are:

- the plastic flow direction is evaluated from the plastic strain rate. In a fully developed plasticity flow, the plastic strain can be approximated with the total one, however, such approximation can lead to errors at the early stages of plastic deformation, showing a dependence from plastic strain amplitude;

- the inverse function $\mathfrak{G}^{-1}$ is not always available in closed-form. Therefore, numerical methods are required to its evaluation.

All those aspects will be studied deeply in the following sub sections. The present method is formalised for the full-scale with 6 components of stress, however, here is studied only in 2D problems.

3.3.1 Numerical implementation

The stress computation algorithm is summarized in the flow diagram of Figure 3.4. Let consider that all information about stress and strain state are known for time step n and the final goal is to compute them for the subsequent step $n+1$. Analogously to traditional integration schemes, the starting point for implementation of direct method consists on discrimination of the strain increment in elastic or plastic.Initially, a trial stress $\boldsymbol{\sigma}^T$ state is computed assuming that strain increment is purely elastic; this stress is also called *elastic predictor*, and it is calculated for each material point. Then, the active yielding condition asses if the increment exceeds or not the elastic regime, exploiting the definition given by Consistency Condition. If not, the elastic predictor hypothesis is verified, thus these stresses and equivalent plastic strain relative to time $n+1$ are stored. Otherwise, when the difference $\bar{\sigma}(\boldsymbol{\sigma}^T) - \sigma_Y(n)$ is positive, plasticity occurs.

Here, the direct method take action. Accordingly to theoretical framework introduced in the previous section, the plastic flow direction can be determined from the plastic strain rate. However, if strain increment is relatively large, the elastic part can be neglected and total strain increment can be supposed equal to the plastic one, making also computation more efficient. The procedure core relies on the Associative Flow Rule, which permits to define a relationship between the two direction of plastic strain rate and stress through the function $\mathfrak{G}$ and its inverse $\mathfrak{G}^{-1}$. Thereby, equivalent plastic strain rate can be calculated with Eq. 3.45, and total $\bar{\varepsilon}_p(n+1)$. Updated stress is finally obtained directly from the plastic increment independently from stress state of previous time step. This because, at certain equivalent plastic strain, for each plastic increment will correspond only one equivalent stress given by the yield function and only one stress tensor direction. Also, the aforementioned independence represent a convenient characteristic in case of experimental strain data, where missing measurement points at some time steps can affect the success of stress integration in the consecutive steps.

In the following part, all these aspects will be discussed in detail.

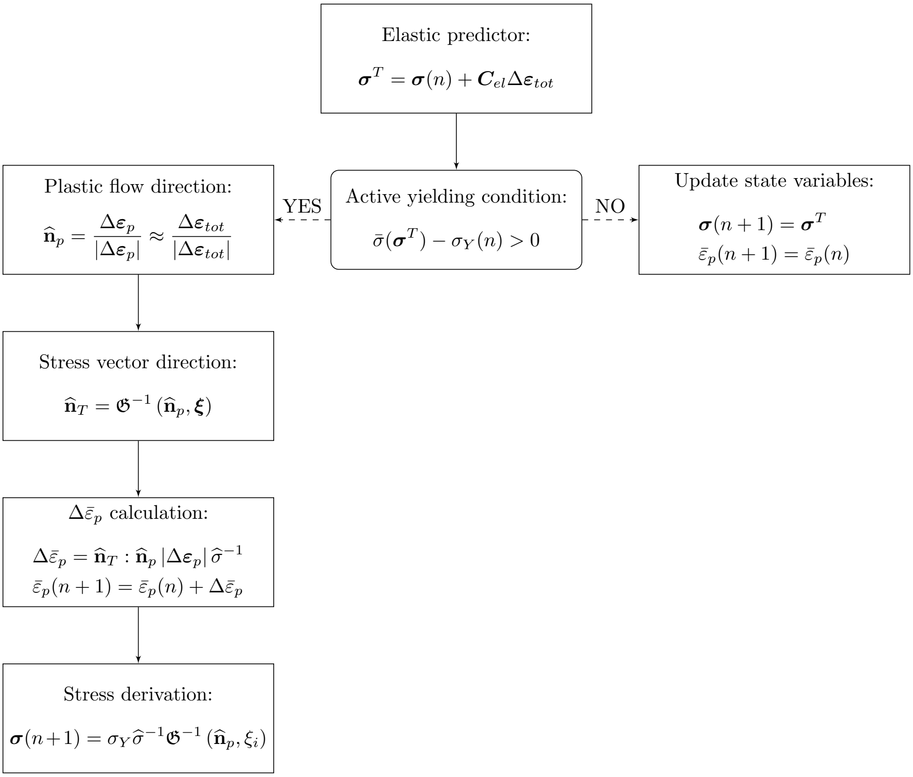
Elastic predictor:
$\boldsymbol{\sigma}^T = \boldsymbol{\sigma}(n) + \boldsymbol{C}_{el}\Delta\boldsymbol{\varepsilon}_{tot}$
Active yielding condition:
$\bar{\sigma}(\boldsymbol{\sigma}^T) - \sigma_Y(n) > 0$
YES
NO
Update state variables:
$\boldsymbol{\sigma}(n+1) = \boldsymbol{\sigma}^T$
$\bar{\varepsilon}_p(n+1) = \bar{\varepsilon}_p(n)$
Plastic flow direction:
$\widehat{\mathbf{n}}_p = \frac{\Delta\boldsymbol{\varepsilon}_p}{|\Delta\boldsymbol{\varepsilon}_p|} \approx \frac{\Delta\boldsymbol{\varepsilon}_{tot}}{|\Delta\boldsymbol{\varepsilon}_{tot}|}$
Stress vector direction:
$\widehat{\mathbf{n}}_T = \mathfrak{G}^{-1}(\widehat{\mathbf{n}}_p, \boldsymbol{\xi})$
$\Delta\bar{\varepsilon}_p$ calculation:
$\Delta\bar{\varepsilon}_p = \widehat{\mathbf{n}}_T : \widehat{\mathbf{n}}_p \, |\Delta\boldsymbol{\varepsilon}_p| \, \widehat{\sigma}^{-1}$
$\bar{\varepsilon}_p(n+1) = \bar{\varepsilon}_p(n) + \Delta\bar{\varepsilon}_p$
Stress derivation:
$\boldsymbol{\sigma}(n+1) = \sigma_Y \widehat{\sigma}^{-1} \mathfrak{G}^{-1}(\widehat{\mathbf{n}}_p, \xi_i)$

Figure 3.4: Flow diagram for implementation of direct stress integration method.

Plastic flow derivation

The plastic flow direction is defined as the direction the plastic strain rate:

$$\widehat{\mathbf{n}}_p = \Delta\boldsymbol{\varepsilon}_p^{(n)} / \left|\Delta\boldsymbol{\varepsilon}_p^{(n)}\right| \tag{3.46}$$

where $\Delta\boldsymbol{\varepsilon}_p$ is the plastic strain tensor. In case of discrete increments, the plastic strain rate at time t can be evaluated as:

$$\Delta\boldsymbol{\varepsilon}_p = \frac{\partial\boldsymbol{\varepsilon}_p}{\partial t} \approx \frac{\boldsymbol{\varepsilon}_p{}^{(t)} - \boldsymbol{\varepsilon}_p{}^{(t-1)}}{\Delta t} = \frac{\Delta\boldsymbol{\varepsilon}_p{}^{(t)}}{\Delta t} \tag{3.47}$$

Also, the strain rate at time t can be computed also using the steps before and after. For instance using a convolution derivation as the one proposed by Gorry [36]. In this case, if we consider m steps before and after the step t, the strain rate becomes:

$$\Delta\boldsymbol{\varepsilon}_p = \frac{\partial\boldsymbol{\varepsilon}_p}{\partial t} \approx \frac{\sum_{j=-m}^{m} h_j \boldsymbol{\varepsilon}_p{}^{(t+m)}}{\Delta t} \tag{3.48}$$

where h_j are convolution weights that depends on the number of points and the grade of the polynomial used to compute the derivation. This technique allow also to have an efficient temporal smoothing in case of noisy data, as in case of experimental strain data.

Since the plastic deformation is isochoric in pressure-independent plasticity and, at large strains, the elastic part is small compared to the plastic one, the plastic strain tensor ${\boldsymbol{\varepsilon}_p}^{(t)}$ can be approximately reduced to the deviatoric part of the total strain tensor $\boldsymbol{\varepsilon}^{(t)}$:

$$\boldsymbol{\varepsilon}_p \approx \boldsymbol{\varepsilon} - \frac{1}{3} tr\left(\boldsymbol{\varepsilon}\right) \mathbf{I}\,. \tag{3.49}$$

Stress computation

Here practical examples of direct integration scheme are introduced for two anisotropic plasticity material models: the Hill48 and The YLD2000-2d, in the case of plane stress conditions. For the sake of clarity, the stress and strain tensor are reduced to vectors using the Voigt notations:

$$\begin{aligned} &\boldsymbol{\sigma} \longrightarrow \boldsymbol{\sigma} = \left(\sigma_{11}, \sigma_{22}, \tau_{12}\right) \\ &\boldsymbol{\varepsilon} \longrightarrow \boldsymbol{\varepsilon} = \left(\varepsilon_{11}, \varepsilon_{22}, \gamma_{12}\right) \\ &\widehat{\mathbf{n}}_T \longrightarrow \widehat{\mathbf{n}}_T = \left(\widehat{n}^T_{11}, \widehat{n}^T_{22}, \widehat{n}^T_{12}\right) \\ &\widehat{\mathbf{n}}_p \longrightarrow \widehat{\mathbf{n}}_p = \left(\widehat{n}^p_{11}, \widehat{n}^p_{22}, \widehat{n}^p_{12}\right) \end{aligned} \tag{3.50}$$

where $\gamma_{ij} = 2\,\varepsilon_{ij}$. The versors $\widehat{\mathbf{n}}_T$ and $\widehat{\mathbf{n}}_p$ are derived accordingly by normalizing the corresponding stress or strain vector.

Implementation of Hill48 In plane stress condition, the Hill48 criterion can be written as [18]:

$$\bar{\sigma}\left(\boldsymbol{\sigma}\right) = \left[\left(g+h\right)\sigma_{11}^2 + \left(f+h\right)\sigma_{22}^2 - 2h\;\sigma_{11}\sigma_{22} + 2\,n\;\sigma_{12}^2\right]^{\frac{1}{2}} \tag{3.51}$$

where $\xi = \{g, f, h, n\}$ are four anisotropic constants of that can be derived from the Lankford parameter R, measured in three different orientations [19, 37, 12]. The normalized equivalent stress of Eq. 3.38 is, in this case, written as:

$$\widehat{\sigma} = \left[\left(g+h\right)\,{\widehat{n}^T_{11}}^{\;2} + \left(f+h\right)\,{\widehat{n}^T_{22}}^{\;2} - 2h\,\widehat{n}^T_{11}\widehat{n}^T_{22} + n\;\;{\widehat{n}^T_{12}}^{\;2}\right]^{\frac{1}{2}} \tag{3.52}$$

Gradient of function describing a surface represents the normal vector to the surface, so the direction of the plastic flow is derived from Eq. 3.51:

$$\frac{\partial\bar{\sigma}\left(\widehat{\mathbf{n}}_T, \xi_i\right)}{\partial\boldsymbol{\sigma}} = \widehat{\sigma}^{-1} \begin{bmatrix} (h+g) & -h & 0 \\ -h & (f+h) & 0 \\ 0 & 0 & 2n \end{bmatrix} \begin{Bmatrix} \widehat{n}^T_{11} \\ \widehat{n}^T_{22} \\ \widehat{n}^T_{12} \end{Bmatrix} \tag{3.53}$$

The plastic flow direction is a linear transformation of the stress normal. Thus, the inverse function $\mathfrak{G}^{-1}$ can be easily obtained as the inverse of the transformation matrix of Eq. 3.53:

$$\widehat{\mathbf{n}}_{\sigma} = \frac{\mathbf{A}\widehat{\mathbf{n}}_p}{|\mathbf{A}\widehat{\mathbf{n}}_p|} \quad \text{with} \quad \mathbf{A} = \begin{bmatrix} f+h & h & 0 \\ h & h+g & 0 \\ 0 & 0 & \frac{gf+gh+hf}{2n} \end{bmatrix} \tag{3.54}$$

and the stress can be directly derived with no iteration using Eq. 3.42. Therefore, for Hill48, it stands:

$$\boldsymbol{\sigma} = \sigma_Y \widehat{\sigma}^{-1} \frac{\mathbf{A}\widehat{\mathbf{n}}_p}{|\mathbf{A}\widehat{\mathbf{n}}_p|} \tag{3.55}$$

Implementation of YLD2000-2D As reported in Section 2.3.2, the equivalent stress according to YLD2000-2D criterion is:

$$\boldsymbol{\sigma}\left(\boldsymbol{\sigma}\right) = \left[\frac{1}{2}\left(|X_1' - X_2'|^a + |2X_2'' + X_1''|^a + |2X_1'' + X_2''|^a\right)\right]^{\frac{1}{a}} \tag{3.56}$$

where X_1', X_2' and X_1'', X_2'' are the principal values of the $\mathbf{X}'$ and $\mathbf{X}''$ tensors obtained from the Cauchy stress $\boldsymbol{\sigma}$ using two linear transformation, according to $\mathbf{L}'$ and $\mathbf{L}''$, respectively.

In this case, the derivative of Eq. 3.56 to obtain the direction of the plastic flow is not straightforward. It can be derived using the chain rule on the different stress transformations. All the steps are detailed in the Appendix of [22] and will not be repeated here. Compared to the Hill48 case, for Yld2000-2D, to the best authors' knowledge, does not exist a direct formula for the inverse function $\mathfrak{G}^{-1}$. Therefore, a numeric algorithm is used using the concept of scattered data interpolant [38].

First, M samples of stress vector norms are selected from the whole yielding function domain. Then, the corresponding plastic flow directions are computed according to normality of plastic flow with respect to the yield surface:

$$\widehat{\mathbf{n}}_p^{(j)} = \frac{\partial\bar{\sigma}\left(\widehat{\mathbf{n}}_T^{(j)}, \xi_i\right)}{\partial\boldsymbol{\sigma}} \Bigg/ \left|\frac{\partial\bar{\sigma}\left(\widehat{\mathbf{n}}_T^{(j)}, \xi_i\right)}{\partial\boldsymbol{\sigma}}\right| \quad \text{for } j = 1, \ldots, M\,. \tag{3.57}$$

Then an interpolation function Θ is used to create a scattered data interpolant $\mathfrak{I}$, using $\mathbf{n}_p$ as domain and $\mathbf{n}_T$ as corresponding target.

$$\mathfrak{I} = \Theta\left(\widehat{\mathbf{n}}_p^{(j)}, \widehat{\mathbf{n}}_T^{(j)}\right) \tag{3.58}$$

In other words, $\mathfrak{I}$ plays the same role of function $\mathfrak{G}^{-1}$, so such interpolant can be used to evaluate the stress normal from each value of the plastic flow direction.

$$\widehat{\mathbf{n}}_T = \mathfrak{I}\left(\widehat{\mathbf{n}}_p\right) \quad \forall\, \widehat{\mathbf{n}}_p \tag{3.59}$$

This kind of interpolant operators, are implemented in MATLAB®, but can be developed also in other programming languages. Such procedure is computationally very efficient as will be demonstrated later on.

3.3.2 Validation on numerical data

The goodness of the proposed algorithm for stress reconstruction is evaluated performing a comparison with data obtained from a Finite Element Analysis. Thus, a numerical model reproducing a simple tensile test on notched specimen (Figure 3.5), able to provide heterogeneous strain fields and evolving yield locus [2, 39], was realised using the commercial code ABAQUS-Standard®, assuming plane stress state condition.

Concerning the specimen's material, its hardening behaviour was described by the well-known Swift's law:

$$\bar{\sigma} = K_H(\varepsilon_0 + \bar{\varepsilon}_p)^{n_H} \ , \tag{3.60}$$

where $\bar{\sigma}$ indicates the equivalent stress and p the equivalent plastic strain. In this case, the input material parameters $\xi_i^H = \{k_H, \varepsilon_0, n_H\}$ for the hardening rule were chosen arbitrary hypothesising a general austenitic stainless steel. Moreover, anisotropic plasticity behaviour, typical of metal sheets widely employed in forming applications, was included using the two material models reported in the previous section, Hill48 and YLD2000-2D, the latter implemented with an user subroutine UMAT following the approach described Section 3.2.2; also two different material orientations were considered at 0° and 30° with respect to the direction of tensile load application. All numerical model's characteristics and material properties entries are listed in Table 3.1.

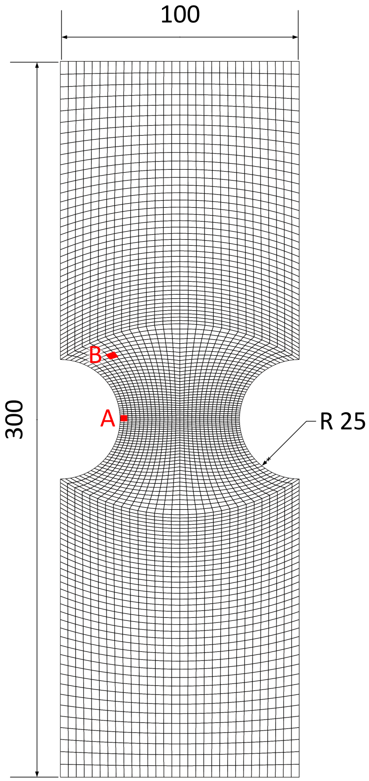

Figure 3.5: Specimen geometry. Dimensions are in mm.

Element type		CPS4R	
Elements number		4200	
Nodes number		4361	
Elastic constants			
E		200 GPa	
ν		0.3	
Swift's law parameters			
K_H		1000 MPa	
ϵ_0		0.05	
n_H		0.5	
Anisotropy parameters			
Hill48		YLD2000-2d	
R_0	2.2	α_1	1.11
R_{45}	1.5	α_2	1.35
R_{90}	1.8	α_3	1.21
		α_4	1.11
		α_5	1.07
		α_6	0.96
		α_7	1.21
		α_8	1.15
		a	8

Table 3.1: FE model characteristics and constitutive parameters used.

Boundary conditions replicating a tensile test in displacement control were set fixing the nodes on the lower side of the specimen and applying to the upper side ones a vertical displacement of 45 mm increasing linearly; hence, total displacement was split in two consecutive steps of 1 mm and 44 mm mm, subdivided each one in 30 equispaced time increments, in order to better assess the response of the algorithm at different strain increments and also observe its stress reconstruction ability during the transition between elastic and plastic regimes. Thereby, FEA variables outputs like strains, stresses and equivalent plastic strain were extrapolated at each loading increment respectively for all elements' integration points and nodes.

Evaluation at Integration Points

The described FE model was built adopting CPS4R element, characterized by 4 nodes, bilinear shape function and reduced integration method with hourglass control, which provides one integration point for each element. It is worth noting that stress computation is more accurate at integration points due to numerical calculation of Stiffness Matrix exactly there. So, a first appraisal of the proposed algorithm performances was conducted comparing, at the same Gauss point, stresses reconstructed analytically from FEA strain data with the ones obtained from ABAQUS® simulation, as depicted in Figure 3.6a, where material orientation was at 0° with respect to tensile load direction and anisotropic behaviour described by Hill48 model. Considering element A in proximity of left notch, stresses derived from direct method match with FEA results, both in elastic and fully developed plastic regimes. At time step 3, where first yielding is just reached and exceeded, σ_{xx} and σ_{yy} exhibit a difference: in fact, at this strain increment the elastic part is not negligible and the assumption $d\boldsymbol{\varepsilon}_p \approx d\boldsymbol{\varepsilon}_{tot}$ leads to an error determining the plastic flow direction according to Eq. 3.46. However, the direct integration scheme is able to correct this error in the subsequent stage, since the stress derivation in plastic regime is achieved without considering the previous stress state.

Also a comparative of equivalent plastic strain calculation was executed; considering again the same Gauss point, the procedure described in 3.3.1 match with the results coming from Finite Element Analysis (Figure 3.6b).

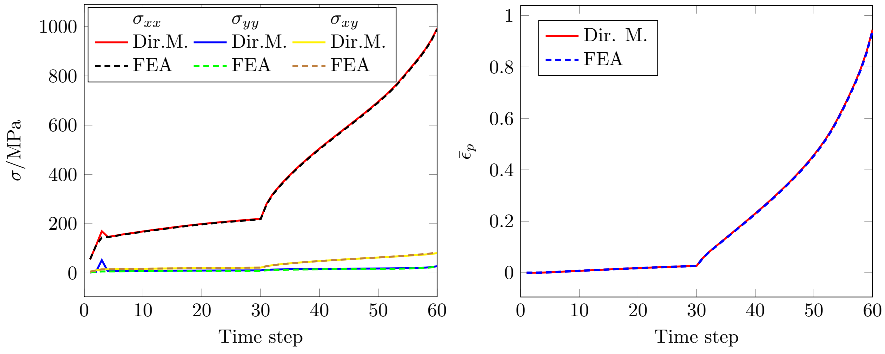

(a) Stresses

(b) Equivalent plastic strain

Figure 3.6: Comparison between reconstructed stresses, equivalent plastic strain and resulting data from FEA at integration point A.

Now, let's take into account the integration point relative to element B in Figure 3.5 where, during traction, the material underwent to unloading due to strain localization in the area between two notches. The direct integration algorithm is not able to reconstruct stresses properly in two critical instants (Figure 3.7a): the first, corresponding to time step 11, whose differences are related again to early stage of plastic deformation; the latter at time step 56, where unloading phase started, protracting until last time step. In fact, although material point is fully developed plasticity regime, here the strain increment is too small and elastic component is comparable to the plastic one. Therefore, error in stress calculation increases in the subsequent step, since unloading represents an elastic loading and, thus, is added to the previous stress state according to Figure 3.4. This mismatching can be solved modifying the *Active Yielding Condition* defining an appropriate residual value threshold R_{th}, viz:

$$\bar{\sigma}(\boldsymbol{\sigma}^T) - \sigma_Y(n) > R_{th}\,; \tag{3.61}$$

stress reconstruction results employing an $R_{th} = 0.05$ are displayed in Figure 3.7b.

The introduction of residual threshold R_{th} does not lead to significant differences in accumulated equivalent plastic strain calculation (Figure 3.7c), albeit there is a slight gap between FEA data and results from direct integration scheme for the last time increments.

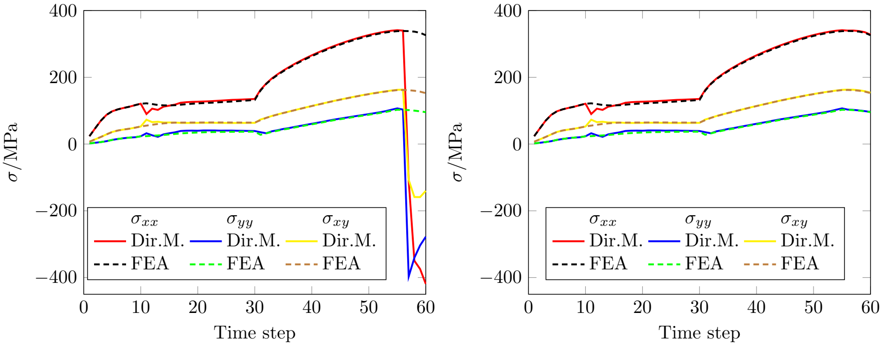

(a) Stresses

(b) Stresses with $R_{th} = 0.05$

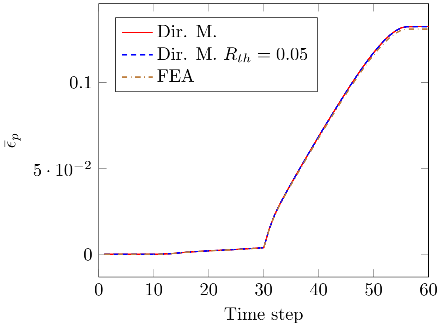

(c) Equivalent plastic strain

Figure 3.7: Comparison between reconstructed stresses, equivalent plastic strain and resulting data from FEA at integration point B.

Global Error

Results of the introduced direct method for stress integration are also evaluated in terms of global error, taking into account the whole strain maps obtained from the FEA. Extending this analysis to the numerical simulation of notched specimen described by Hill48 introduced previously, Figure 3.8 compares the Cauchy stress tensor components with the ones computed using the proposed method, showing a good agreement between the two data sets. Highest differences are observed in proximity of notches' corners, where material just undergoes to plastic deformation and σ_{yy} exhibits a maximum error around 20 MPa. The picture also shows a difference of few MPa highlighting mesh texture effect that is linked to averaging smoothing performed by FEA software during stress maps generation.

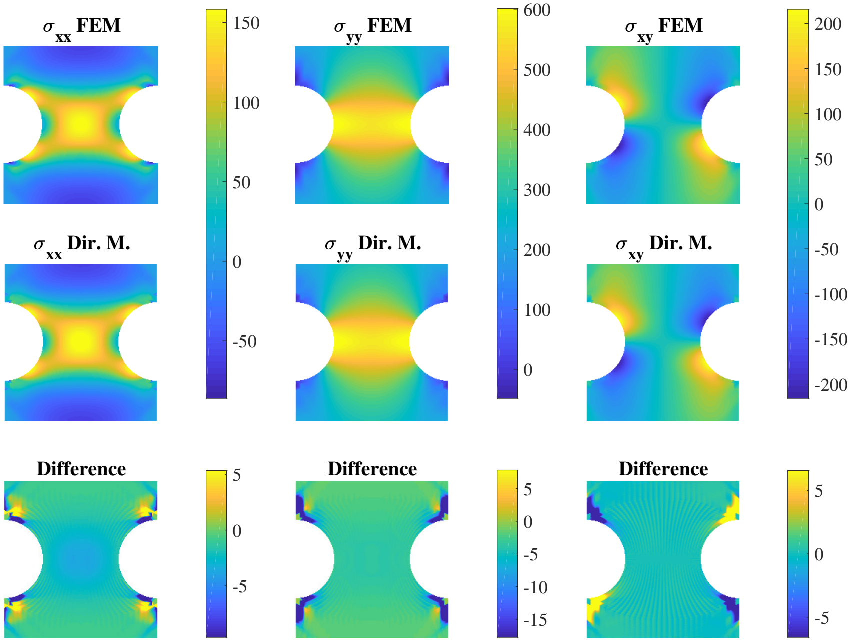

Figure 3.8: Cauchy stress comparison for notched specimen with material orientation at 0°, modelled using Hill48.

The same response is found considering the YLD2000-2D material model, as reported in Figure 3.9, which display the stress reconstruction and comparison for a notched specimen having material orientation at 30° with respect to load direction.

Evaluation of Internal Work gives a better insight on global impact of ob-

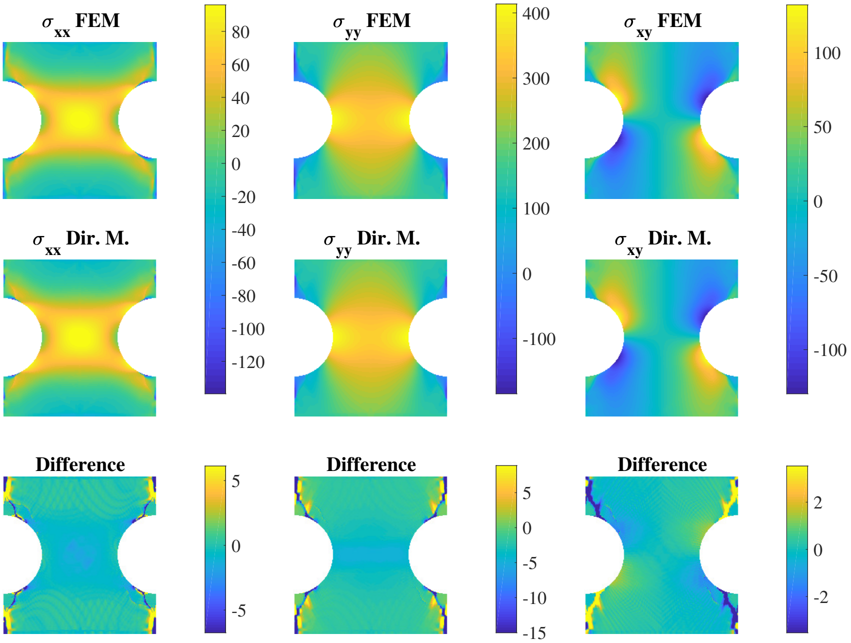

Figure 3.9: Cauchy stress comparison for notched specimen with material orientation at 30°, modelled using YLD2000-2D.

served differences in stress computation, and, also, considering that inverse identification methods as VFM are founded on the Virtual Work Principle, it is an helpful check to assess applicability of the proposed algorithm. So, defining the Internal Work as:

$$W_i = \int_V \boldsymbol{\sigma} : \boldsymbol{\varepsilon}_{tot} \, dV \,, \tag{3.62}$$

Figure 3.10 reports its calculation along all the 60 steps of simulation for the notched specimen modelled with Hill48 and material orientation at 0°, comparing data from FEA with the ones analytically retrieved using the proposed method. A perfect correspondence is found until time step 54, then there is a mismatching between the two data sets due to unloading. Thus, different values of R_{th} are set starting from the first yield stress $\sigma_{Y_0} = k_0 \varepsilon_0^{n_H}$ in order to assess the optimal residual threshold limit. Indeed, the best match is founded for $R_{th} = \sigma_{Y_0}/2$.

Moreover, taking into account the YLD2000-2D material model, Figure 3.11 displays the Internal Work evaluation for notched specimen oriented at 30°, exhibiting a perfect conformity between numerical and analytical data, although unloading is not present with the applied displacement of 45 mm.

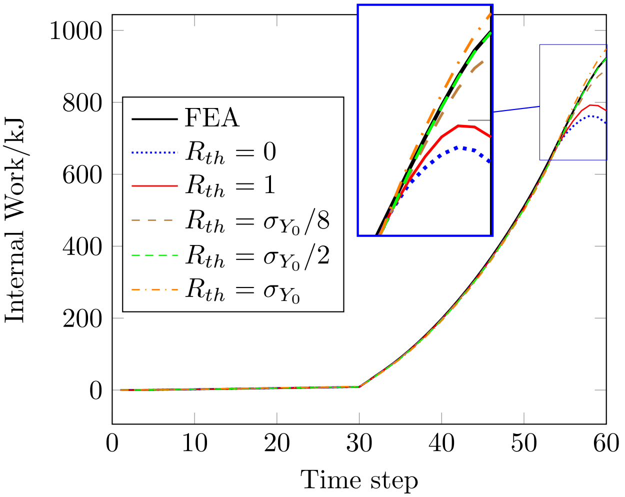

Figure 3.10: Interal Work evaluation and comparison using Hill48 model at different R_{th} values.

Influence of strain increment size

Another important feature consists on the ability by stress integration method to reconstruct the stress state independently from amplitude and number of strain increments. Thus, the Cauchy stress tensor is calculated involving separately

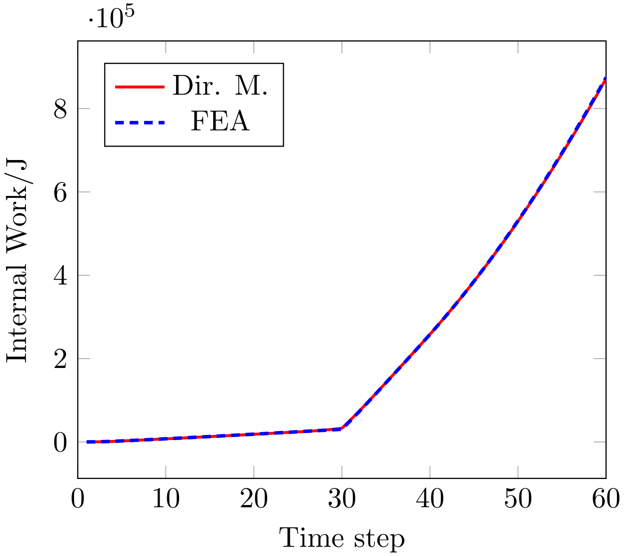

Figure 3.11: Interal Work evaluation and comparison using YLD2000-2D model.

1 and 10 strain increments, and then verify the dissimilarity with the FEA results as illustrated in Figure 3.12 and Figure 3.13 respectively for Hill48 and YLD2000-2D. For both material models the proposed algorithm is able to reconstruct properly the stress fields even with only one strain increment, although employing more steps reduces error compared to numerical simulation outcomes, especially looking at the area between notches where highest values of plastic deformation are reached. In fact, since the stress computation relies on plastic flow direction, when only 1 step of strain increment is considered the elastic deformation weights more in the determination of plastic flow direction. On the other hand, using more strain increments to get the same deformation level splits better the elastic increment from the plastic one, limiting the observed error only in increment where material actively yields but the elastic deformation is not negligible.

Influence of noise

Stress integration often involves strain data obtained experimentally with full-field measurements as, for instance, DIC technique, which are intrinsically affected by experimental noise uncertainty. This issue is not particularly relevant in large deformations when plasticity material parameters are retrieved using the non-linear VFM , but it can have effects determining the plastic flow direction. So, the proposed algorithm response is tested submitting noisy strain maps

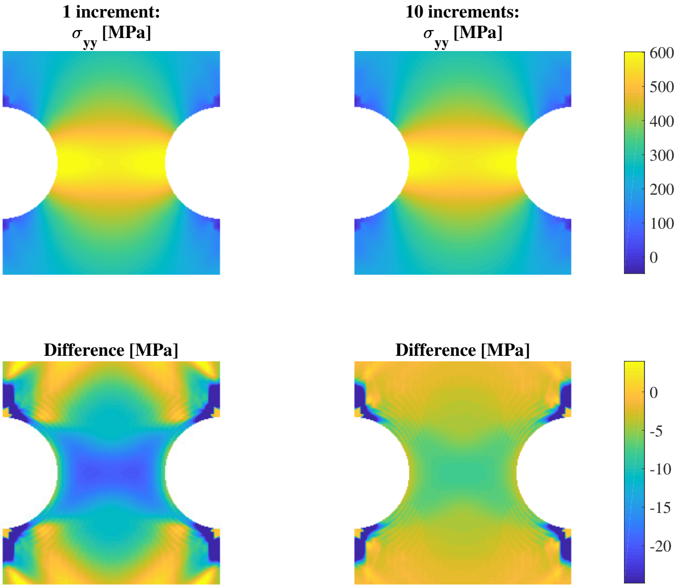

Figure 3.12: Stress integration at different strain increments, using Hill48 material model.

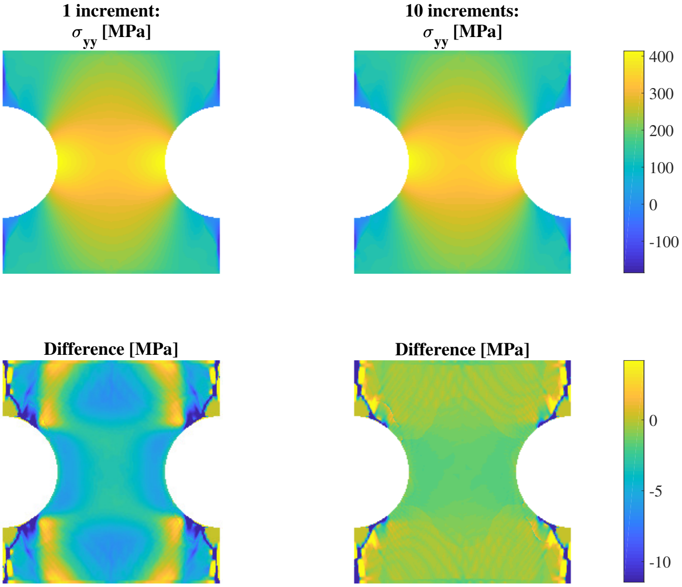

Figure 3.13: Stress integration at different strain increments, using YLD2000-2D material model.

defined according to:

$$\boldsymbol{\varepsilon}_N = \boldsymbol{\varepsilon}_{FEA} + k_N \Upsilon(\mu_G, \sigma_G)\,, \tag{3.63}$$

where $\boldsymbol{\varepsilon}_{FEA}$ indicates the FEA strain data, $\Upsilon(\mu_G, \sigma_G)$ is a randomly generated array described by a normal distribution with mean $\mu_G = 0$ and standard deviation $\sigma_G = 1$, k_N is a factor relative to noise level. In this case, two levels are considered giving respectively a standard deviation of 10^{-4} and 10^{-3}, the latter representing usually the noise disturb affecting strain DIC measurement. All results are reported in Figure 3.14 and Figure 3.9 for both anisotropic plasticity models previously described. Looking to the plastic zone of the notched specimen, the stress reconstruction algorithm shows a good response to noisy data. Obviously noise has stronger impact on specimen zones where material is closer to elastic regime, and its main drawback concerning the error determining plastic flow direction leads differences over 100 MPa in case of higher level of noise (10^{-3}).

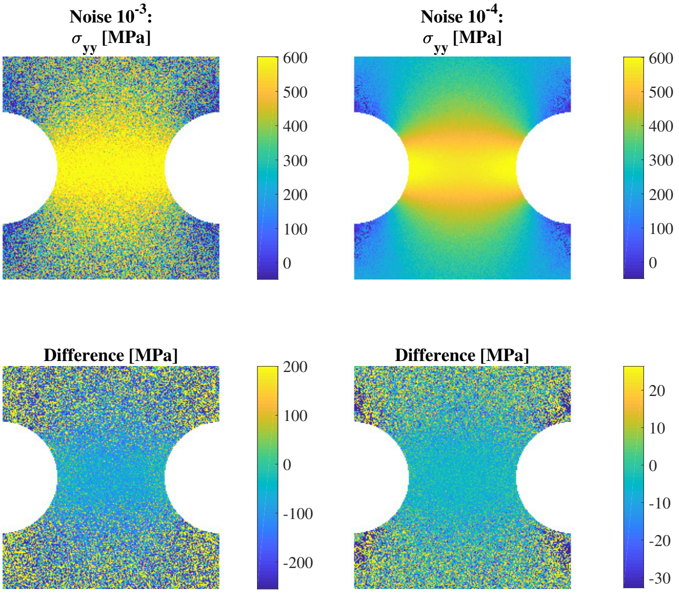

Figure 3.14: Stress integration from strain field affected by noise, using Hill48 material model.

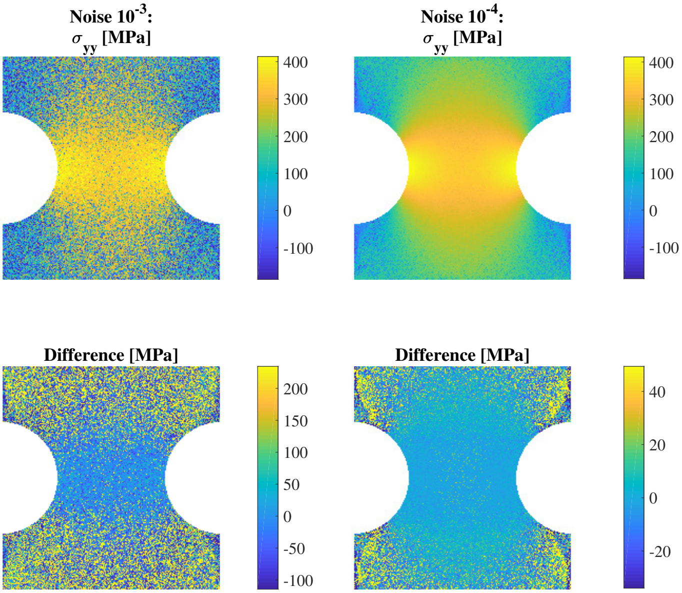

Figure 3.15: Stress integration from strain field affected by noise, using YLD2000-2D material model.

Benchmark

Computational time represent a crucial feature for the utilization of algorithms in industrial applications. Thus, a time benchmark was realised comparing the proposed direct stress integration method with the robust Euler Backward with multi-stage return mapping scheme reported in [29, 30, 22]. The machine employed for the analysis was equipped with an Intel® Core™ i7-7700HQ CPU @ 2.80 GHz 2.80 GHz, 16 MB RAM, and all benchmark routines are tested on single core without parallelization.

Stress integration algorithms' performances were evaluated with the high-level programming language MATLAB® for both Hill48 and YLD2000-2D material models. Basically, stress state is calculated from arrays with different size having the same strain increment, that in this case is correspondent to 0.3% equivalent plastic strain. Figure 3.16 displays the results in a double-logarithmic diagram, showing a significant computational time reduction using the direct method compared to the Euler Backward scheme due to absence of Newton-Raphson iterations to solve the non-linear problem. Concerning material models, also, YLD2000-2D is more time consuming on the proposed direct method compared to Hill48 due to numerical interpolation algorithms.

Furthermore, the same integration methods comparison was extended to a

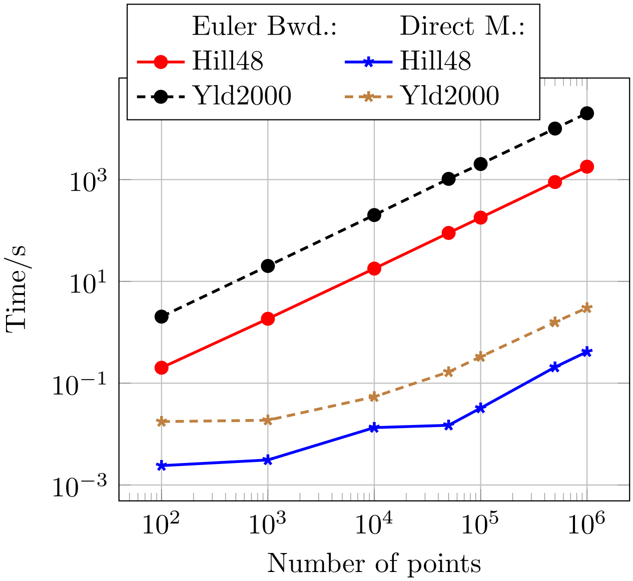

Figure 3.16: Computational time evaluation using Matlab®.

low-level programming language, the Fortran95, this time involving only the Hill48 constitutive material model (Figure 3.17). Two strain increments are considered for computational time evaluation, the first at $\bar{\varepsilon}_p = 1\%$ and the latter at $\bar{\varepsilon}_p = 15\%$. Since the Euler Backward method implemented divides the residual of consistency condition equation in sub-step to ensure convergence, large strain increments requires more stages and, thus, more computational time. Direct stress integration algorithm, instead, is not sensitive to strain increment size, confirming its rapidness.

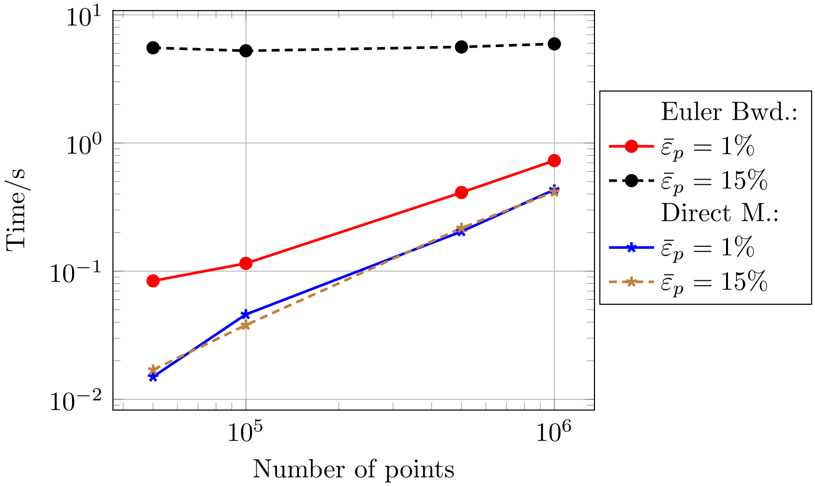

Figure 3.17: Computational time evaluation using Fortran95 language for Hill48.

Chapter 4

The Virtual Fields Method for large strain problems

4.1 Introduction

Problems in mechanics of deformable solids are founded on the connection between displacements, strains and stresses, each of them defined for all material points. These quantities, indeed, are regulated by the well-known equations of continuum mechanics, distinguished in equilibrium, kinematics and constitutive equations. In this framework, the problem is defined as *direct* when parameters that govern a certain constitutive law are known; otherwise, when the final main objective is to retrieve material properties such problems are called *inverse* [4]. Several inverse procedures for material identification from full-field measurement data can be found in literature. One on the most widespread is the Finite Element Model Update (FEMU) method [40, 41, 42, 39, 43], that performs iteratively numerical simulations of test in order to find the constitutive parameters that match the actual material data; other examples are also given by the Constitutive Equation Gap Method [44] in case of elastic properties, and the Equilibrium Gap Method, used in [45] to identify damage fields parameters. Among them, the Virtual Fields Method (VFM) [46, 47, 48] has the prominent role in the presented research activity.

Conceptually VFM is based on the Principle of Virtual Work applied on appropriate virtual fields. This method provides, in fact, several benefits compared to other inverse techniques as FEMU, especially concerning the computational time for the identification process. Also, the procedure does not rely on the numerical modeling assumptions, i.e. mesh size dependence for example, and the only requirement prescribes to employ kinematically admissible virtual displacement fields. The theoretical framework of VFM dealing with typical non-linear problems as large deformations is described in the following sections according to [49, 48, 35].

4.2 The Principle of Virtual Work for finite strains

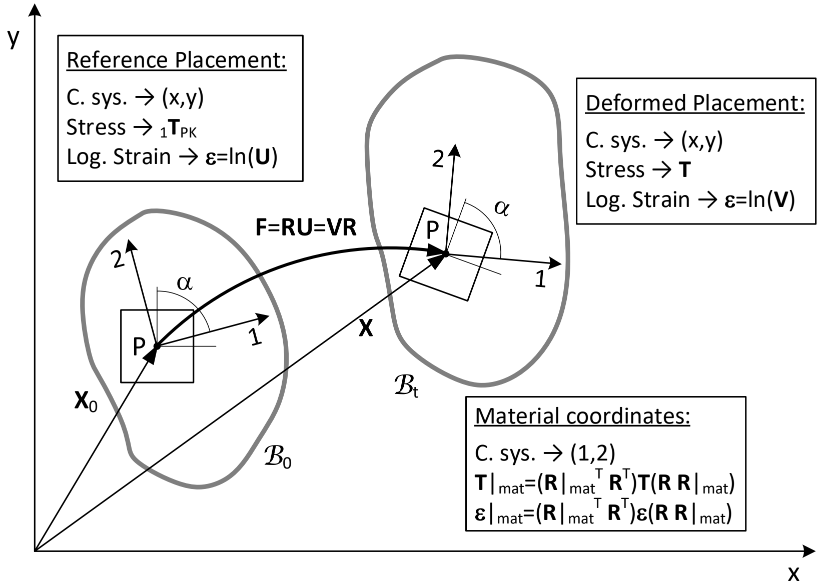
y
Reference Placement:
C. sys. → (x,y)
Stress → $_1\mathbf{T}_{PK}$
Log. Strain → ε=ln(**U**)
Deformed Placement:
C. sys. → (x,y)
Stress → **T**
Log. Strain → ε=ln(**V**)
F=RU=VR
2
α
P
1
2
α
P
1
X
X₀
$\mathcal{B}_t$
$\mathcal{B}_0$
Material coordinates:
C. sys. → (1,2)
$\mathbf{T}|_{mat}=(\mathbf{R}|_{mat}^T\,\mathbf{R}^T)\mathbf{T}(\mathbf{R}\,\mathbf{R}|_{mat})$
$\varepsilon|_{mat}=(\mathbf{R}|_{mat}^T\,\mathbf{R}^T)\varepsilon(\mathbf{R}\,\mathbf{R}|_{mat})$
x

Figure 4.1: Kinematic of material body finite strains, reference and current placement, rota- tion of the material axes and corresponding stress and strain tensors.

In the Euclidean space, finite deformation theory imposes the distinction between the reference placement $\mathcal{B}_0$ of material body and its current placement $\mathcal{B}_t$ at time t due to application of surface loads $\boldsymbol{t}$ and body forces $\boldsymbol{b}$. Considering a single material point P (Figure 4.1), its position in the reference configuration is indicated by vector $\boldsymbol{x}_0$, while its placement in the current configuration is denoted by position vector $\boldsymbol{x}$. So, it is possible to map the position of material particle defining the displacement vector as:

$$\boldsymbol{u}(\boldsymbol{x}_0, t) = \boldsymbol{x} - \boldsymbol{x}_0 \tag{4.1}$$

in this way it is possible to define the deformation gradient $\mathbf{F}$ with respect to reference configuration:

$$\mathbf{F} = \nabla \boldsymbol{u}(\boldsymbol{x}_0, t) + \mathbf{I}\,. \tag{4.2}$$

Moreover, polar decomposition allows to separate the pure deformation from the rotational part, introducing the rotational tensor $\mathbf{R}$, the Right Cauchy-Green tensor $\mathbf{U}$ and Left Cauchy-Green tensor $\mathbf{V}$:

$$\mathbf{F} = \mathbf{RU} = \mathbf{VR}\,. \tag{4.3}$$

The Principle of Virtual Work, thus, represents the integral form of mechanical equilibrium and, given an arbitrary kinematically admissible vector field $\delta \boldsymbol{u}^*$, it can be written as:

$$\int_{\mathcal{B}_t} \mathbf{T} \colon \delta\mathbf{D}^* dV + \int_{\mathcal{B}_t} \rho \boldsymbol{a} \cdot \delta \boldsymbol{u}^* dV = \int_{\partial\mathcal{B}_t} \boldsymbol{t} \cdot \delta \boldsymbol{u}^* dA + \int_{\mathcal{B}_t} \boldsymbol{b} \cdot \delta \boldsymbol{u}^* dV \tag{4.4}$$

where $\mathbf{T}$ indicates the Cauchy stress tensor, $\boldsymbol{a}$ the acceleration vector and $\delta\mathbf{D}^*$ the virtual stretch tensor, viz.:

$$\delta\mathbf{D}^* = \frac{1}{2}(\nabla \delta \boldsymbol{u}^* + \nabla^T \delta \boldsymbol{u}^*)\,. \tag{4.5}$$

However, it is also common to express the Principle of Virtual Work at large strains in terms of Virtual Power, defining the $\delta \boldsymbol{u}^*$ as virtual velocity field and, consequently, $\delta\mathbf{D}^*$ as virtual stretch rate tensor.

In such problems it is often convenient to write Eq. 4.4 with respect to reference configuration $\mathcal{B}_0$ using the Lagrangean description. Therefore, assuming absence of body forces and acceleration, the Principle of Virtual Work can be rewritten in the following equivalent form:

$$\int_{\mathcal{B}_0} {}_1\mathbf{T}_{PK} \colon \delta\mathbf{F}^* dV = \int_{\partial\mathcal{B}_0} ({}_1\mathbf{T}_{PK} \hat{\boldsymbol{n}}_0) \cdot \delta \boldsymbol{u}^* dA\,. \tag{4.6}$$

${}_1\mathbf{T}_{PK}$ is the First Piola-Kirchhoff stress tensor, and can be calculated from the Cauchy stress tensor according to:

$${}_1\mathbf{T}_{PK} = det(\mathbf{F})\mathbf{T}\mathbf{F}^{-T}\,. \tag{4.7}$$

It it worth noting that in case of anisotropy material orientation must also be included. In particular, if deformation can be considered by employing the logarithmic Hencky strain tensor $\boldsymbol{\varepsilon} = ln(\mathbf{U})$, its definition on the material reference system can be obtained from:

$$\boldsymbol{\varepsilon}|_{mat} = \mathbf{R}|_{mat}^T(\mathbf{R}^T \boldsymbol{\varepsilon}\, \mathbf{R})\mathbf{R}|_{mat}\,, \tag{4.8}$$

where $\mathbf{R}|_{mat}$ represents the material rotational tensor; onsequently, the Cauchy stress tensor, that is calculated in the material reference frame, must be referred to the global coordinate system:

$$\mathbf{T} = \mathbf{R}|_{mat}(\mathbf{R}\mathbf{T}|_{mat}\mathbf{R}^T)\mathbf{R}|_{mat}^T\,. \tag{4.9}$$

4.3 The non-linear Virtual Fields Method

The final purpose of the VFM technique is to identify constitutive material parameters starting from heterogeneous displacement fields and loading conditions that are measured during the test. According to the plasticity framework previously introduced, a general plasticity model can be governed by a set of material parameters ξ_i, which represents, indeed, the unknowns of inverse problem. So, the following cost function can be introduced:

$$\psi(\xi_i, \delta \boldsymbol{u}^*, t) = \left| \int_{\mathcal{B}_0} {}_1\mathbf{T}_{PK} : \delta \mathbf{F}^* dV - \int_{\partial \mathcal{B}_0} ({}_1\mathbf{T}_{PK} \hat{\boldsymbol{n}}_0) \cdot \delta \boldsymbol{u}^* dA \right| \tag{4.10}$$

that is equal to zero for the exact material parameters, any admissible virtual fields and any time t, in accordance with the Principle of Virtual Work. Obviously, this equation is valid for all N_{vf} kinematically admissible virtual fields and all N_t time step of test. Thus, the following cost function $\Psi(\xi_i)$ can be built:

$$\Psi(\xi_i) = \sum_{i=1}^{N_{vf}} \sum_{j=1}^{N_t} \psi(\xi_i, \delta \boldsymbol{u}_i^*, t_j)\,. \tag{4.11}$$

The non-linear VFM theory states that identification can be performed minimising the cost function with respect to parameters ξ_i in order to ensure the equilibrium law in its weak form.

In case of anisotropic plasticity, it is common to employ several samples obtained at different texture orientations with respect to rolling direction (RD), in order to gather as much informations as possible from the testing procedure. The same principle can be exploited by the VFM, so that it is possible to build a total cost function composed by the sum of every VFM error functions from each specimen material orientation N_{mat}; it follows:

$$\Psi(\xi_i) = \sum_{k=1}^{N_{mat}} \Psi(\xi_i)_k\,. \tag{4.12}$$

Thereby, it is possible to consider different material orientations and also include more type of test to improve identification. The approach reported in Eq. 4.12 makes it so that every virtual field and specimen material orientation weights equally in the error function, condition that represent an hot-topic in the VFM research community. The influence of chosen virtual fields for the identification is still discussed [50], representing, also, one of the main propose of this research dissertation.

Chapter 5

Development and validation of new testing protocols

5.1 Introduction

The increasing interest toward advanced inverse characterization methods requires new experimental procedures able to collect a large amount of data containing crucial information about material heterogeneity and anisotropy. An example, in fact, is given by some VFM applications [46], which permits to deal with complex material behaviour and geometries thanks to the employment of full-field measurements. Among full-field optical techniques, DIC is largely widespread and probably the fastest-growing method among the last two decades. Basically the DIC measurement tracks displacement of an opportunely generated random speckle pattern on the surface of a body under certain loading conditions: if the displacement is in-plane, a single camera (2D-DIC) is sufficient; else, more cameras must be involved in the procedure in order to measure object displacement in the 3D space according to stereo-photogrammetry principles [51]. In this chapter new experimental approaches are discussed, aimed at establishing proper testing protocols to furnish the experimental data required for the inverse procedure.

The first issue investigated concerns the evaluation of volume displacement from surface DIC measurement, and represents a side project of this research activity mainly focused on the study of sheet metal behaviour. In fact, although stereo-DIC is a powerful and accurate tool to measure shape changes and surface displacement fields, with this technique it is not possible to gather information in the bulk of material, limiting the analysis only to plane-stress and plane-strain conditions. These simplifications are not properly correct in case of necking phenomenon due to plastic deformation, or for the calibration of ductile damage models [52, 53]. The volume deformation of solids can be measured experimentally using Digital Volume Correlation (DVC) [54, 55], which presents some limitations: it needs expensive and complex equipments like x-ray tomography, the analysed material must have a random internal pattern like foams or composites, and the correlation algorithm is computationally time consuming. Also magnetic resonance elastography and magnetic resonance images are involved in volume deformation measurement, albeit their use is limited to biological tissue and for most of materials with engineering application (metals, polymers, etc.) these techniques cannot be employed.

So, starting from the work of Rossi and Pierron [56], a method involving Bézier curves able to reconstruct volume deformation from surface DIC measurement is applied to experimental data coming from a tensile test on round-section specimen.

The second studied experimental approach concerns the development of new test for characterization of sheet metals through-thickness behaviour. In fact, sheet metals often exhibit preferential orientations in their texture due to rolling production process, that plays, also, a really important role in subsequent metal forming applications. Although only the planar components in the RD-TD plane of anisotropy are usually considered in constitutive modelling due to assumption of plane stress condition, the through-thickness shear behaviour can be relevant in the prediction of failure modes and plastic instabilities. Several 3D anisotropic plasticity models were developed among the years [12, 57, 58, 10], and their calibration is getting increasing interest from the research community, working on methodology and design of appropriate specimens. For example, in [35] a general procedure to retrieve material parameters for the 3D Hill48 model using the VFM on numerical data is described; [59] deal with geometry optimization of cruciform specimen for biaxial-stress state; also, Denys et al. [60] reported an application of stereo-DIC for the identification of 3D Hill48 yield surface through FEMU technique, where a double perforated specimen with a 10 mm thickness is introduced. However, when these 3D material models are employed on metal sheets, it is often a common procedure to assume the through-thickness parameters are equal to the isotropic case, and then to calibrate the others.

So, in the second section, the VFM method is used to assess feasibility of a new experimental protocol for testing through-thickness anisotropic behaviour of sheet metal. The idea took place extending the *Unnotched Iosipescu* test [61, 47] to large strains, using 2D-DIC for the thickness surface displacement measurement. After a first numerical study that was made by assuming plane stress condition, simulated experiments [62, 63] are employed to verify metrology and identification performances via VFM on thin sheet metal specimen.

Finally, the last section is dedicated to one of the former research activities of the author, which concerns the shape optimization of specimen for elasto-plastic material characterization. The study took place from the work of Badaloni [64], where a numerical simulator of experiments involving DIC is built to assess the impact of specimen geometry for the calibration of isotropic plasticity material model via VFM. This, in fact, can become an useful instrument to improve the DIC testing set-up as both diagnostic and improving tool. Since the protocol was limited only to numerical results, here an experimental validation is provided to investigate the goodness of this numerical simulator.

5.2 Evaluation of volume displacement from surface DIC measurement

In this section it is reported the application of a new algorithm for volume displacement field reconstruction from surface measurements for a solid that undergoes to large deformation. Basically, the method, called Internal Mesh Generation (IMG), is founded on the production of internal nodal points. Their position in the 3D space changes according to surface informations, and in the proposed formulation it can be applied only to basic geometries as cylinder or parallelepiped.

Let's consider a cylindrical shape specimen, at the initial condition the measurement points are distributed on a regular cylindrical grid on the 360° external surface (Figure 5.1). Placing the coordinate system so that z-axis coincides with cylinder axis, the cylindrical mesh identifies in the x-y plane k circumferences, each one composed by n points. So, for each circumference, two opposite points $\mathbf{N}_A$ and $\mathbf{N}_B$ are taken, such that $m = n/2$ pairs of $(\mathbf{N}_A^{(i)}, \mathbf{N}_B^{(i)})$ with $i = [1, \ldots, m]$ are defined.

In order to generate the internal mesh, the method exploits quadratic Bézier curves defined starting from three points, which are $\mathbf{N}_A^{(i)}$, $\mathbf{N}_B^{(i)}$ and a point $\mathbf{P}$ inside the volume. The resulting curve $\mathbf{B}(a)$ is described by the following equation:

$$\mathbf{B}(a) = (1-a)^2\mathbf{N}_A + 2(1-a)a\mathbf{P} + a^2\mathbf{N}_B \tag{5.1}$$

where a is a parameter that varies from 0 to 1, so that $\mathbf{B}(0) = \mathbf{N}_A^{(i)}$ and $\mathbf{B}(1) = \mathbf{N}_B^{(i)}$. An important property of quadratic Bézier curves is that the curve is tangent to segment $\overline{\mathbf{N}_A^{(i)}\mathbf{P}^{(i)}}$ at the starting point $\mathbf{B}(0)$ and to segment $\overline{\mathbf{N}_B^{(i)}\mathbf{P}^{(i)}}$ at the end point $\mathbf{B}(1)$.

The internal point $\mathbf{P}^{(i)}$ is defined as the intersection between the straight line connecting points $\mathbf{N}_A^{(i)}$ and $\mathbf{N}_B^{(i)}$ and intersecting cylinder axis. In the initial configuration, since $\mathbf{N}_A^{(i)}$ is opposite to $\mathbf{N}_B^{(i)}$, coordinates of point $\mathbf{P}^{(i)}$ are:

$$\mathbf{P}^{(i)} = \frac{\mathbf{N}_A^{(i)} + \mathbf{N}_B^{(i)}}{2} \tag{5.2}$$

and the resulting Bézier curve is a straight line from $\mathbf{N}_A^{(i)}$ to $\mathbf{N}_B^{(i)}$.

In deformed configuration, instead, each cylinder section can change is aspect ratio, and two important considerations must be taken:

- The cylinder axis is not so straightforward to determine; for example, in this dissertation the algorithm described in [65] is used in order to determine the axis of cylindrical body from point clouds.
- two different points $\mathbf{P}_A^{(i)}$ and $\mathbf{P}_B^{(i)}$ are obtained depending on the surface perpendicular vectors in $\mathbf{N}_A^{(i)}$ and $\mathbf{N}_B^{(i)}$ (Figure 5.1).

If $\hat{\mathbf{n}}_A^{(i)}$ and $\hat{\mathbf{n}}_B^{(i)}$ are the normals to specimen surface in $\mathbf{N}_A^{(i)}$ and $\mathbf{N}_B^{(i)}$ respectively, according to geometrical considerations, it follows:

$$\mathbf{P}_A^{(i)} = \mathbf{N}_A^{(i)} - \frac{\left|\mathbf{N}_A^{(i)} - \mathbf{N}_B^{(i)}\right|^2}{2\left(\mathbf{N}_A^{(i)} - \mathbf{N}_B^{(i)}\right)\cdot\hat{\mathbf{n}}_A^{(i)}}\hat{\mathbf{n}}_A^{(i)} \tag{5.3}$$

$$\mathbf{P}_B^{(i)} = \mathbf{N}_B^{(i)} - \frac{\left|\mathbf{N}_B^{(i)} - \mathbf{N}_A^{(i)}\right|^2}{2\left(\mathbf{N}_B^{(i)} - \mathbf{N}_A^{(i)}\right)\cdot\hat{\mathbf{n}}_B^{(i)}}\hat{\mathbf{n}}_B^{(i)} \tag{5.4}$$

where $\cdot$ is the scalar product. Point $\mathbf{P}^{(i)}$ is finally computed as:

$$\mathbf{P}^{(i)} = \frac{\mathbf{P}_A^{(i)} + \mathbf{P}_B^{(i)}}{2} \tag{5.5}$$

It may be noted that, if the deformation of the two surfaces was symmetrical, as theoretically occurs in necking of isotropic materials, $\mathbf{P}_A^{(i)}$, $\mathbf{P}_B^{(i)}$ and $\mathbf{P}^{(i)}$ would be coincident. However, this is not usually true because of the measurement errors and the possible anisotropic behaviour of the material.

For each load step, a different Bézier curve is generated for each pair of points in the two faces. According to Bézier curve theory, parameter a identifies a specific point of curve $\mathbf{B}(a)$. We assume that a given point is identified by the same value of a during deformation, *i.e.* its position can be tracked at different steps of the test using the same a in the corresponding curve. This assumption was found to be reasonable following the reconstruction validation presented later on using numerical models. Similar approaches, indeed, can be found in the literature in [66, 67] for necking and strain localization.

Choosing a suitable number of internal points, a 3D mesh can be assembled where the position of each node is known for every step of the test. If $\mathbf{X}_0$ is a point in the initial configuration and $\mathbf{X}_1$ is the corresponding point in the deformed configuration, the displacement vector $\mathbf{u}$ is:

$$\mathbf{u} = \mathbf{X}_1 - \mathbf{X}_0 \tag{5.6}$$

The displacement and strain fields inside the body can be retrieved using 3D shape function similarly to FEM analysis.

Initial cylindrical configuration

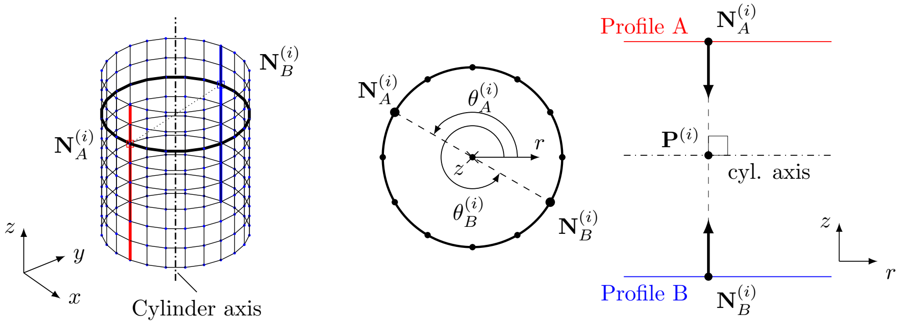
$\mathbf{N}_B^{(i)}$
$\mathbf{N}_A^{(i)}$
z
y
x
Cylinder axis
$\mathbf{N}_A^{(i)}$
$\theta_A^{(i)}$
r
z
$\theta_B^{(i)}$
$\mathbf{N}_B^{(i)}$
Profile A
$\mathbf{N}_A^{(i)}$
$\mathbf{P}^{(i)}$
cyl. axis
z
r
Profile B
$\mathbf{N}_B^{(i)}$

Final deformed configuration

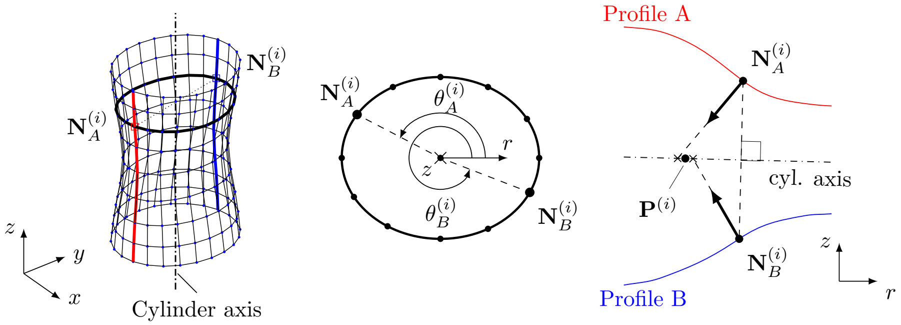
$\mathbf{N}_B^{(i)}$
$\mathbf{N}_A^{(i)}$
z
y
x
Cylinder axis
$\mathbf{N}_A^{(i)}$
$\theta_A^{(i)}$
r
z
$\theta_B^{(i)}$
$\mathbf{N}_B^{(i)}$
Profile A
$\mathbf{N}_A^{(i)}$
cyl. axis
$\mathbf{P}^{(i)}$
$\mathbf{N}_B^{(i)}$
z
r
Profile B

Figure 5.1: Application of the IGM method for cylindrical geometry.

5.2.1 Numerical validation

The proposed reconstruction algorithm is based on pure geometrical information (*i.e.* surface displacement and local curvature). In order to evaluate its accuracy when applied to real experiments, the method was first validated using 3D numerical simulation, for which the whole volume deformation history is known. In particular, the test cases simulate the necking evolution in specimens under severe plastic deformation.

Numerical model of cylindrical specimen with an initial radius of 25 mm was built up using the commercial FE software Abaqus/Standard, adopting 8-nodes brick elements and a constitutive law that describes the behaviour of a metal with high ductility and anisotropy. The Hill48 yielding function [18] was used to describe the yield locus and the Swift power law adopted to describe the stress-strain hardening curve.

	Mesh:
Elements	26564
Nodes	29216
Element type	C3D8R
	Constitutive law:
Yielding	Hill48
	$R_0 = 1.8$, $R_{45} = 1.5$, $R_{90} = 2.2$
Hardening	Swift law
	$\bar{\sigma} = 700 + 1200\,\bar{\varepsilon}$

Table 5.1: Mesh details and material parameters used in the finite element model.

Mesh information and the input constitutive parameters are listed in Table 5.1, while the FE model in initial and deformed configuration is illustrated in Figure 5.2. Severe necking occurs at the centre of specimen, and maximum strain is obtained in the bulk so that it cannot be directly evaluated by surface measurements. Moreover, effect of anisotropic material behaviour is particularly evident since deformation is not axisymmetric and the necking section is elliptical.

The IMG method was used to calculate the internal displacement and strain fields that were compared to their numerical counterparts obtained from the FEM analysis. Therefore, only the volume where necking occurs was reconstructed, that is composed by 9 lines of nodes along the axial direction while 24 nodes along the circumference.

Results of IMG method application are illustrated in Figure 5.3 for three section planes. Plane z-x represents a longitudinal section of the specimen across the major axis of the neck, plane z-y a longitudinal section across the minor

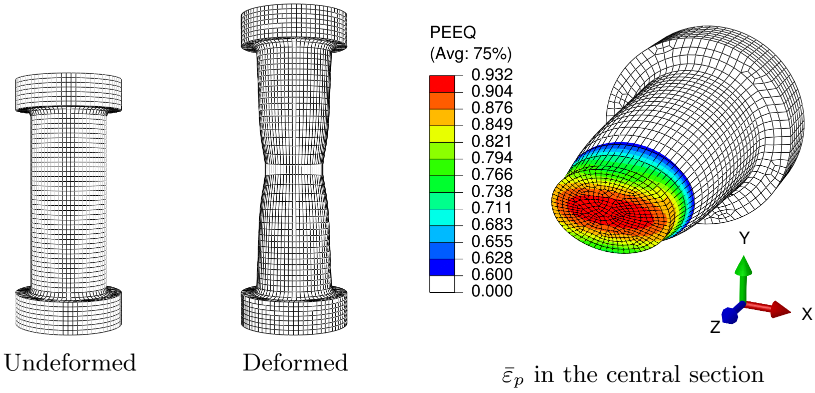
PEEQ
(Avg: 75%)
0.932
0.904
0.876
0.849
0.821
0.794
0.766
0.738
0.711
0.683
0.655
0.628
0.600
0.000
Y
Z
X

Undeformed Deformed $\bar{\varepsilon}_p$ in the central section

Figure 5.2: FE models used in numerical validation. The central cross section reveals the strain localization within the necking zone.

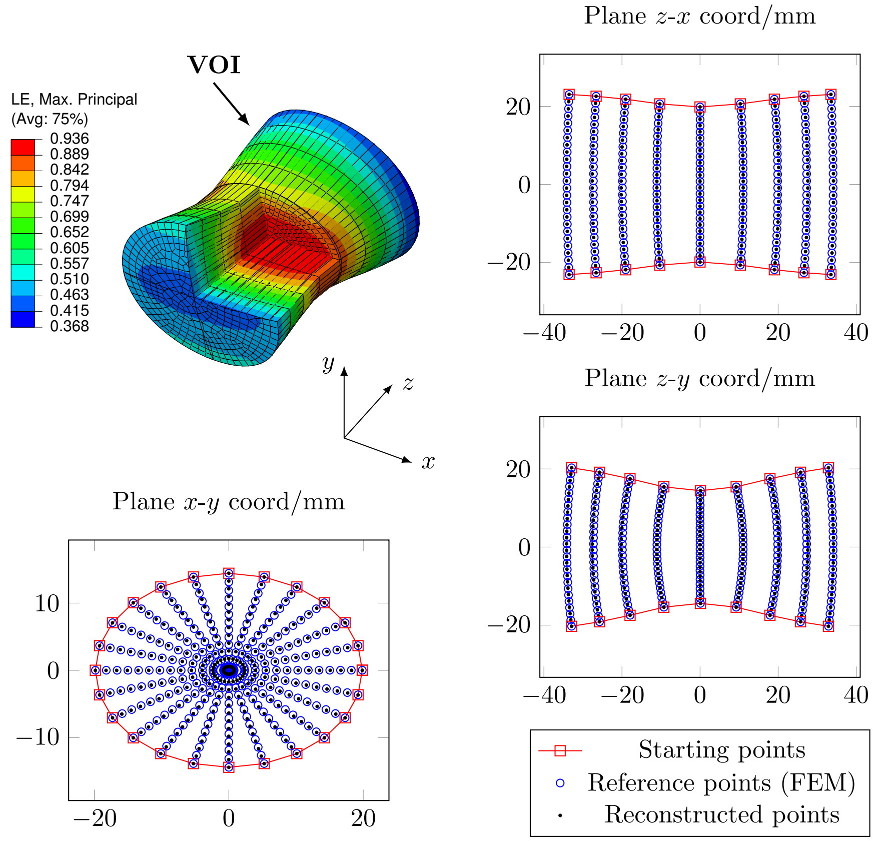

Figure 5.3: Comparison of reconstructed internal points with the FEA reference data for the cylindrical specimen.

axis of the neck and plane x-y a cross section in the central part of the neck. The internal nodes were derived following the procedure previously described, using 26 internal points for each Bézier curve. In this case, there is not direct correspondence between internal FE nodes and the reconstructed points. As depicted in Figure 5.3, the IMG method for cylindrical specimens produces a distribution of points in the section perpendicular to the axis (see Plane x-y) that is not compatible with a suitable FEA mesh, because the elements in the central zone would have a distorted aspect ratio. The FEA model was therefore built up using an optimal regular mesh, see Figs. 5.2 and 5.3.

To allow a quantitative comparison, the displacement field of the FE nodes was remapped according to the position of reconstructed points, using the *scatteredInterpolant* interpolation function implemented in MATLAB®. If $\mathbf{X}_{\mathrm{FEA}}$ are the coordinates of the FEA nodes in the VOI, $\mathbf{X}_0$ the coordinates of the IMG points in the initial configuration, $\mathbf{u}_{\mathrm{FEA}}$ the displacement field from FEA and $\mathcal{I}$ the interpolation function, it follows:

$$\mathbf{u}_{\mathcal{I}} = \mathcal{I}\left(\mathbf{u}_{\mathrm{FEA}}, \mathbf{X}_{\mathrm{FEA}}, \mathbf{X}_0\right) \tag{5.7}$$

and

$$\mathbf{X}_{\mathrm{Ref}} = \mathbf{X}_0 + \mathbf{u}_{\mathcal{I}} \tag{5.8}$$

where $\mathbf{X}_{\mathrm{Ref}}$ are the points used to make the comparison of Figure 5.3.

A fairly good agreement was found, with an average positioning error of 0.09 mm (±0.08 standard deviation).

The accuracy in terms of strain evaluation is reported in Figure 5.4, where the first plot shows the two sets of data in the central section of the specimen for two paths along major and minor axes of the elliptical section, respectively. A reasonably good agreement was found. In particular, it is worth noting that the increase of strain in the central point with compared to the surface is +10% for the major axis and +25% for the minor axis.

The second plot of Figure 5.4 shows the maximum principal strain evaluated along three paths in the axial direction. In particular, the labels "x-side" and "y-side" refer to paths on the external surface of the specimen, while the label "Inner part" refers to the strain evaluated along the central axis of the specimen. Again, a good agreement is obtained using the reconstruction algorithm. The graph clearly shows how, in the necking zone, the state of deformation in the inside of the specimen is largely different from what is observed over the surface and, if the material is anisotropic, a large difference also occurs at different angular positions along the specimen circumference.

Results from the numerical validation demonstrate that the reconstruction algorithm is able to describe with a reasonable accuracy the internal displacement and strain field in the necking zone, although purely based on geometrical surface

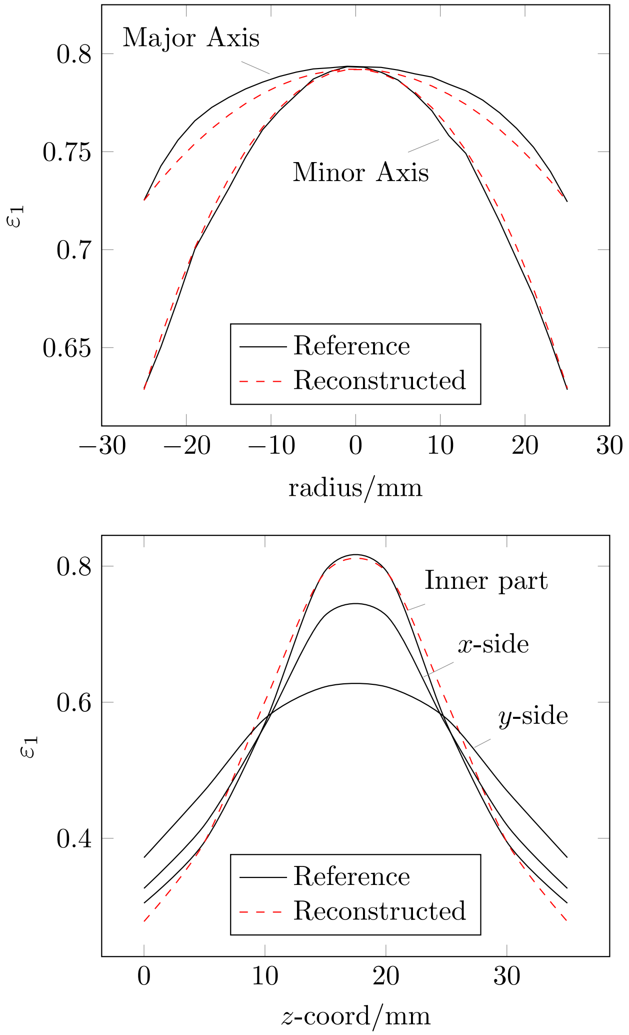

Figure 5.4: Comparison of the strain field evaluated in the necking zone of specimen with the reconstruction method. Two paths in the central section and a path in the axial direction are depicted.

data. The validation was carried out by considering non trivial case studies including severe necking and anisotropic materials. In order to check if the level of accuracy is sufficient to use the IMG method for material characterization, the reconstructed strain field should be used to identify the material properties through an inverse method like the VFM or FEMU.

In the following section, the results of the IMG method applied to real experiments are reported and discussed.

5.2.2 Application on experimental data

The presented procedure of displacement and strain 3D fields reconstruction is, thus, extended to experimental data. Cylindrical specimen, was tested with the special 360° DIC arrangement represented in Figure 5.5. A single camera (Nikon7100, 4000×6000 pixel resolution, equipped with a Nikkor 60mm Micro lens, used at f/16) was mounted on a slewing ring in order to capture multiple pictures of the specimen at different angles. The specimen was a cylindrical sample of Grade X100 steel with an initial diameter of 8 mm. So, the camera, moving on the sledge, capture pictures every $\alpha \cong 26°$ providing 14 images for the whole revolution. Considering two consecutive images, the angle is opportunely imposed to obtain a sufficient overlapping between the two measurement ROI. In this way, applying an fixed cylindrical calibration target on the base of specimen, the stereo-DIC measurement is done on the 360° surface. More details of this experimental technique including the related error analysis are reported in [68].

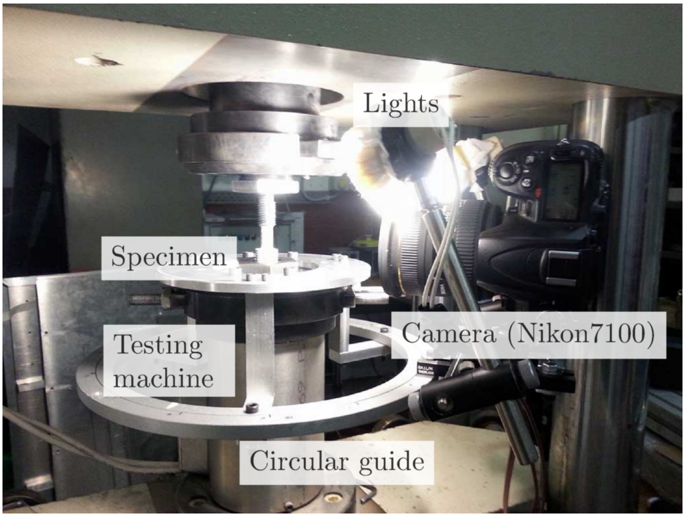

Figure 5.5: Experimental set-up with 360° DIC acquisition equipment.

In this case, to accurately reconstruct the surface displacement field, the commercial software *MatchID* (`www.matchidmbc.be`) was used to perform large deformation DIC measurement. Results in term of vertical displacement are depicted in Figure 5.6.

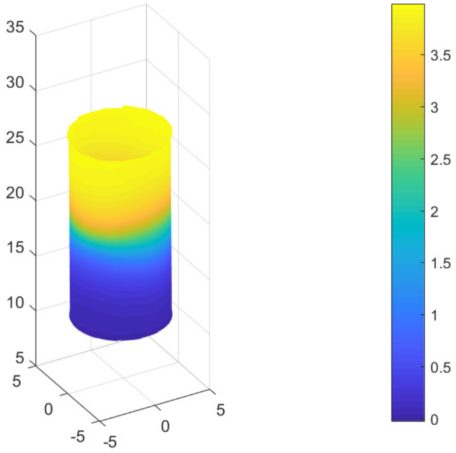

Figure 5.6: Vertical displacement obtained from 360°-DIC measurement.

As result of the stereo-DIC analysis, a set of measurement points with coordinates $\mathbf{X}_{DIC}$ and the corresponding 3D displacement field $\mathbf{u}_{DIC}$ were obtained. These data were not directly used for the IMG method but they were first regularized using, again, the *scatteredInterpolant* [38] MATLAB® interpolation function.

Volume reconstruction procedure can be distinguished in the following steps:

1. A regular grid of points with coordinates $\mathbf{X}_{S0}$ was defined over the specimen surface in the undeformed configuration. The displacement field $\mathbf{u}_{DIC}$ obtained from DIC was mapped over the regular grid using the interpolation function $\mathcal{I}$:

$$\mathbf{u}_{S0} = \mathcal{I}\left(\mathbf{u}_{DIC}, \mathbf{X}_{DIC}, \mathbf{X}_{S0}\right) \tag{5.9}$$

   where $\mathbf{u}_{S0}$ is the resulting displacement field. The coordinates $\mathbf{X}_{S1}$ of the grid points after deformation are obtained as:

$$\mathbf{X}_{S1} = \mathbf{X}_{S0} + \mathbf{u}_{S0} \tag{5.10}$$

2. The reconstruction algorithm previously introduced was used to obtain

the internal points $\mathbf{X}_{V0}$ and $\mathbf{X}_{V1}$ starting from the corresponding surface points. The volume displacement field $\mathbf{u}_{V0}$ was then derived as:

$$\mathbf{u}_{V0} = \mathbf{X}_{V1} - \mathbf{X}_{V0} \tag{5.11}$$

3. As a final step, the volume displacement $\mathbf{u}_{V0}$ was projected over a 3D mesh of the specimen obtained using the mesh generator of Abaqus. The displacement $\mathbf{u}_N$ of each node was obtained from the reconstructed displacement field using the interpolation function:

$$\mathbf{u}_N = \mathcal{I}\left(\mathbf{u}_{V0}, \mathbf{X}_{V0}, \mathbf{X}_N\right) \tag{5.12}$$

where $\mathbf{X}_N$ are the coordinates of the nodes. The FEA software was then used as post-processing tool to display the 3D displacement and strain fields. It must be underlined that no computation was performed, and displayed results are relative to IMG method.

Therefore, the number of points corresponding to the different steps are listed in Table 5.2. A very dense point cloud was obtained from the 360° measurement. Such points were used to reconstruct a regular grid of 28×29 points, in the θ and z directions, respectively. Then 8932 points were generated with the IMG method and they were used to retrieve the deformation of the 8410 nodes of the solid mesh.

Number of points			
stereo-DIC	regular grid	IMG method	solid mesh
629104	812 (28×29)	8932	8410

Table 5.2: Number of points used in the various steps of the reconstruction process.

The reconstructed undeformed and deformed shapes of the cylindrical specimen are illustrated in Figure 5.7. In this case, the VOI is a central zone of 13.5 mm in length. At the considered deformed stage, a 17.47 mm longitudinal length was reached and a well developed localized necking was clearly visible in the central portion of the specimen.

Because of the material anisotropy, the shape of the neck is not symmetrical. The strain localization inside the sample is shown in Figure 5.8 where the strain field over two of its cross sections is reported. As expected, the deformation contour pattern is not axi-symmetrical and the maximum strain is obtained in the centre of the specimen. The principal maximum strain along different radial paths is plotted in Figure 5.9. In particular, three paths are shown, one along

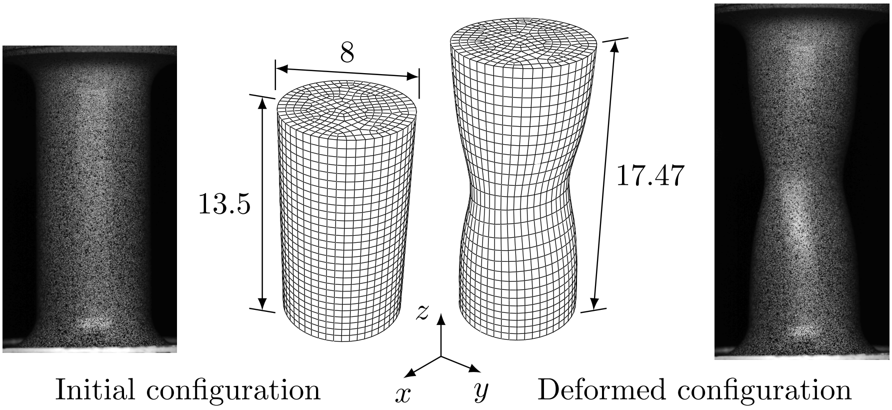

Figure 5.7: Three-dimensional reconstruction of the deformation of the cylindrical specimen and pictures of the specimen.

the major axis of the neck section, one along the minor axis and one at 45° with respect to the major axis. Depending on the considered angular position, the strain increase in the centre compared to the surface ranges from +15% to almost +50%.

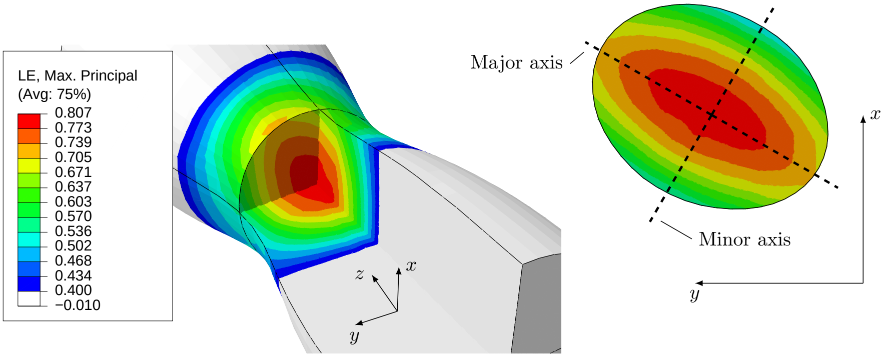

Figure 5.8: Strain distribution across two orthogonal cross sections of the specimen showing the strain concentration at its centre.

In conclusion, the IMG method is a suitable instrument to investigate strain localization phenomenon such as necking, and also can be potentially applied in a large number of case-study of engineering interest. However, in order to obtain acceptable results, some important remarks must be taken into account. First, raw displacement data from the full-field measurement cannot be used directly, and preprocessing tools like smoothing and remapping of data into regular grid are necessary. Employment of interpolation functions, indeed, requires a dense

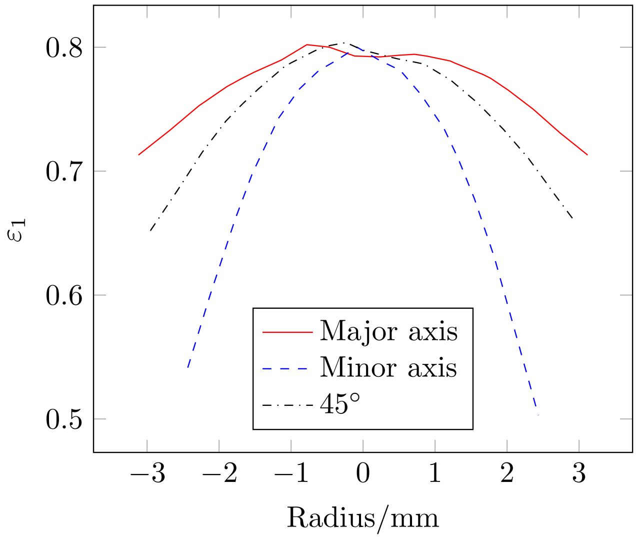

Figure 5.9: Plots of the principal strain along three different radial paths in the central section of the specimen.

distribution of measurement points to reduce interpolation error when regular grid is generated. Moreover, the method is mesh-dependent, so an opportune and regular mesh size should be chosen.

Regarding further implementations, the final scope for this proposed protocol is represented by its application to material properties characterization, so a deep study on reconstruction error on material identification should be performed using, for instance, simulated experiments.

5.3 Experimental test for sheet metals through-thickness behaviour characterization

Iosipescu test [69, 70] is nowadays a common standard for studying the shear properties of composite materials in the field of linear elastic anistropy, and in literature several applications [71, 70] are reported. Basically, this kind of test involves a V-notched specimen with appropriate fillets that is hold on one side by a fixed jaw while the other is clamped by a second jaw that can move only vertically, permitting to generate a bending and shear load on specimen. Also, a second version was proposed by Pierron et al. [72, 61], where the two notches are removed from the specimen.

Starting from these principles, this kind of shear test is redesigned considering, first, the subsequent design requirements:

- Experimental apparatus must contain thin metal sheet specimen;
- Large deformation regime must be reached, taking care of clamping system effects on strain localization due to bending moment;
- Measurement area must guarantee enough field of view for the full-field technique (in this case 2D-DIC).

Thus, the first step is to determine the dimension of the specimens to be used. In order to respect the latter requirement keeping the dimensional characteristics of sheet metal, a thickness of 2 mm is chosen, while length is setted to 44 mm; moreover, specimen width is a crucial feature for plane stress or plane strain condition, and in the present study it is imposed to 5 mm assuming plane stress state.

Once specimen dimensions are defined, the relative clamping system is planned employing two twin jaws of 20 mm length opportunely equipped with fillets to avoid excessive indentation due to bending. So, the opening area between the two clamps was setted imposing a maximum bending angle of 30° and 2 mm of maximum vertical displacement for the moving jaw.

5.3.1 FE analysis on numerical 2D model

FEA approach [73] is a powerful tool to assess system feasibility, so, a numerical model reproducing the testing apparatus was realised in ABAQUS-Standard® environment. In Figure 5.10 all geometrical specifications of testing apparatus introduced in the model are displayed; the fixed clamp was assumed to be composed by two rigid body parts: the lower one, provided with fillet on right side to drive specimen deformation, and the upper one that prevents sheet metal to rotate operating as an holder. The right-side clamp, that is capable of translating vertically, was modelled with only one rigid body having analogous dimensions of the left-side jaw. It is worth noting that fillet radius and length can have an important role in the stress field and also to avoid convergence problems in the simulation due to excessive element distortion, so these two geometrical parameters were tried iteratively, finding adequate results for configuration with radius equal to 2 mm and length of 1 mm.

Sheet metal specimen with the previously reported dimensions was modelled including a geometric partition in the middle area that is subjected to DIC measurement, aimed to increase number of elements. In this way, the model contains 3200 elements with approximatively 0.1×0.05 mm size in the middle partition, and 1440 ones having 0.1×0.5 mm dimensions for the rest of specimen. Moreover, the measurement zone was modelled using full-integration 4-nodes bilinear element type CPS4 in order to avoid the shear-locking issue due to the combination of bending and shear load, while the rest of the adopted

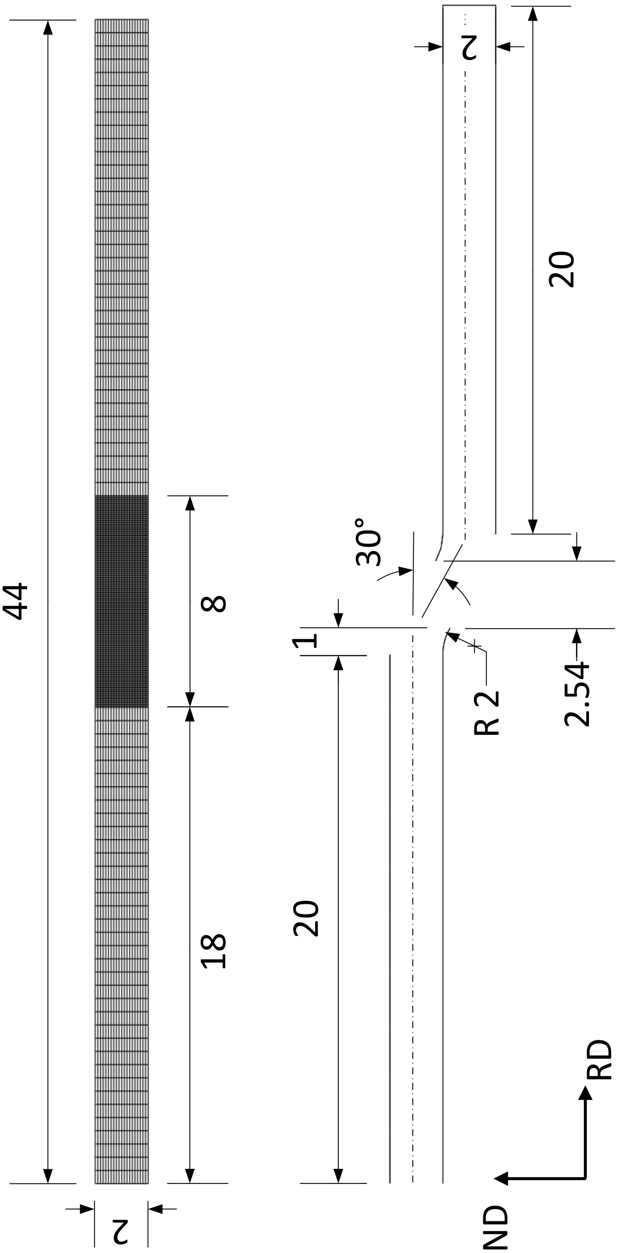
44
2
8
18
20
2
20
30°
1
R 2
2.54
RD
ND

Figure 5.10: Experimental apparatus and specimen specifications for metal sheet through-thickness testing used in FEA. Dimensions are in mm.

specimen reduced integration 4-nodes bilinear elements type CPS4R to reduce computational timing.

Concerning the material, isotropic hardening was considered and described by the well-known Swift Law (Eq. 3.60) and anisotropic behaviour employing the traditional Hill48 material model. Let's indicate the rolling direction *RD* correspondent with x axis, the transverse direction *TD* with y axis and normal direction *ND* with z axis, material orientation of 0° with respect to RD was assigned to specimen model considering thickness-face on xz plane. In Table 5.3 all material parameters inserted are reported, and they were taken from a general austenitic stainless-steel.

Elastic constants			
E	200 GPa		
ν	0.3		
Swift's law parameters			
K_H	1000 MPa		
ε_0	0.02		
n_H	0.5		
Lankford parameter			
R_0	2.2		
R_{45}	1.5		
R_{90}	1.8		
Anisotropy coefficents for Hill48			
f	0.3819	l	2.5000
g	0.3125	m	2.5000
h	0.6875	n	1.3889

Table 5.3: FE model constitutive parameters.

Boundary conditions were set as follows: all the parts of left jaw were fixed with an encastre while right jaw is capable of moving only vertically with an imposed displacement of 2 mm downward; moreover, the left side border of sheet metal is locked with hinge constraint. Also, the assignment of contact condition between specimen boundary and clamping system is a relevant step for a successful simulation; in this case, frictional contact was selected by considering the static friction coefficient $\mu_s = 0.16$, a typical value for steel-steel contact with lubricated surfaces.

Numerical analysis results are displayed in Figure 5.11 in terms of stresses and equivalent plastic strain for the last step of simulation for the opening zone to be submitted to VFM analysis. In particular, Figure 5.11d gives us a qualitative and quantitative insight of plastic strain field obtained, reaching in the middle of observed area values between 0.16 and 0.22. However, a local concentration of strain is present in correspondence of fillets due to bending moment, and equivalent plastic strain achieves its maximum value around 0.24.

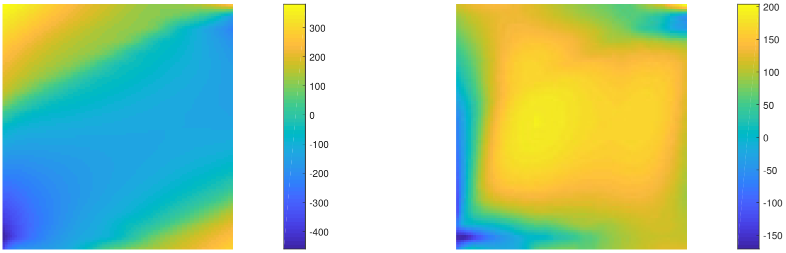

(a) σ_{xx} (b) σ_{zz}

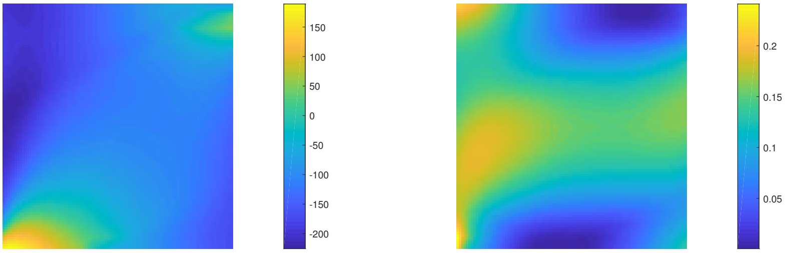

(c) σ_{xz} (d) Eq. Plastic Strain

Figure 5.11: Results of FEA simulation, calculated with respect to global reference system.

5.3.2 Synthetic images generation and DIC measurement

The experimental procedure was studied by means of simulated experiments to reproduce the whole measurement chain, as reported in [62] for the Unnotched Iosipescu test. In fact, exactness and robustness of the identification process through VFM are deeply influenced by the accuracy of displacement field measurement on the specimen's surface obtained by the full-field technique. As widely reported in literature [74, 75, 76], factors such spatial resolution, noise intensity and quality of the speckle pattern, strongly affect identification results, acting as error sources. This approach can be also used for other purposes as diagnostic tool for DIC arrangement optimization [64], and a practical applications can be found in [77] in case of polymeric foams, or in Section 5.4

inherent to metal isotropic plasticity.

So, FE analysis represents the starting point for the generation of synthetic images. The reference image, which captures the unloaded specimen in the initial step of the test, is created starting from nodal coordinates of FE model, camera sensor dimensions in pixel and a general speckle pattern; afterwards, deformed images are built deforming the reference image according to displacement vector at each pixel location. In other words, when the reference image is created, the belonging relation between each pixel and FE model elements is known, and the new position of a certain pixel can be calculated from nodal displacement field using the element shape functions. Moreover, details about the convolution procedure implemented for image deformation are reported in [78].

Hence, synthetic images coming from the numerical through-thickness test analysis were generated to reproduce an experimental apparatus equipped with one CMOS camera with 1024 × 1280 image resolution and 8-bit sensor and 50 mm lens mount. Particular attention was given to choose a reasonable speckle-pattern for the thin specimen thickness. With this intent, the reference speckle-pattern was taken from a real test image on 8 mm specimen (in particular the one described in 5.2.2), whose pattern has the peculiarity to be painted with airbrush technique, able to provide fine and small black paint dots. In this way, cutting an area of interest that has almost the same dimensions of simulated specimen. In Figure 5.12 an example of resulting synthetic reference and deformed images is represented. Obviously, with this simulating picture technique, deformed images can only display pixels that are contained in the initial picture. So, if some external nodes enter in the camera field of view due to large deformation, the corresponding pixels cannot be included.

Since in numerical simulation the total displacement was divided in 30 steps, one synthetic image was created for each step of FEA and, then, submitted to 2D-DIC measurement.

Some considerations must be taken regarding the chosen field of view for the simulated test. Approximatively, images capture an area of 3.36 mm width and 4.2 mm height, that, according to well-known pinhole theory [79], implies a distance between camera and specimen surface of around 32 mm using the aforementioned lens mount size. In these conditions 2D-DIC is extremely influenced by out of plane movement, and telecentric lens or stereo-DIC set-up are recommended to avoid this kind of experimental uncertainties. However, the aim of this study is to assess the identification goodness of the proposed experimental protocol, taking into account to guarantee an appropriate image resolution.

The 2D-DIC measurement was performed using the commercial software *MatchID*. Here, subset size was setted to 49 pixels in order to avoid correlation problems due to bigger black paint dots, while the stepsize on 3 pixel. Also,

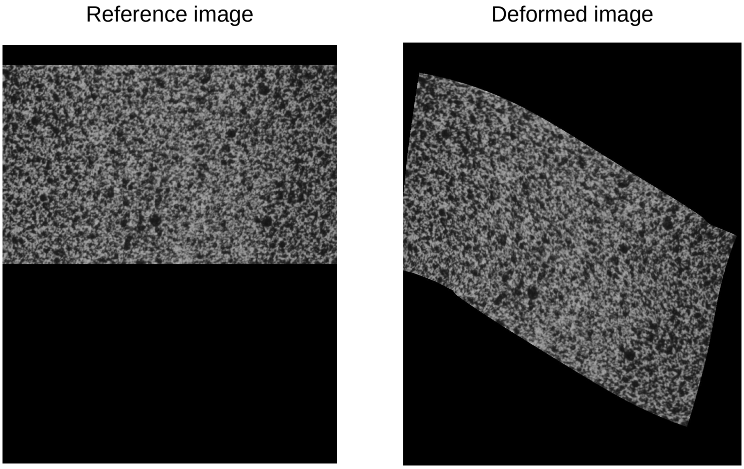

Figure 5.12: Synthetic reference and deformed images.

quadratic shape function was employed to permit full bending of subset, and ANSSD correlation criterion with bicubic spine interpolation were used for the analysis. Then, measured displacement maps were submitted to strain computation through an external routine, and results are depicted in Figure 5.13 compared to strain fields calculated from displacement FEA data. Since these synthetic images are not affected by noise, no temporal and spatial smoothing was performed for all data sets. Measuring displacement data in proximity of borders is a relevant issue for full-field techniques as DIC due to mismatching problems when the subset includes pixels outside the specimen speckle pattern; indeed, usually the AOI is taken avoiding region close to borders. The adopted DIC software, however, contains an internal algorithm for missing data compensation, and permits to extend the correlation to the whole specimen thickness. Nevertheless, there are problems in resulted computed strain exactly close to upper and lower edges, which depend on subset size. These strain errors can strongly contaminate identification results. A practical way to reduce them without compromising the equilibrium, is to correct strain fields by substituting each noisy measurement point with the closer correct one. Clearly, this strategy is admissible only when few datapoints must be corrected.

5.3.3 Application of non-linear VFM

According to the Hill48 criterion introduced in 2.3.1, the through-thickness shear behaviour is regulated by material parameter m, which also represents the final objective of the identification procedure. Thus, the non-linear VFM

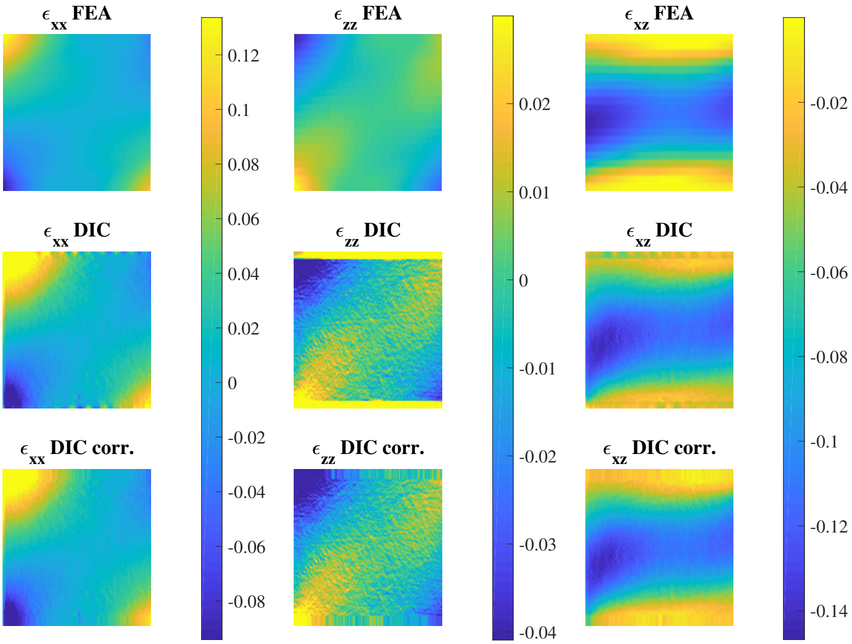

Figure 5.13: Strain fields comparison between FEA data and results from DIC measurement (raw and corrected), with subset size of 49, respect to local reference frame. Last set of images represent corrected strain fields submitted to VFM identification.

must be arranged considering that:

- Only the opening area between the two clamps is considered for strain calculation;
- Practically, only the vertical component of loading force is known;
- According to elastic Iosipescu VFM applications in literature, the virtual displacement field must be continuous.

The non-linear VFM allows to insert more virtual fields in the cost function (Eq. 4.11) in order to help its minimization, especially in case of anisotropic material properties. Usually, the virtual fields are chosen in order to minimize noise sensitivity. Among the years manual or automatically generated optimized virtual fields [80, 81] were used; here, four different virtual fields were manually inserted following the considerations reported in [47].

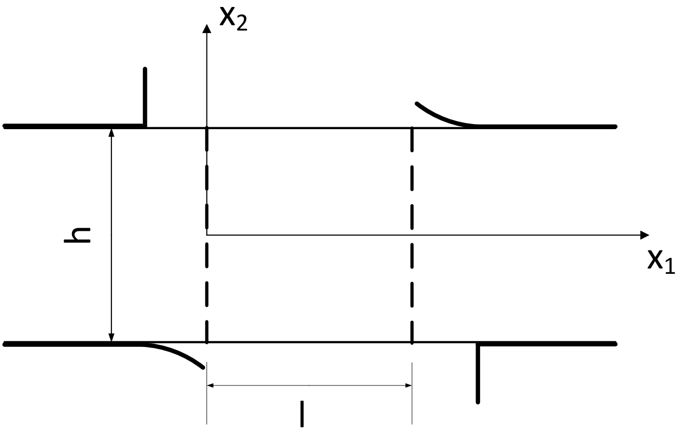

Figure 5.14: Sheet metal through-thickness test schematic view.

Under the preceding assumptions, let's consider the notation reported in Figure 5.14. The first virtual field is taken to reproduce the typical uniform shear deformation:

$$\begin{cases} \delta u_1^{*(1)} = 0 \\ \delta u_2^{*(1)} = -\frac{x_1}{l} \end{cases} \qquad \delta \boldsymbol{F}^{*(1)} = \begin{bmatrix} 0 & 0 \\ -\frac{1}{l} & 0 \end{bmatrix} \tag{5.13}$$

in this way, indeed, external virtual work $W_e^{*(1)}$ is directly dependent to vertical force F_v:

$$W_e^{*(1)} = \frac{F_v}{w}\,, \tag{5.14}$$

where w indicates the width of sheet metal specimen. It is worth noting that is case of elastic Unnotched Iosipescu test the first virtual field permits to retrieve directly elastic shear modulus G.

The second virtual field, instead, can be select considering a bending strain fields without any transverse virtual shear component. Making again a comparison with elastic Iosipescu test, this virtual field is employed to gather the elastic modulus E and Poisson ratio ν. Viz:

$$\begin{cases} \delta u_1^{*(2)} = x_1(l-x_1)x_2 \\ \delta u_2^{*(2)} = \frac{1}{3}x_1^3 - \frac{1}{2}lx_1^2 \end{cases} \qquad \delta\boldsymbol{F}^{*(2)} = \begin{bmatrix} x_2(l-2x_1) & x_1(l-x_1) \\ x_1^2 - lx_1 & 0 \end{bmatrix} \tag{5.15}$$

also for second virtual fields the external virtual work depends from vertical component of the force:

$$W_e^{*(2)} = \frac{F_v l^3}{6w} \tag{5.16}$$

Remaining virtual fields are introduced trying to enhance identification results, and they are opportunely built to give the external virtual work equal to zero. So, third virtual field $\delta\boldsymbol{u}^{*(3)}$ is defined as:

$$\begin{cases} \delta u_1^{*(3)} = 0 \\ \delta u_2^{*(3)} = x_1(l-x_1)x_2 \end{cases} \qquad \delta\boldsymbol{F}^{*(3)} = \begin{bmatrix} 0 & 0 \\ x_2(l-2x_1) & x_1(l-2x_1) \end{bmatrix}\,, \tag{5.17}$$

while the forth virtual fields $\delta\boldsymbol{u}^{*(4)}$:

$$\begin{cases} \delta u_1^{*(4)} = 0 \\ \delta u_2^{*(4)} = x_1(l-x_1)x_2^3 \end{cases} \qquad \delta\boldsymbol{F}^{*(4)} = \begin{bmatrix} 0 & 0 \\ x_2^3(l-2x_1) & 3x_1(l-2x_1)x_2^2 \end{bmatrix}\,. \tag{5.18}$$

Input data for non-linear VFM where submitted in the following order:

- Displacement and strain fields coming from FEA simulation. In this way, it is possible to give an insight on effects of strain and stress calculation method and, also, optimization algorithm capabilities;
- FEA displacement and strain fields with artificial noise addiction. This analysis, instead, permits to evaluate noise impact on parameter identi-

fication. In particular two level of noise are considered as discussed in 3.3.2;

- DIC measured displacement fields and derived strains both raw and corrected data.

The minimization of the cost function in Eq. 4.6 in this case was performed using the MATLAB® function *fmincon*, which is an optimization tool to find the minimum of a constrained non-linear multivariable problem. More details can be found in [82]. Moreover, stress state calculation was executed adopting the Direct Method widely described in 3.3. Hence, VFM identification results are reported in Table 5.4, where the starting point for optimization algorithm was chosen assuming isotropic plastic behaviour of material (i.e. $m = 1.5$).

	Identified parameter (reference $m = 2.5$)
FEA	2.566
FEA noise 10^{-4}	2.528
FEA noise 10^{-3}	2.297
DIC raw	5.093
DIC corrected	2.471

Table 5.4: Identification results via non-linear VFM for sheet metal through-thickness test.

Some interesting conclusions can be deduced. First a correct measurement of strain fields close to the specimen edge can dramatically influence identification results, and their correction - when it is possible - can help the VFM procedure. Also, adding a noise of 10^{-4}, the typical range that affects elastic deformation, does not pollute identification, confirming the effectiveness of Direct stress integration Method to deal with noise.

5.3.4 Assessment of specimen width

The plane stress state assumption was mainly addressed to generate a stress state containing the optimal information for the VFM identification. In fact, this condition guarantees that the stress fields is constant through the thickness, and the informations gathered on the specimen surface are the same in the bulk of material. However, such assumption must be verified and validated, since the specimen dimensions suggest that the generated stress state is closer to the plane strain condition. Therefore, a 3D numerical model reproducing the developed test was built in order to compare the generated stress field at different levels of specimen width. In particular, the analysis is conducted considering three layers of the specimen as depicted in Figure 5.15: the external surface, that represent the reference stress field since its corresponding strain fields are directly measured by the full-field technique, and two inner layer at 25% and 50% of the width. Moreover, this analysis is extended to three values of specimen width: 5 mm, 2 mm and 1 mm.

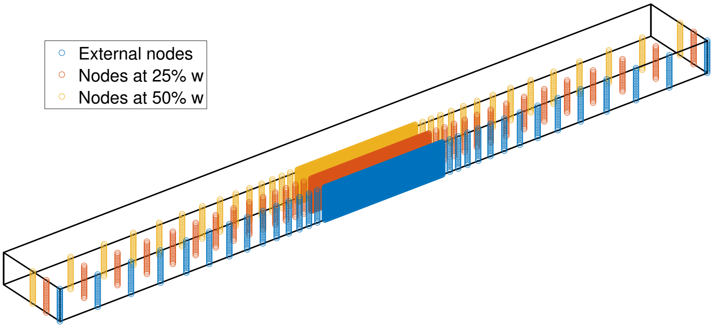

Figure 5.15: Schematic view of the selected nodes at three different levels of specimen width.

The full scale numerical model represents the extension of the 2D model previously described to the 3D through an extrusion of the four parts composing the testing set-up. So, considering the thickness plane, the same element dimensions are used, while the edges along the width direction are divided in order to have the ratio between the element size and specimen width $\Phi_w = 0.04$. Accordingly, the element size gradient, and also the number of divisions, are constant even changing the width of specimen. Thereby, the sheet metal sample is composed by 94000 8-nodes brick elements, taking care to use the full-integration type (C3D8) in the central zone of the specimen, where the deformation localizes.

Figure 5.16 displays the numerical results obtained for the 5 mm width specimen in terms of in-plane stresses generated on the external layer and their difference in MPa with the two internal layers respectively. It is worth noting that such width does not provide a pure plane stress state: the highest differences are located in the corners zones, where the bending moment and also the indentation effect due to the clamps are predominant. Here, the σ_{xz} reaches differences of almost 80 MPa, while the dissimilarities decrease in the middle area of the measurement zone.

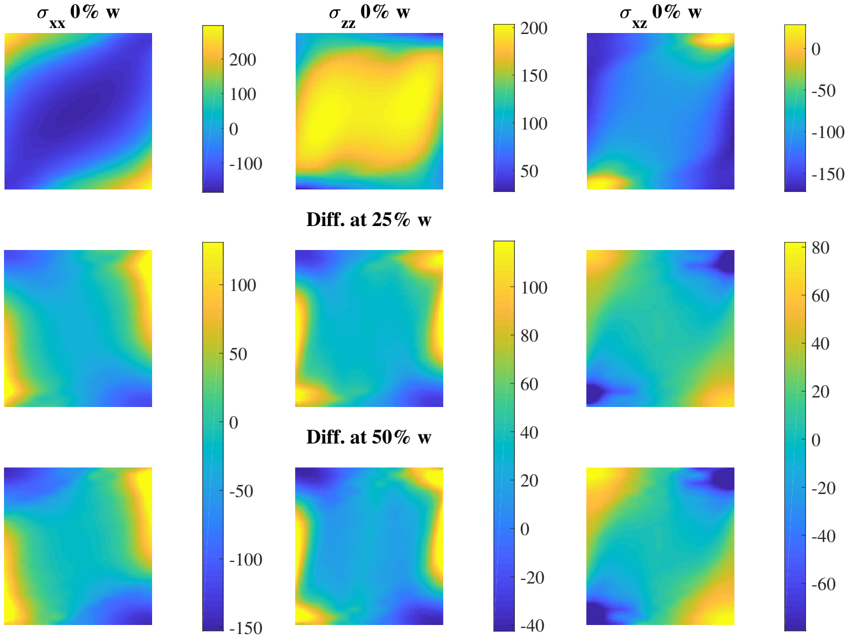

Figure 5.16: Stress fields generated on the external layer of 3D specimen having 5 mm width. The two last sets of images depict the differences with internal layers at 25% and 50% of width.

Reducing the specimen width leads the results closer to the plain stress condition. In fact, albeit the maximum difference is again around 80 MPa for σ_{xz}, the area with the highest error is less diffused (Figure 5.17). Also here, the region in the middle of the selected measurement area displays a maximum difference around $\sim$ 15 MPa, suggesting its employment for the identification via VFM as a compromise solution.

The specimen configuration with 1 mm width (Figure 5.18) gets results even more closer to the stress fields obtained for the 2D plane stress analysis reported in Figure 5.11. The differences of σ_{xx} and σ_{zz} between the outer layer and the two inner ones are the lowest, nevertheless the variance of σ_{xz} are comparable to the 2 mm width configuration. However, the 1 mm wide specimen represent a limit configuration since it can be critically affected by experimental uncertainties as out-of-plane motions when relatively high strains are achieved in a real test.

In conclusion, the proposed experimental protocol can represent an interesting

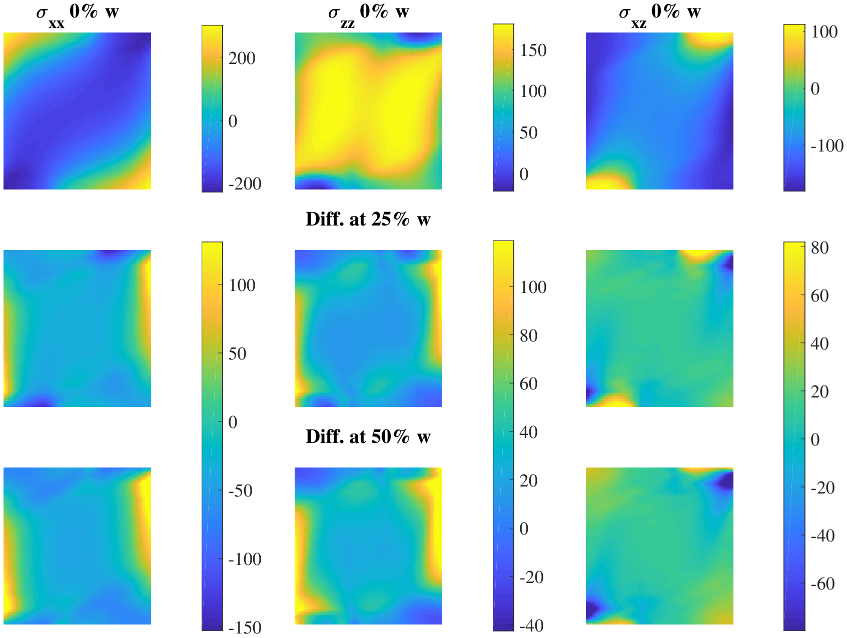

Figure 5.17: Stress fields generated on the external layer of 3D specimen having 2 mm width. The two last sets of images depict the differences with internal layers at 25% and 50% of width.

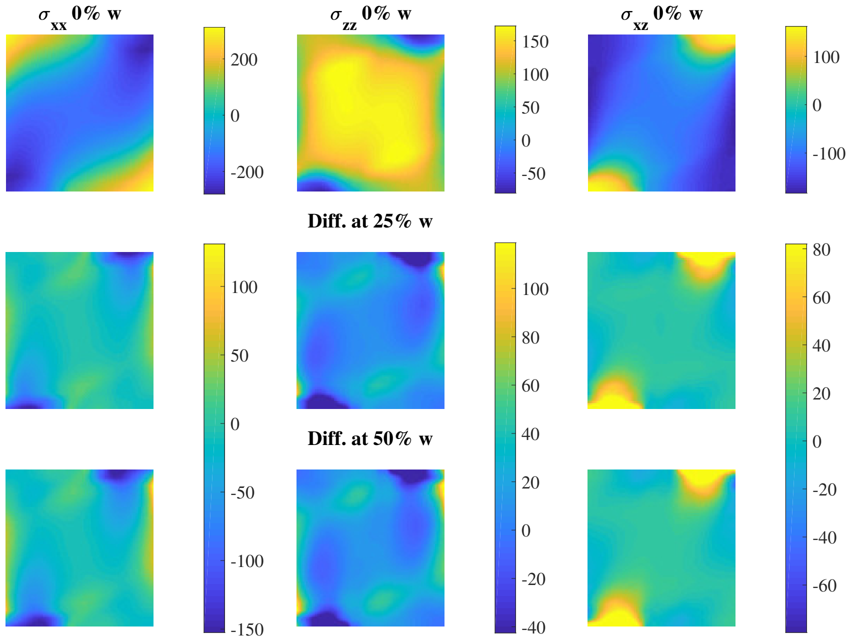

Figure 5.18: Stress fields generated on the external layer of 3D specimen having 1 mm width. The two last sets of images depict the differences with internal layers at 25% and 50% of width.

tool to study the through-thickness anisotropic behaviour of sheet metal using a 2D-DIC measurement system, permitting to identify the relative constitutive parameter for the traditional Hill48 model using the VFM inverse technique. However, this is a preliminary study regarding fundamentally the metrology point of view and the assessment of specimen width in order to generate the plane stress state recommended for the VFM identification; in fact, a width of 5 mm produces a stress state closer to the plain strain state condition, which suggests to couple the proposed testing protocol with inverse methods as the FEMU. Moreover, it would be really interesting to employ the proposed test in calibration of complex anisotropic plasticity material models as YLD2004-18p [57, 58].

5.4 Validation of numerical simulator to optimize experimental set-up for elasto-plastic material characterization

In Section 5.3 it is described an application of simulated experiments of 2D-DIC arrangement to evaluate metrology aspects and effectiveness of a new testing protocol; nevertheless, this numerical technique can represent a valid diagnostic instrument to study sought experimental set-up. An interesting version is provided to optimize the geometry of specimen that will be used for characterizing hardening behaviour of isotropic metal sheet at large strains. In literature there are several examples regarding the application of numerical procedure to specimen shape optimization, as, for instance, in [39] to calibrate the YLD2000-2D or [83] concerning the more complex YLD2004-18p. However, albeit only the simple case of isotropic von Mises material was analysed, the peculiarity of this numerical simulator is represented by the replication of the whole 2D-DIC measurement chain, including the main experimental uncertainties. The aim of this section, thus, is to provide an experimental validation to the optimization protocol described in the following.

Summarizing the procedure reported in [84], the optimization process is organised in two subsequent phases, as outlined in Figure 5.19: the simulated experiment, that produces synthetic images required in the second phase: the identification procedure. Main input is the geometry of specimen, whose features are the objects of optimization. So, the generated geometry is submitted to Finite Element analysis; since isotropic material was taken into consideration, its behaviour is determined only by a reference hardening curve, expressed, in this case, by the Swift's law. Generation of synthetic images follows the same steps described in Subsection 5.3.2 both for the reference and deformed ones. In addition, here experimental uncertainties are introduced to consider noise, rigid

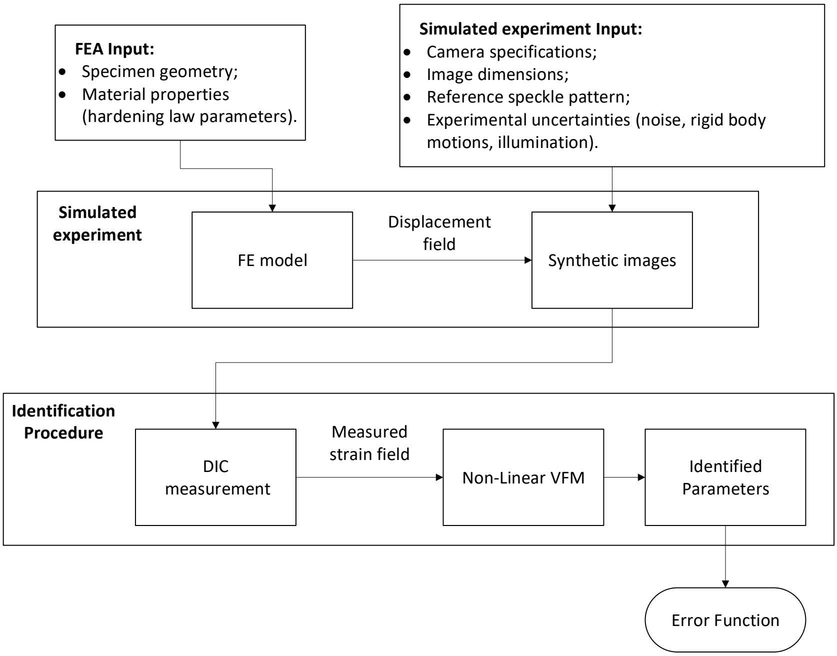
FEA Input:
Specimen geometry;
Material properties (hardening law parameters).
Simulated experiment Input:
Camera specifications;
Image dimensions;
Reference speckle pattern;
Experimental uncertainties (noise, rigid body motions, illumination).
Simulated experiment
FE model
Displacement field
Synthetic images
Identification Procedure
DIC measurement
Measured strain field
Non-Linear VFM
Identified Parameters
Error Function

Figure 5.19: Optimization process flowchart.

body motions and illumination variations. Hence, the set of created images undergoes to 2D-DIC analysis and identification is achieved by the non-linear VFM. Finally, the goodness of identification results is assessed with an error function based on the Root Mean Square Error between the reference and identified stress-strain curve, viz.:

$$RMSE = \sqrt{\frac{1}{\bar{\varepsilon}_p^{lim}} \int_0^{\bar{\varepsilon}_p^{lim}} \left(\bar{\sigma}_{ref} - \bar{\sigma}_{VFM}\right)^2}, \tag{5.19}$$

where $\bar{\varepsilon}_p^{lim}$ indicates the considered maximum equivalent plastic strain.

5.4.1 Simulated experiment and results

In this study the shape of specimen is characterized by the presence of two notches, whose geometry is regulated by 7 independent variables (h, x_L, x_R, y_L, y_R, θ_L, θ_R), as displayed in Figure 5.20. In particular, the DOI was composed by 50 different configurations, where adopted values of design variables are opportunely chosen and combined to avoid repetitions:

$$\begin{aligned}
&h \longrightarrow \{5, 10, 20\}\ [mm];\\
&\theta_L \longrightarrow \{-45, -30, 0, 45\}\ [°];\\
&\theta_R \longrightarrow \{-45, 0, 30, 45\}\ [°];\\
&x_L \longrightarrow \{1, 2.5, 5, 6, 12.5\}\ [mm];\\
&y_L \longrightarrow \{0, 5, 10, 15, 20, 25\}\ [mm];\\
&x_R \longrightarrow \{1, 2.5, 5, 6, 12.5\}\ [mm];\\
&y_R \longrightarrow \{-25, -20, -15, -10, -5, 0\}\ [mm].
\end{aligned}$$

Specimen thickness is constant and equal to 2 mm.

A Young's Modulus $E = 200$ GPa and Poisson's Ratio $\nu = 0.3$ are input in the FE model for the elastic properties, while the used parameters for the Swift's law are $K = 1000$ MPa, $\varepsilon_0 = 0.02$ and the exponent $N = 0.5$.

The numerical images are generated to reproduce an experimental set-up equipped with a CMOS camera having 1280 × 1024 resolution with 8-bit sensor, mounting a lens of 50 mm. The camera is supposed to be mounted with a distance $z = 557$ mm with respect to the specimen surface. Moreover, experimental uncertainties are included in the simulated images, assuming that:

- Noise is distributed following an Extreme Value distribution, where the Extreme value parameters are function of image grey levels;

- Out-of-plane motions are regulated by two angles $\vartheta = 0.0026$ rad, $\gamma = 0.0026$ rad and the distance $\delta_z = 0.058$ mm,while the in plane motions by $c_x = -2.50$ pixel and $c_y = -21.40$ pixel.

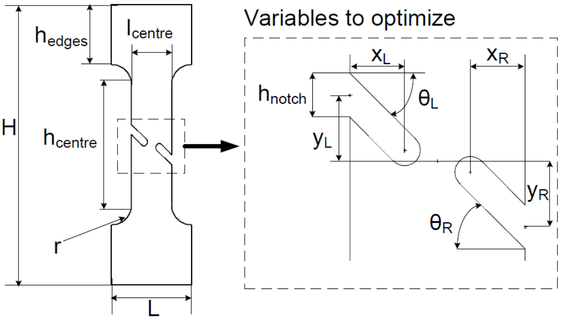

Figure 5.20: Specimen geometry and design variables. Dimensions are expressed in mm.

- Regarding lighting conditions, light spot illumination is introduced in order to simulate a not uniform floodlighting on specimen measurement ROI.

A complete discussion about these selected parameters for experimental uncertainties is given in [63].

Displacement and strain fields for VFM identification are measured using the DIC software MatchID, performing the analysis with a subset size of 23 pixels and step size of 3 pixels, involving the ZNSSD correlation algorithm. Hence, strain fields are derived setting a strain windows of 3 points, avoiding, in this way, strong filtering effects by the software.

According with [35, 85], the non-linear VFM (Chapter 4) cost function is minimized employing three different virtual fields:

$$\begin{cases} \delta u_1^{*(1)} = 0 \\ \delta u_2^{*(1)} = -\frac{y}{l} \end{cases} \quad \begin{cases} \delta u_1^{*(2)} = \frac{x}{w}\frac{(y-|l|)}{l} \\ \delta u_2^{*(2)} = 0 \end{cases} \quad \begin{cases} \delta u_1^{*(3)} = sin\left(\pi\frac{x}{w}\right)cos\left(\pi\frac{y}{h}\right) \\ \delta u_2^{*(3)} = sin\left(\pi\frac{x}{w}\right)cos\left(\pi\frac{y}{h}\right) \end{cases}, \tag{5.20}$$

where, considering the coordinate system placed with the origin at the centre of specimen, l is the semi-length of measurement area and w is the semi-width of middle section. In particular, further details on these virtual fields will be given in the following chapter.

Since the aim of this study is primarily to evaluate the simulation procedure response and its capability to distinguish an adequate geometry considering experimental error sources, analysis was executed using first directly the strain field resulting from FEA, then three different sets of numerical images: the former is composed by pure synthetic images, the second one involves noise in picture generation, the third set has all the other experimental uncertainties. Overall results are depicted in Figure 5.21, imposing $\bar{\varepsilon}_{lim} = 0.6$.

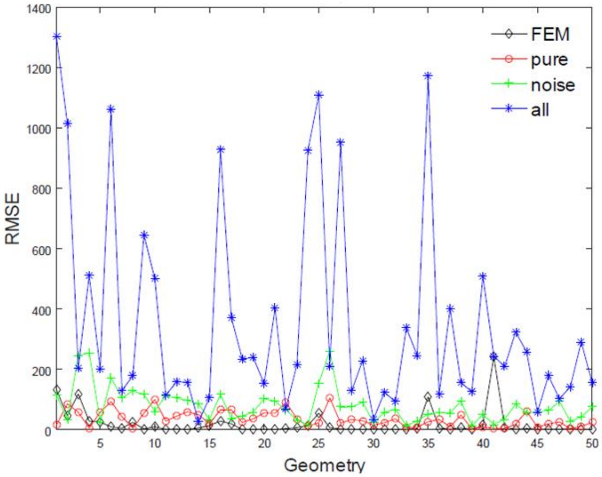

Figure 5.21: Resulting identification error for all 50 configurations with datasets coming from FEA and simulated experiments.

The analysis performed on FEM data shows results close to the ideal material behaviour, reaching, for the best geometry (configuration 39), a RMSE of 0.21%. When the DIC process is simulated, the RMSE increases as expected. Using pure images, the resulting best geometry is the same as the obtained one from FEA data, with an error increase around 2%. Concerning the second set of numerical images, adding noise deteriorates the pictures and, consequently, the identification. Nonetheless, the best geometry is still in agreement with the previous results, although its RMSE 12% higher. Including all the experimental error sources strongly affects the identification procedure. In fact, the best geometry changes compared to the previous cases; the RMSE value for configuration 39 arises un to 25%, while shows the lowest error is reached by configuration 14. The predicted $\sigma - \varepsilon$ curves from the best configurations are reported in Figure 5.22: the addition of all the reproduced experimental uncertainties deteriorates more the identification results compared to the pure numerical images and the synthetic images with noise.

5.4.2 Experimental validation

The validation of presented simulator capabilities in a real experiment has to face, first, two important observations: which geometries must be tested and

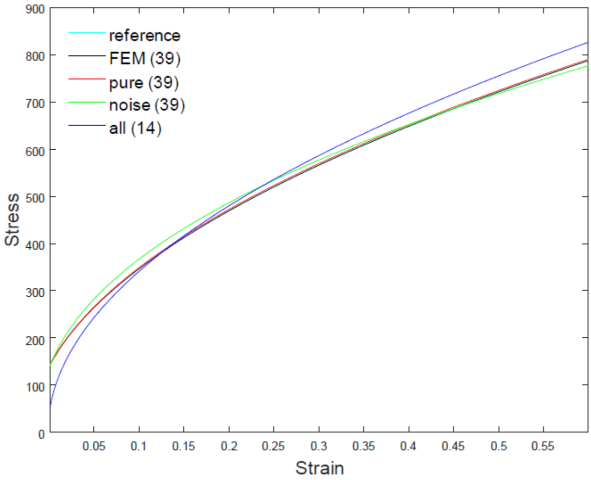

Figure 5.22: Comparison of predicted stress-strain curves from geometries having the best identification performances.

what kind of material to use. Answers to the former consideration can easily be found in the optimization results, taking into account specimen shapes that have respectively the best and the worse RMSE scores. The latter one, instead, responds to requirements of reaching an adequate plastic strain and also having an isotropic behaviour whose hardening can be described by Swift law (in other words, no Lüders bands phenomenon). So, three different configurations were selected:

- Geometry 6, which represents one of configurations with the worst RMSE score for all stages of reproduced uncertainties;
- Geometry 39, that is indicated by the simulator as the best configuration in case of FEA, pure numerical images and synthetic images with noise;
- Geometry 14, which provides the best identification results in case of numerical images generated with all the introduced experimental error sources.

In Figure 5.24 these specimens geometries are depicted in detail; for sake of clarity let's indicate them respectively with A, B, C. Further considerations can be taken observing equivalent plastic strain distribution from the FEA analysis reported in Figure 5.23: Geometry A provides a limited plastic strain area compared to the other two specimens, which reasonably explains the worst performance score. In fact, the considered experimental uncertainties relative to DIC measurements affect strains producing usually variations of $10^{-4} \sim 10^{-3}\ \varepsilon$.

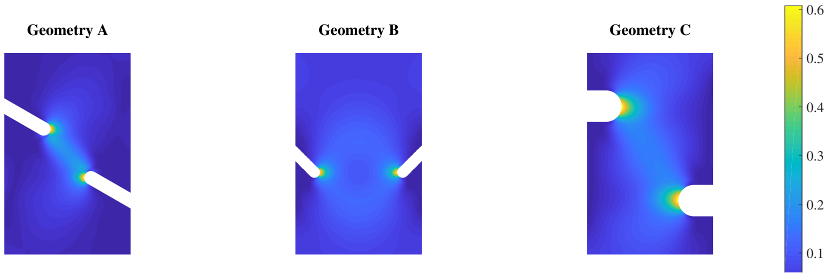

Figure 5.23: Equivalent plastic strain distribution for the three geometries.

Consequently, in large strain plasticity domain, they do not have crucial effects on identification. In other words, the larger the plasticized area (employed for non-linear VFM), the better the results achieved (Geometry C).

Since statistical relevance must be achieved to give a proper response, 9 specimens for each configuration were cut from a 2 mm thick sheet metal of X5CrNi18-10 (AISI304) austenitic stainless steel. This material, in fact, permits to reach elongation to break around 70%, characteristics that fits with the numerical simulator setting of equivalent plastic strain limit $\bar{\varepsilon}_p^{lim}$ imposed to 60%.

Albeit this version of simulator relies on isotropic plasticity, AISI304 sheets metal often exhibit mild anisotropy due to rolling process. Thus, a preliminary study was conducted on standard tensile specimens to have an insight on anisotropic behaviour of material impacts on validation. Samples at 0°, 45°, 90° with respect to RD were obtained from the same sheet metal and tested on tensile bench equipped with a stereo-DIC measurement system composed by two AVT Stingray F201-B cameras with 1624 × 1234 pixel 8-bit sensor, mounting 50 mm/f1.4 Cinegon C-mount lens. Displacement and strain measurement were processed with the DIC correlation software MatchID Stereo, using a subset of 35 pixels and 7 pixels of step-size, ZNSSD criterion, affine shape function and bicubic spline interpolation. Acquired experimental data were processed to calculate Lankford coefficients R [19], also, identification of Swift law parameters was realised by non-linear VFM. In fact, the necking phenomenon occurs when only the 40% of plastic deformation is reached, so, employing the VFM allows to include post-necking strain field data, including plastic strains up to 60%. All results are summarised in Table 5.5.

The calculation of R-value is performed considering the in-in plane stress in the horizontal direction ε_w and the through-the-thickness strain ε_t, as reported in Figure 5.25b for a maximum strain in the loading direction of 40%. Material does not show a strong normal anisotropy but only a slight value of planar anisotropy, confirming its employment for the proposed validation.

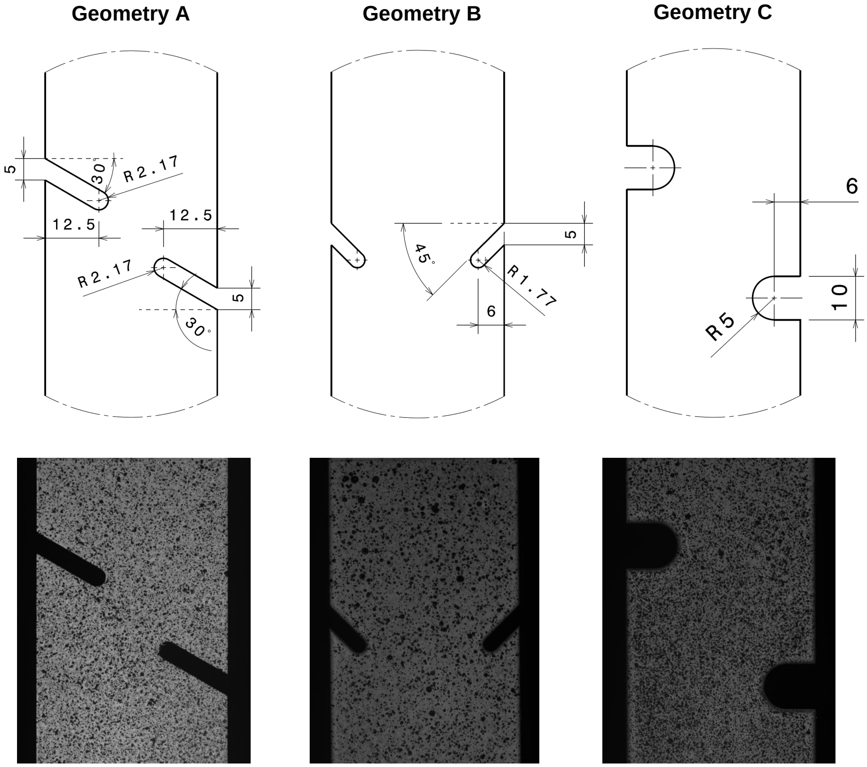
Geometry A
Geometry B
Geometry C
5
30
R2.17
12.5
12.5
R2.17
5
30°
45°
5
R1.77
6
6
10
R5

Figure 5.24: Details of notched specimens used for the experimental validation. Geometries A, B, C, correspond to configuration 6, 39, 14 respectively; dimensions are in mm. Also, examples of samples in real test are reported below.

Material Orientation	σ_Y /MPa ($\varepsilon = 0.2\%$)	R
0°	287	0.9460
45°	295.1	1.0639
90°	300.2	0.9187
Normal Anisotropy		$\bar{R} = 0.9981$
Planar Anisotropy		$\delta R = -0.1315$
Swift Law parameters at 0°:		
K /MPa	ε_0	n
1788	0.095	0.78

Table 5.5: Lankford parameters evaluation and Swift hardening law characterization for AISI304.

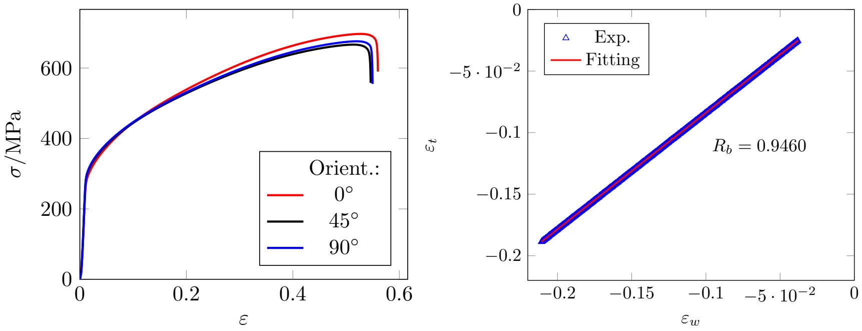

(a) Engineering σ-ε curves from standard tensile test.

(b) R-value at 0° material orientation.

Figure 5.25: Results from uniaxial tensile test campaign on standard uniaxial specimen. Figure (b) reports the R-value calculation for the 0° direction.

The selected outcoming geometries of notched specimens were tested employing an experimental arrangement congruous to the hypothesised one in the optimization process. So, two AVT CMOS Pixelink B371F cameras with 1280×1024 resolution and 8-bit sensor with 50 mm C-mount lens were used for stereo-DIC measurement; stereo vision acquisition is, indeed, a different condition from the simulated 2D set-up, however, represents a more accurate instrument for this kind of validation. Also here, images correlation was executed by MatchID Stereo software, imposing a subset size of 23 pixels and 3 pixels of step size as in the simulating procedure, using a ZNSSD to deal with changing illumination conditions, affine shape function and bicubic spline interpolation function.

First, evaluation of noise and displacement resolution was performed on static images for all 27 specimens. Noise as standard deviation of pixels grey levels values reached a maximum score of 0.47%, while the maximum resolution displacement measured was 0.00068 mm for horizontal direction and 0.00066 mm for vertical one.

Hence, the identification procedure via non-linear VFM was executed following the same path described in simulated experiment protocol. Also here the retrieved characterization results are reported in terms of RMSE error according to Eq. 5.19, where reference stress-strain curve is calculated using the parameters obtained from uniaxial dogbone.

As displayed in Figure 5.26, RMSE score for each geometry depends on the maximum equivalent plastic strain achieved. For this reason, three different limits of $\bar{\varepsilon}_p$ were considered for the analysis, based on the correspondent value where necking regime takes place. In fact, from the experimental activity on standard uniaxial tensile specimen, the material exhibits necking initialization at approximately $\bar{\varepsilon}_p = 40\%$, while the post-necking data allow to extend the identification to 60% of equivalent plastic strain; furthermore, the special conformation of introduced notched specimen is able to increase equivalent plastic strain, reaching nearly the 100%. It is worth noting that reference hardening law parameters were not obtained from strain data up to the higher limit of $\bar{\varepsilon}_p = 100\%$, so the corresponding missing values of stress-strain curve where extrapolated mathematically.

Observing the RMSE results at the lower strain limit (Figure 5.26a), the geometries do not display significant differences; when $\bar{\varepsilon}_p$ increases (Figure 5.26b and Figure 5.26c), Geometry A presents higher values of errors, confirming the response of numerical simulator. On the other hand, the designated best configuration (Geometry C) shows to have almost the same trend at the three different levels of maximum equivalent plastic strain. An interesting perception of simulator outcomes is given plotting all identified hardening curves for each set of specimens. At least there is one specimen for each shape almost reaching the reference trend; however, Geometry A provides higher variance of results (Figure 5.26d) compared to Geometry B (Figure 5.26e) and Geometry C (Figure 5.26f), that, instead, appears to be the most robust one producing the most repeatable identification results. These data can be also summarised in statistical terms computing the mean and standard deviation of the displayed stress-strain curves, as reported in Figure 5.27. Comparing the average hardening curves there is not a perfect matching with the reference one, however, Geometry C seems to have roughly its same trend.

Thus, the described experimental activity validates the results provided from the numerical simulator, giving, also, an important insight on the fundamental role played by experimental uncertainties on reliability of identification outcomes. In fact, when a full-field measurement is employed, geometrical features have not only a determinant impact on the strain field and, consequently, on gathered material information, but also can affect and reduce impacts of error sources.

Some remarks must be pointed out. According to numerical results, specimens with better performance are characterized by a diffused plastic strain area, while localized strain concentrations only in proximity of notches produce worse identification, according also to [86, 83]. Nevertheless, even these optimal geometries do not produce a ample strain field compared to common double notched specimen in Figure 3.5. The DOI previously explained, indeed, does not help to find a sort of absolute optimal configuration, but in this case represents a reasonable strategy to have a proper control on simulator results. Therefore, the presented simulating protocol can be improved using more advanced optimization methods as, for instance, Simplex Algorithm or Genetic Algorithms. In future, moreover, this approach can be extended to other

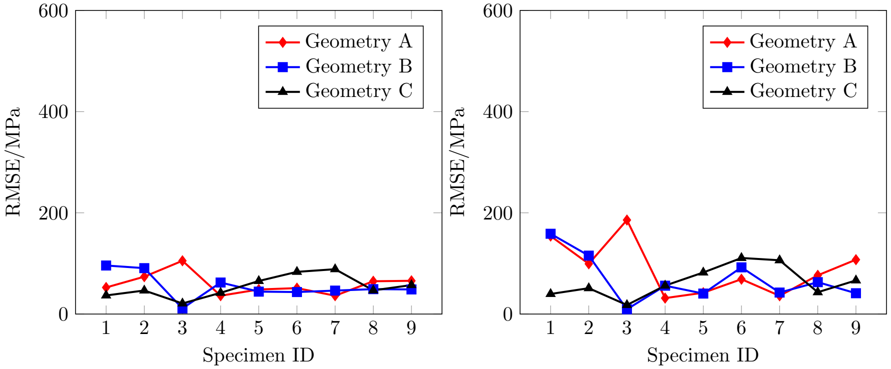

(a) RMSE at $\bar{\varepsilon}_p = 40\%$.

(b) RMSE at $\bar{\varepsilon}_p = 60\%$.

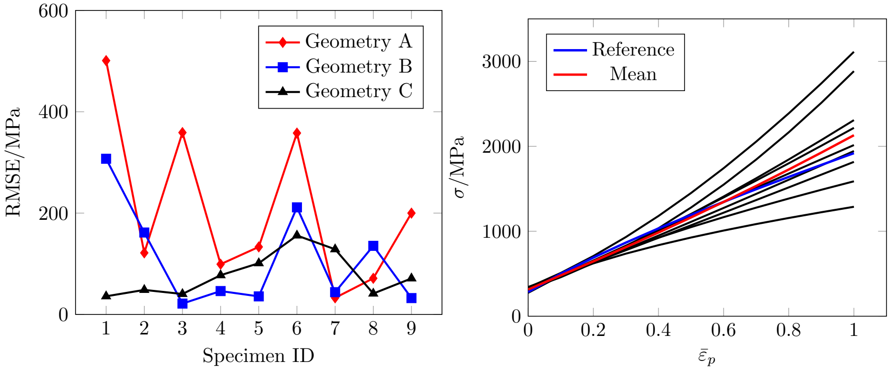

(c) RMSE at $\bar{\varepsilon}_p = 100\%$.

(d) σ-ε curves from Geom.A.

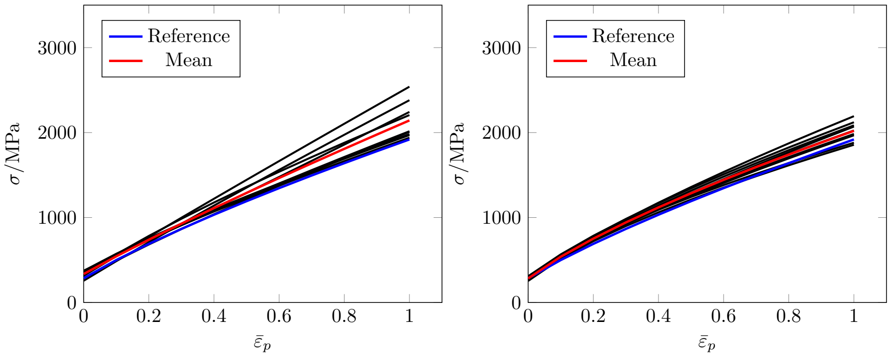

(e) σ-ε curves from Geom.B.

(f) σ-ε curves from Geom.C.

Figure 5.26: Overview of experimental activity results. RMSE scores for all specimens are reported at different equivalent plastic strain thresholds. Also, all hardening curves calculated from identified parameters are displayed for the three geometries, highlighting in red the mean value curve and in blue the reference one.

specimen' shapes and to more complex constitutive models, as in case of anisotropic plasticity.

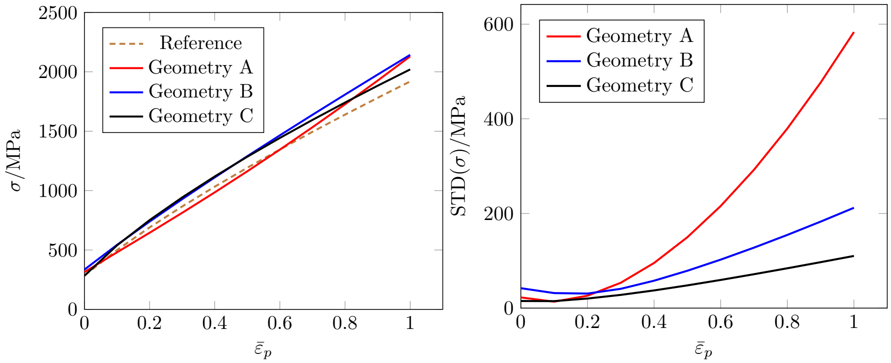

(a) Average σ-ε curve.

(b) Standard deviation.

Figure 5.27: Statistical comparison in terms of average stress-strain curve and standard deviation trends for the three geometries considered.

Chapter 6

Identification of anisotropic plasticity models: the YLD2000-2D

6.1 Introduction

In this Chapter the whole theoretical framework described previously is connected with the aim to characterize an advanced consitutive model for anisotropic plasticity: the YLD2000-2D. The Direct Method is employed to reconstruct the stress state required for the internal Virtual Work calculation in the non-linear VFM, in order to verify the accuracy. The results are compared with the standard calibration procedure involving material experimental data from uniaxial and equi-biaxial stress states.

As reported in Section 2.3.2, the YLD2000-2D [20, 22] yield criterion is founded on the description of anisotropic behaviour through the application of two linear transformations on the Cauchy stress tensor. In particular, these linear transformations are described by the two matrices $\mathbf{L}'$ and $\mathbf{L}''$, which are function of 8 linearly independent parameters α_i.

The aforementioned material model is valid under the plane stress assumption that is usually acceptable in sheet metal forming problems. Performing uniaxial tension test along the RD and TD, and balanced biaxial stress state provides three flow stresses σ_0, σ_{90}, σ_B and three R-values R_0, R_{90}, R_B, allowing to calibrate parameters from α_1 to α_6. Moreover, the flow stress and R-value obtained from uniaxial tensile test at 45° with respect to TD supply the remaining coefficients α_7 and α_8. Details about mathematical procedure for their calculation are reported in the Appendix of [20].

Identification via VFM, instead, is realised by opportunely shaped notched specimens that produces an heterogeneous stress state under the plane stress assumption [39, 47]. The heterogeneous strain field can be measured with full-field techniques. This geometry is particularly convenient because permits to have a large area of the specimen under plastic deformation. In other approaches, like the Σ-shaped specimen proposed by [87], the strain localizes around fillets leaving most of the measurement zone under low and sometimes elastic deformations. In Figure 6.1 its geometrical dimensions are displayed.

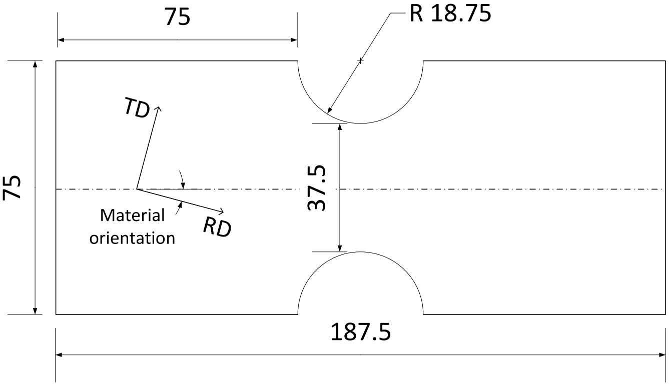

Figure 6.1: Specimen geometry for VFM identification (units: mm).

The application of non-linear VFM needs the definition of proper Virtual Fields (VF) respecting the boundary conditions imposed by the problem (i.e. kinematically admissible Virtual Fields). As already mentioned in Section 4.3, the optimal choice of VFs for elasto-plasticity identification is still an open question. Very recently, an automatic procedure to select virtual fields was introduced in [50], based on the stress sensitivity to each constitutive parameter. However, in this research, manually defined VFs are used in the VFM cost function. This kind of VFs are also called stiffness-based since they depend only from stiffness matrix, and in literature several application of this approach can be found in elasto-plastic problems for both monotonic loads [35, 26, 85] and cyclic plasticity [88, 89] for example.

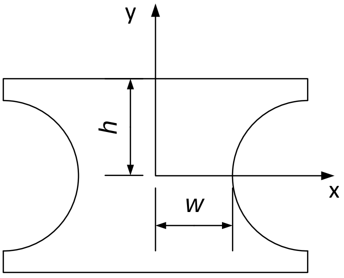

Figure 6.2: Schematic of the reference frame used in the VF definition.

Placing the x-y reference frame in the AOI submitted to VFM procedure as depicted in Figure 6.2 and defining with h and w respectively its semi-height and semi-width, three VFs are introduced. The first used Virtual Field is reported in the following equation:

$$\begin{cases} \delta u_x^{*(1)} = 0 \\ \delta u_y^{*(1)} = \dfrac{y}{h} \end{cases} \qquad \delta \boldsymbol{F}^{*(1)} = \begin{bmatrix} 0 & 0 \\ 0 & \dfrac{1}{h} \end{bmatrix} \tag{6.1}$$

As introduced previously in Chapter 5, this Virtual Field makes that external Virtual Work proportional to the measured loading force $W_e^* = 2F$, and it affects only the stress component corresponding to the vertical direction. The other two Virtual Fields are respectively:

$$\begin{cases} \delta u_x^{*(2)} = \dfrac{x}{w}\dfrac{|y|-h}{h} \\ \delta u_y^{*(2)} = 0 \end{cases} \qquad \delta \boldsymbol{F}^{*(2)} = \begin{bmatrix} \dfrac{|y|-h}{wh} & \mathrm{sgn}(y)\dfrac{x}{wh} \\ 0 & 0 \end{bmatrix} \tag{6.2}$$

and

$$\begin{aligned} &\begin{cases} \delta u_x^{*(3)} = \dfrac{1}{\pi} sin\left(\pi\dfrac{x}{w}\right) cos\left(\pi\dfrac{y}{2h}\right) \\ \delta u_y^{*(3)} = \dfrac{1}{\pi} sin\left(\pi\dfrac{x}{w}\right) cos\left(\pi\dfrac{y}{2h}\right) \end{cases} \\ &\delta \boldsymbol{F}^{*(3)} = \begin{bmatrix} \dfrac{1}{w} cos\left(\pi\dfrac{x}{w}\right) cos\left(\pi\dfrac{y}{2h}\right) & -\dfrac{1}{2h} sin\left(\pi\dfrac{x}{w}\right) sin\left(\pi\dfrac{y}{2h}\right) \\ \dfrac{1}{w} cos\left(\pi\dfrac{x}{w}\right) cos\left(\pi\dfrac{y}{2h}\right) & -\dfrac{1}{2h} sin\left(\pi\dfrac{x}{w}\right) sin\left(\pi\dfrac{y}{2h}\right) \end{bmatrix} \end{aligned} \tag{6.3}$$

Observing the second VF, it takes into account the horizontal stress component, producing a displacement field $\delta u_x^{*(2)}$. It has a trend similar to the one observed from FEA simulations or experiments on double notched specimens. At the upper ($y = h$) and lower ($y = -h$) bounding frontiers it can be easily verified that:

$$\delta u_x^{*(2)} = \delta u_y^{*(2)} = \delta u_x^{*(3)} = \delta u_y^{*(3)} = 0\,, \tag{6.4}$$

hence the external Virtual Work is null.

Basically, the first Virtual Field takes into account the anisotropy of the yield stress at different directions, while the second and third Virtual Fields is more sensitive to the R-value anisotropy.

The investigation is carried out on two different *Advanced High-Strength Steels* (AHSS), largely employed in automotive industrial applications, the BH-340 and TRIP-780. In the following the two identification approaches adopted are described, discussing and comparing their results. Then, final considerations are reported in the Conclusions Chapter.

6.2 Calibration of BH-340 steel

Bake Hardening (BH) [90] indicates a category of ferritic steels submitted to controlled ageing process which regulates the presence of carbon and/or nitrogen in solid solution. This gives to the material a strengthening effect achieving also a good drawability. In the automotive industry is usually employed in visible (for instance: door, hood, tailgate, roof [91]) and structural (i.e. cross member, underbody, reinforcement, lining) parts.

6.2.1 Standard calibration procedure

The used uniaxial tensile machine is depicted in Figure 6.3. Standard uniaxial flats specimens at 7 different directions with respect to RD were obtained from the same BH-340 sheet metal having thickness of 0.7 mm. Displacement and strain fields on the specimen surface are retrieved using a stereo-DIC set-up composed by two 2448 × 2048 CCD cameras, synchronized with the 500 kN loading cell to couple each frame with measured force. VIC-3D software (`www.correlatedsolutions.com`) is employed for the correlation analysis, setting a subset size of 21 pixels and a step size of 3 pixels, while strain derivation is calculated imposing a filtersize of 15 points. More details about the DIC settings are reported in Table 6.2

Results of this experimental activity are reported in Figure 6.4 in terms of engineering and true $\sigma - \varepsilon$ curves, and in Table 6.1 for the corresponding Lankford coefficient R.

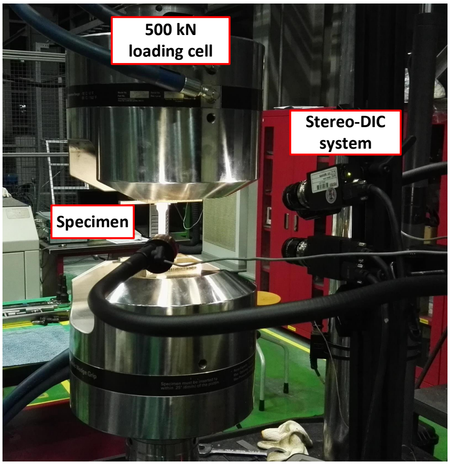

Figure 6.3: Uniaxial test experimental setup.

Material Orientation	σ_Y MPa	R
0°	225	1.52
15°	223	1.3
30°	227	1
45°	245	0.9
60°	241	1.08
75°	238	1.48
90°	226	1.67
Swift Law parameters (0°):		
K /MPa	ε_0	n
618.5	0.0022	0.204

Table 6.1: Summary of uniaxial test results for BH-340.

Observing the obtained R-values, material exhibits an isotropic behaviour at 30° and 60°, while shows its maximum anisotropy along the RD and TD orientations. Concerning the stress-strain curves (Figure 6.4b), RD and TD have almost similar values, otherwise test at 45° has a slightly higher hardening curve (∼ 20 MPa).

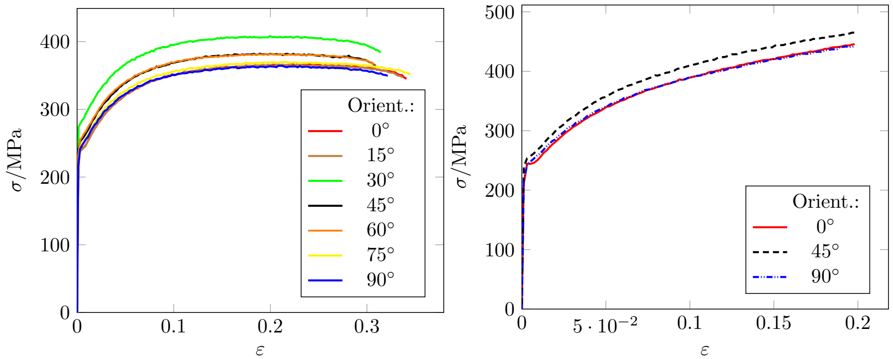

(a) Engineering curve.

(b) True curve.

Figure 6.4: BH-340 uniaxial tensile test results on standard specimens obtained at seven different directions with respect to RD. For the sake of clarity, the True σ-ε curves are reported only for the three orientations that are directly involved in the identification.

Specimen	Uniaxial	Blank Bulge
DIC technique	3D correlation	3D correlation
Pre-filtering	Gaussian-Kernel 5	Gaussian-Kernel 5
Subset (pixel)	21	43
Stepsize (pixel)	3	7
Correlation criterion	ZNSSD	ZNSSD
Shape function	Affine	Affine
Interpolation function	Bicubic spline	Bicubic spline
Strain computation	Gradient	Gradient
mm to pixel conversion	1 mm=0.0543 pixel	1 mm=0.1217 pixel
Performance analysis		
Spatial resolution	1.1403 mm (21 pixel)	5.2331 mm (43 pixel)
Resolution (pixel)	0.0193	0.0479

Table 6.2: Settings used for the DIC measurements on BH-340 uniaxial and bulge tests, and performance analysis.

The remaining information required to calibrate the yield function model regards the material behaviour at equi-biaxial stress state condition, which, in this case, are obtained through the hydraulic bulge test. When the bulge is formed through the application of a pressure on the blank sheet, a membrane stress state of a thin-walled spherical vessel can be assumed in proximity of the dome apex, permitting the calculation of stress-strain curve in the condition of equi-biaxial stress state [92, 93].

In particular, the achievement of biaxial stress-strain curve requires the measurement of three quantities: the forming pressure of fluid, the bulge curvature, and the through-thickness strain. Full-field measurement with stereo-DIC allows to obtain the latter two inputs, since it returns both shape and displacement fields; the in-plane strains can be derived from displacements fields, and, then, the through-thickness strain component can be obtained thanks to the hypothesis of volume conservation, valid during plastic deformation. The used, stereo-DIC system is illustrated in Figure 6.5. The DIC settings are: a subset of 35 pixels on a step size of 5 pixels and strain filtering of 15 in VIC-3D. Further DIC measurement settings are listed in Table 6.2 The results of bulge test experimental campaign are reported in Figure 6.6 and Figure 6.7, according to calculations contained in the ISO 16808:2014 standard [94].

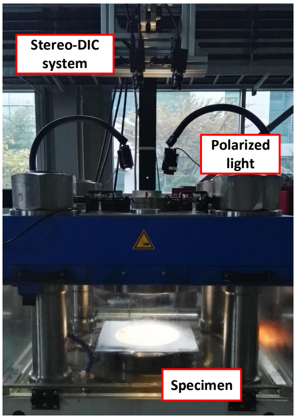

Figure 6.5: Bulge test experimental setup.

Max. Drawing Force:	1000 kN
Max. Drawing velocity:	220 mm/min.
Blank Holding Force:	1000 kN
Blank specifications:	
Length and height:	300 mm
Bulge diameter:	200 mm

Table 6.3: Bulge test equipment specifications.

DIC correlation also furnishes the input data for the biaxial R-value with the adequate strain measurement accuracy. Considering a circular area having radius $r = 10$ mm centred in the dome apex, plastic strain along the RD and TD can be evaluated with the following formula:

$$\varepsilon_p^{dir} = \varepsilon^{dir} - \frac{1-\nu}{E}\sigma_B \tag{6.5}$$

where σ_B represents the equi-biaxial stress, E and ν the elastic constants. Biaxial R-value R_B is, thus, retrieved by means of linear fitting as depicted in Figure 6.7b.

The experimental data coming from uniaxial tensile tests at three orientations (0°, 45°, 90° with respect to RD) and equi-biaxial stress-strain curve coming from the bulge test need one last processing step before they can be used for

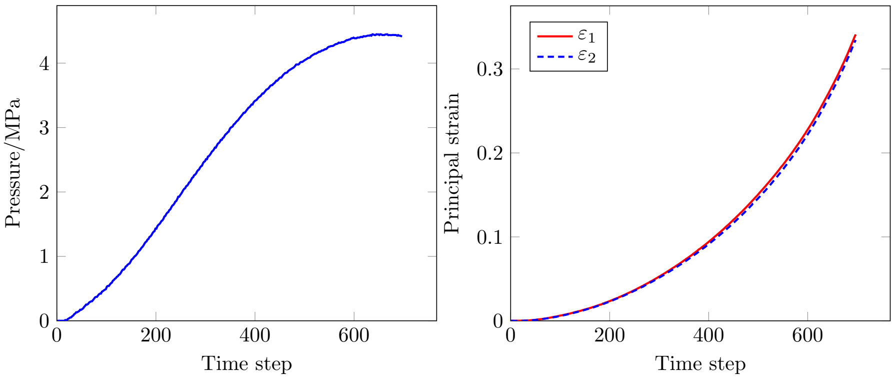

(a) Pressure.

(b) Hencky principal strains.

Figure 6.6: Hydraulic bulge test pressure until fracture and principal strains measured on the specimen surface with DIC for BH-340.

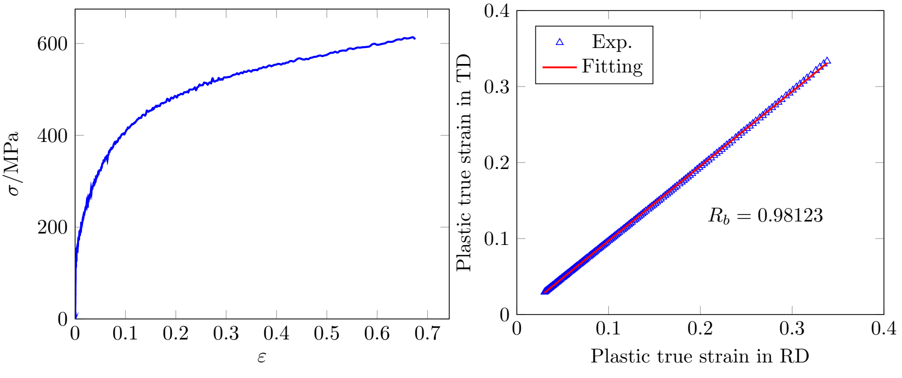

(a) Equi-biaxial stress-strein curve.

(b) R-value R_B .

Figure 6.7: True stress and strain curve for equi-biaxial stress state for BH-340. Besides, plastic strains along the RD and TD are reported for the calculation of biaxial R-value.

the identification of YLD2000-2D. Although stresses and r-values at yielding point permit to calibrate the model, in fact, they cannot give a proper insight on material behaviour at large deformation. Thus, according to the approach of Barlat in [95, 96, 20, 57], flow stresses corresponding to a certain amount of Plastic Work must to be selected. The yield surface has to be expressed with respect to the strain hardening rate from one of the tests required for the calibration. Practically, it is convenient to employ the biaxial stress-strain curve, since, in the case of the bulge test, this reaches larger deformations compared with the uniaxial tests.

The flow stress trend can be displayed as function of Pastic Work W_p, as illustrated in Figure 6.8. After Plastic Work $W_p = 59$ kJ, the three uniaxial tests assume a constant trend, i.e. the yield function is stable. This consideration is better explained reporting the flow stresses in the plane of principal stresses (i.e. π-plane), normalised with respect to σ_B. Increasing the amount of Plastic Work, indeed, the yield function will tend to cover different points, until the relative yielding surface assumes a stable shape.

Thereby, the value of Plastic Work, considered for yield function calibration, is $W_p = 59$ kJ. The resulting flow stresses relative to all tests performed are presented in Table 6.4.

Dir.	0°	15°	30°	45°	60°	75°	90°	*Biax.*
$\frac{\sigma}{\sigma_B}$	0.9219	0.9180	0.9508	0.9558	0.9567	0.9288	0.9154	1
R	1.52	1.30	1.00	0.89	1.06	1.48	1.67	0.98

Table 6.4: Input data for YLD2000-2D calibration on BH-340 steel.

Finally, results of YLD2000-2D calibration for BH-340 steel are depicted in Figure 6.10, reporting the eight α_i coefficients and the predicted yield surface. Since ferritic steels are characterized by a BCC crystal structure, the a exponent is commonly assumed as 6 for Bake Hardening steel [21].

6.2.2 VFM identification procedure

Notched specimens with the same geometry specifications illustrated in Figure 6.1 were cut from the same blank sheet of BH-340 at three different material orientations: 0°, 45° and 90° with respect to RD. In [26] there is reported a numerical and experimental study showing that the use of such specimens obtained at these directions can cover a portion of the yield surface which excludes the pure shear and balanced-biaxial stress state.

The full-field measurement is performed employing the same stereo-DIC system described previously. Image correlation is achieved via VIC-3D software, setting a subset window of 32 pixels and a step size of 3 pixels between two

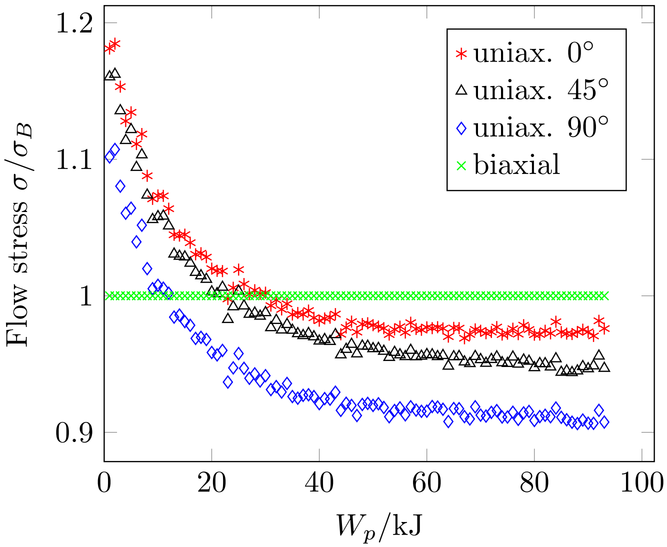

Figure 6.8: Flow stress normalised by the equi-biaxial stress σ_B as function of Plastic Work W_p for BH-340.

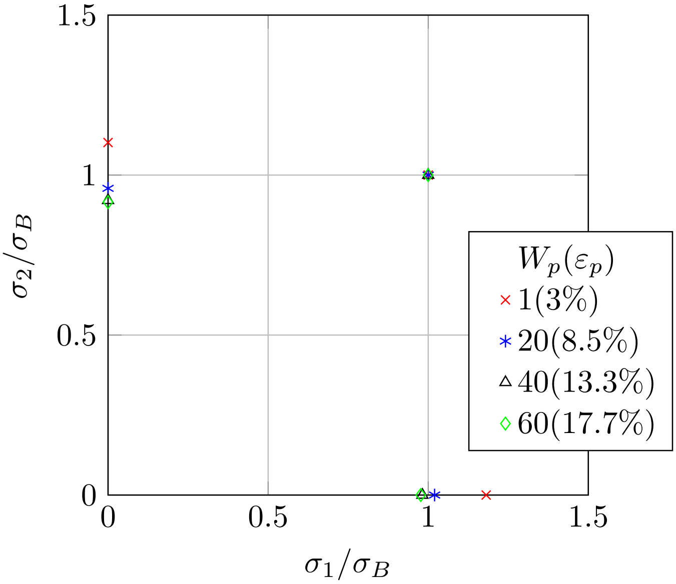

Figure 6.9: BH-340 plot on the π-plane of flow stresses calculated at different Plastic Work. Corresponding plastic strain from uniaxial tensile test at 0° is reported in parenthesis.

YLD2000-2D coefficients:	
α_1	1.0780
α_2	1.1629
α_3	0.9646
α_4	1.0212
α_5	1.0292
α_6	0.9346
α_7	1.0234
α_8	1.1336
a	6

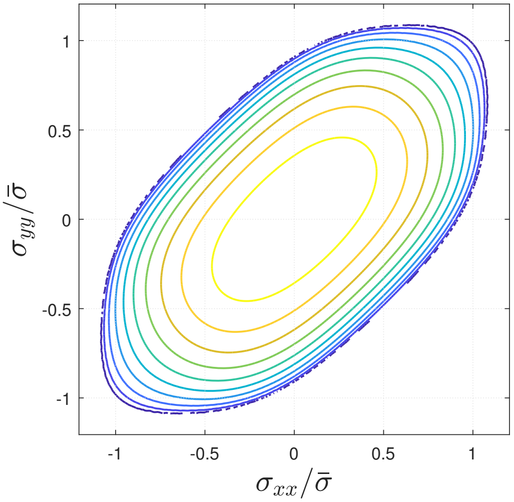

Figure 6.10: Anisotropy coefficients and predicted tricomponent yield surface for BH-340 steel.

measurement points. In particular, incremental correlation strategy was adopted, which means that each image is correlated with the previous one and the measured incremental displacement is added to the one from previous step. Further metrology specifications on this experimental campaign are summarised in Table 6.5.

Figure 6.11 illustrates an example of strain fields obtained from the experiments, used later for the VFM identification. The VFM was restricted to this smaller zone for two reasons: first, it remains planar up to large strains whereas the external parts of the specimen tend to wrinkle when load increases; second, the plastic flow localizes within this zone reaching the highest deformations, while the external parts mainly remains in the elastic regime. Thereby, 158×389 measurement points are considered in the identification procedure for each time step.

Accuracy of measured displacement field plays a crucial role in the VFM identification, leading the accuracy of retrieved material parameters. In Section 5.3, for instance, there are described the effects of boundary area in the identification results, but also noisy strain data can represent a considerable issue, as reported in [97] in elasticity or [35, 26] for anisotropic plasticity. For this reason, spatial smoothing is applied by means of least-square smoothing based on convolution method proposed by Gorry [36]. In such case, 9 measurement points are used to perform convolution, and Figure 6.12 depicts an example of the same strain field before and after smoothing.

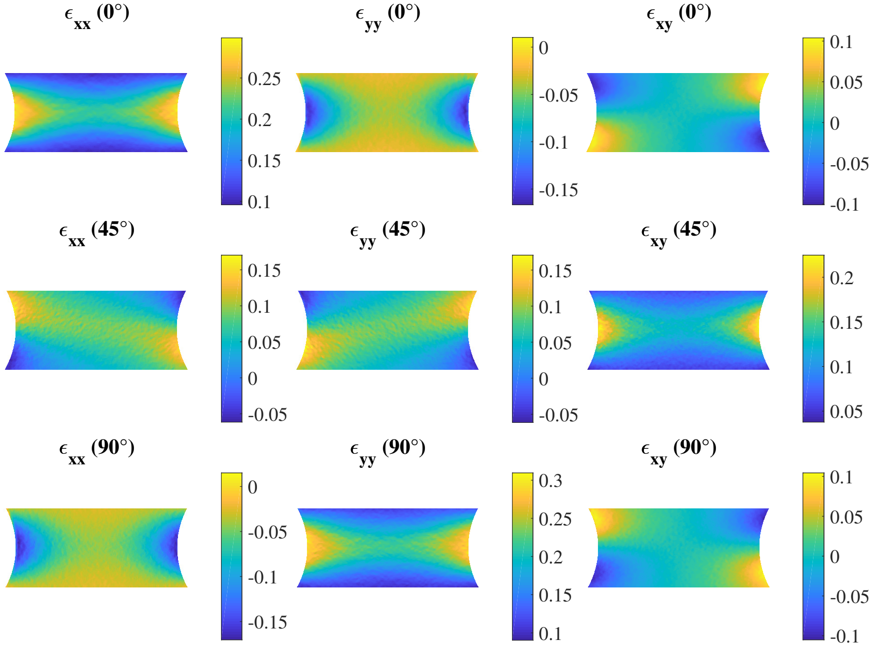

Figure 6.11: Example of measured strain fields on BH-340 specimens' surfaces at different material orientations.

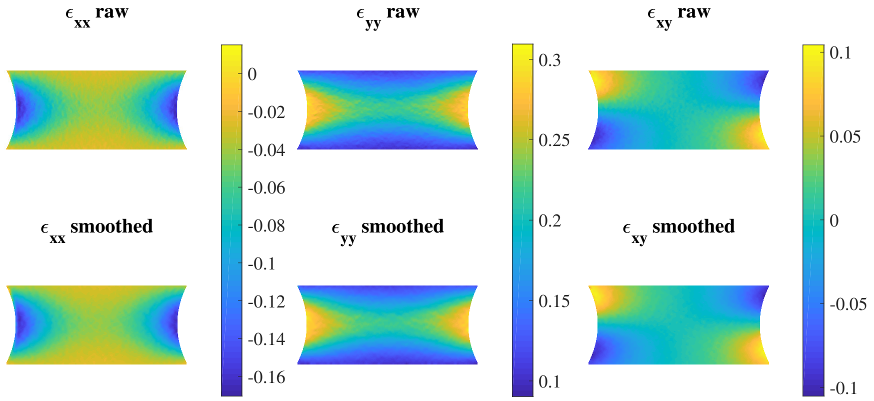

Figure 6.12: Effects of smoothing application on strain fields for BH-340 specimen oriented at 90° with respect to RD. The reference frame is local.

DIC technique	3D correlation
Pre-filtering	Gaussian-Kernel 5
Subset (pixel)	31
Stepsize (pixel)	3
Correlation criterion	ZNSSD
Shape function	Affine
Interpolation function	Bicubic spline
Strain computation	Gradient
Performance analysis	
Spatial resolution	1.1142 mm (31 pixel)
Resolution (pixel)	0.0607

Table 6.5: Settings used for the DIC measurements and performance analysis on BH-340 notched specimens.

Non-linear VFM is applied to retrieve only the YLD2000-2D coefficients α_i, while Swift hardening law parameters are assumed equal to the reference ones from uniaxial test at 0°. Furthermore, such yielding function requires the definition of the exponent a. Since this exponent is strictly related to the material crystal structure, here it is excluded from the inverse identification and imposed equal to $a = 6$.

The introduced two strain data sets are submitted to identification, considering 30 time steps. Minimization of the cost function Ψ is performed using MATLAB® Optitool function *fmincon*. The whole identification process takes an average time of 5h 40min employing parallelization on 6 cores. Rossi et al. in [26] demonstrate that minimization initial guess does not have significantly impact on identification outcomes, so, initially all material parameters were setted equal to 1. The overall results of identification are illustrated in Table 6.6, where cost function score Ψ obtained at the end of minimization represents a quantitative indicator of identification quality [98].

6.2.3 Comparison of identification results

Comparison of calibration results for the BH-340 steel can be outlined drawing predicted yield surfaces whose coefficients are achieved via standard and VFM procedures. Considering the plane of stresses σ_{xx} and σ_{yy} in Figure 6.13, the corresponding yield surfaces are reported in the case of shear component $\sigma_{xy} = 0$. It should be noted that material parameters are retrieved from different reference flow stresses. In fact, the normalised flow stress with respect to equi-biaxial stress state are involved for the standard characterization, while VFM identification employs the flow stress data coming from the Swift hardening law calibrated on the 0° oriented specimen; therefore, since comparison between

	Raw data	Smooth. data
α_1	1.0602	1.0577
α_2	0.9435	0.9588
α_3	0.8281	0.8301
α_4	0.8920	0.9069
α_5	0.9144	0.9220
α_6	0.8488	0.8582
α_7	0.8985	0.9176
α_8	0.9831	1.0159
a	6	
	Cost Function score:	
Ψ	654.95	532.43

Table 6.6: Identified YLD2000-2D coefficients with non-linear VFM for BH-340.

yield surfaces is possible only if they refer to the same hardening curve, yield surfaces are calculated considering the 90° direction as reference for each sets of identified coefficients α_i.

Parameters obtained from VFM on both raw and smoothed strain data do not produces significant differences. Nevertheless, they are not capable cover perfectly the equi-biaxial stress state point and uniaxial stress at 0° predicted by the reference yield surface from standard procedure.

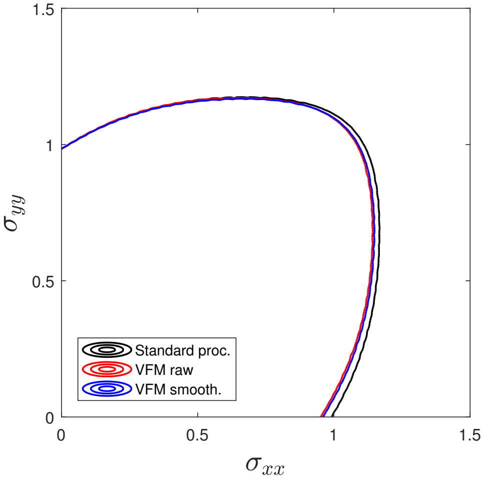

Figure 6.13: Comparison of predicted yield surfaces obtained employing the standard procedure, the VFM on raw and spatially smoothed strain data for BH-340. The yield surfaces are normalised by the TD.

Another effective way to assess the goodness of identification results can be made evaluating the predicted flow stresses and R-value at different material orientations (Figure 6.14).

YLD2000-2D calibrated with the standard procedure offers the same tensile properties at 0°, 45° and 90°. Otherwise, coefficients derived from VFM are not able to predict flow stresses at 0°, showing a maximum gap of 0.04 points. Smoothing strain data decreases this bias for angle parallel to RD, although the difference at 45° increases and the model with these material parameters is still not capable of perfectly reproducing the experimental trend. However the differences are quite small, with a maximum bias of 4% for the VFM parameters from raw strain data at 0°.

Also observing the R-value trend there is a perfect accordance between the predicted results by YLD2000-2D characterized from uniaxial and biaxial experimental data; on the other hand, VFM derived parameters are capable of capturing the experimental R-value trend, showing a difference of 0.12 points at 0° and 0.19 at 90°, which reduces to 0.06 using smoothed strain fields data.

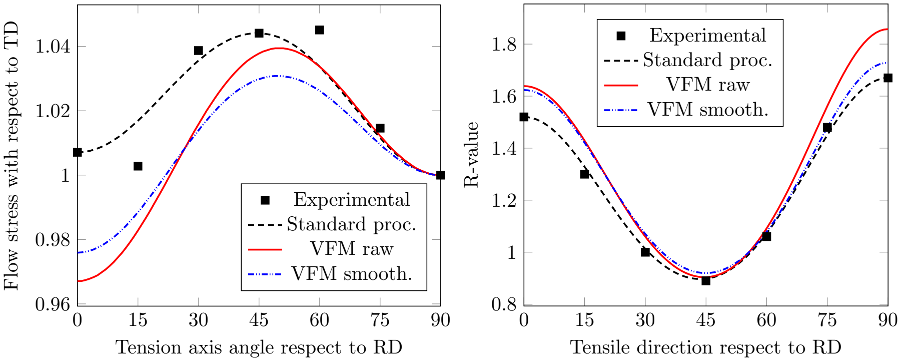

(a) (b)

Figure 6.14: Comparison of anistropy of uniaxial yield stress with respect to the TD flow stress (a) and of R-value (b) for BH-340, measured experimentally and predicted with YLD2000-2D. Characterization is achieved using the standard procedure and also VFM on the two strain data sets. All the values are normalised by the TD

Another comparison can be performed looking at the predicted flow stress from the equi-biaxial stress state. As reported in Table 6.7, the coefficients identified by means of VFM technique are able to predict the equi-biaxial flow stress with a reasonably difference of 1.3% in case of raw strain data and 0.9% for smoothed data. This represents an interesting results, since the adopted notched specimens do not feed the VFM with direct data from the balanced biaxial stress state.

Some further considerations can be pointed out. As already discussed in

Standard	VFM raw	VFM smooth.
1.0924	1.0783	1.0820

Table 6.7: Comparison of predicted flow stress at the equi-biaxial stress state for BH-340.

Chapter 5, the identification of material parameters relies on the accuracy of measurement. So, looking also at the error function scores listed in Table 6.6, DIC measurement can be improved, especially in proximity of notches' edges. Moreover, the VFM uses an heterogeneous strain (and consequently stress) field to identify the material parameters, while the standard calibration basically fits the exact data from four different test. So, such observed differences may be ascribed to this. Reasonably, sensitivity based virtual fields can give a better insight on the influence of heterogeneous stress field in the identification, and may help to improve results.

6.3 Calibration of TRIP-780 steel

The second material employed for this experimental investigation is TRIP-780. Microstructure of Transformation-Induced Plasticity steels is characterised by retained austenite (min. 5%) embedded in a ferrite primary matrix. In addition, hard phases of bainite and martensite are present in varying percentage of volume. The dispersion of hard second phase in ferrite contributes to have an high work hardening during deformation, however, the peculiarity of TRIP is represented by progressive transformation of retained austenite in martensite at higher deformation, producing a further work hardening effect. Therefore, TRIP offers a considerable combination of strength and ductility, becoming a diffused material for structural and safety parts having complex shape. In automotive industry, typical examples of application are cross members, longitudinal beams, B-pillar and bumper reinforcements, sills.

6.3.1 Standard calibration procedure

Characterization of YLD2000-2D yield function for TRIP-780 follows the procedural path described in Section 6.2.1. Uniaxial tensile test campaign was conducted using also the same experimental arrangements previously specified. Therefore, flat standard tensile specimens were obtained at 7 different material orientations with respect to RD from the same sheet metal having 1.4 mm thickness. Displacement and strain measurement is achieved, in this case, with the correlation software *MatchID*, whose settings are reported in Table 6.11.

Observing outcoming stress-strain curves (Figure 6.15), TRIP-780 exhibits

Specimen	Uniaxial	Blank Bulge
DIC technique	3D correlation	3D correlation
Pre-filtering	Gaussian-Kernel 5	Gaussian-Kernel 5
Subset (pixel)	25	43
Stepsize (pixel)	5	7
Correlation criterion	ZNSSD	ZNSSD
Shape function	Affine	Affine
Interpolation function	Bicubic spline	Bicubic spline
Strain computation	Gradient	Gradient
mm to pixel conversion	1 mm=0.0396 pixel	1 mm=0.1217 pixel
Performance analysis		
Spatial resolution	0.990 mm (25 pixel)	5.2331 mm (43 pixel)
Resolution (pixel)	0.0193	0.0737

Table 6.8: Settings used for the DIC measurements on TRIP-780 uniaxial and bulge tests, and performance analysis.

anisotropy behaviour, disclosed, in particular, by a difference of $\sim$ 50 MPa between 0° and 90°, and $\sim$ 20 MPa between 0° and 45° directions respectively. Moreover, mild anisotropy is founded analysing the R-value obtained in Table 6.9.

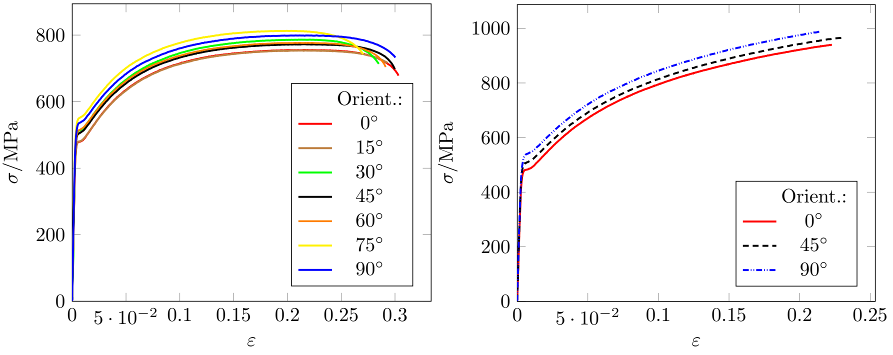

(a) Engineering curve.

(b) True curve.

Figure 6.15: TRIP-780 uniaxial tensile test results on standard specimens obtained at seven different directions with respect to RD.

Analogously to BH-340, the equi-biaxial stress state for TRIP-780 is achieved by means of bulge test equipped with optical stereo-DIC measuring system. Unfortunately, a technical problem occurred during the test that was stopped prematurely before specimen fracture. However, the acquired experimental data are sufficient to calibrate the material model, since both true plastic strains and true equi-biaxial stresses exceed uniaxial data, providing an adequate Plastic

Dir.	0°	15°	30°	45°	60°	75°	90°
σ_Y/MPa	451.2	450.8	509.2	470.2	510.3	545.6	503
R	0.896	0.874	0.883	0.925	0.943	1.059	1.062

Swift Law parameters (at 0° dir.):		
K /MPa	ε_0	n
1343	0.00287	0.229

Table 6.9: Summary of uniaxial test results for TRIP-780.

Work range.

It is worth noting that calculation of R-value from biaxial stress state usually requires to exclude plastic strains up to 3% due to uncertainties errors on determination of curvature in the early stages of dome forming. Nevertheless, the outcoming R_B value computed in Figure 6.16d does not vary significantly even if plastic strains until 5% are discarded, since the majority of points are located between $10 \div 16\%$ of ε_p.

Normalised flow stresses with respect to equi-biaxial stress at the same amount of Plastic Works (Figure 6.17 give also here an idea about how yield surface behaves at large strain, helping to evaluate the amount of Plastic Work whose flow stresses will be used for the calibration. Moreover, displaying flow stresses in the π-plane give an insight about the overall material nature, which for the considered TRIP-780 clearly results mildly anisotropic.

Therefore, all input data for the characterization of TRIP-780 for YLD2000-2D material model, are summarised in Table 6.10 for the selected $W_p = 76$ kJ. Therefore, calibration results are reported in Figure 6.19, assuming that the material exponent of yield surface is $a = 6$, due to BCC structure of TRIP ferrite primary matrix.

Dir.	0°	15°	30°	45°	60°	75°	90°	*Biax.*
σ/σ_B	0.938	0.936	0.970	0.955	0.960	0.999	0.983	1
R	0.896	0.874	0.883	0.925	0.943	1.059	1.062	1.165

Table 6.10: Input data for YLD2000-2D calibration on TRIP-780 steel.

6.3.2 VFM identification procedure

Extending the aforementioned experimental activity on TRIP-780 notched specimen for non-linear VFM identification, also in this case three orientations of material texture are considered from the same blank sheet metal with 1.4 mm thickness. Digital image correlation is realised with the *MatchID* software,

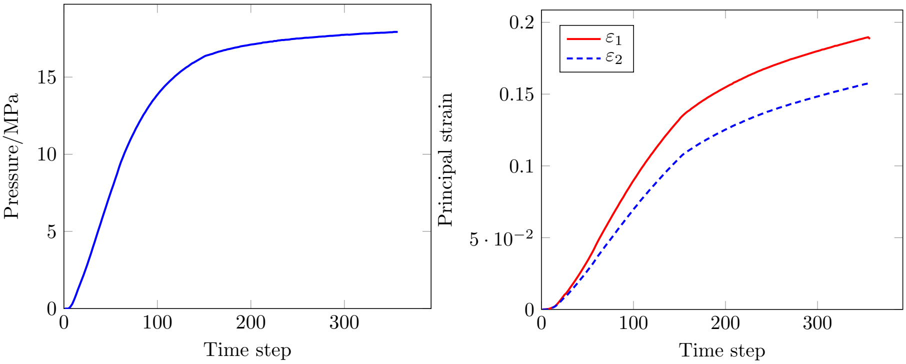

(a) Pressure.

(b) Hencky principal strains.

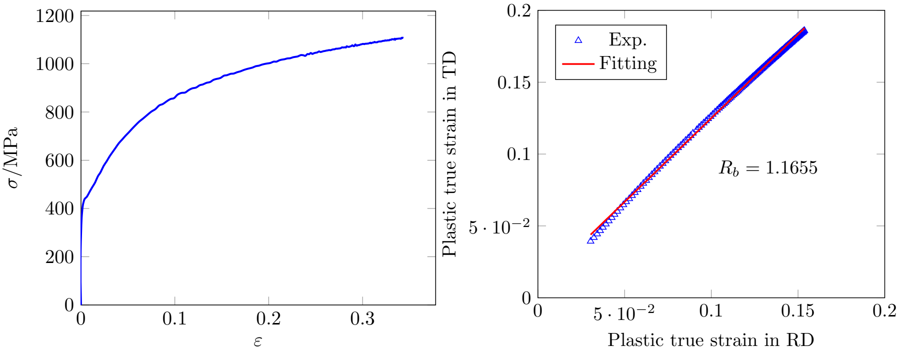

(c) Equibiaxial stress-strein curve.

(d) R-value R_B.

Figure 6.16: Bulge test results and resulting equi-biaxial stress-strain curve and R-value coefficient for TRIP-780.

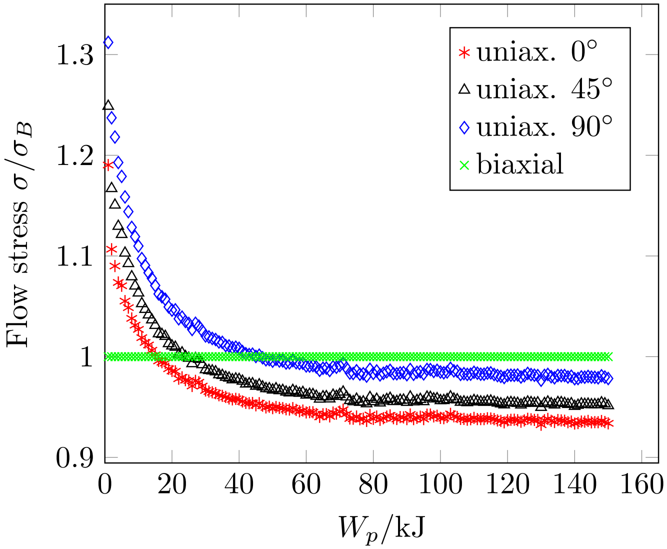

Figure 6.17: Flow stress normalised by the equi-biaxial stress σ_B as function of Plastic Work W_p for TRIP-780.

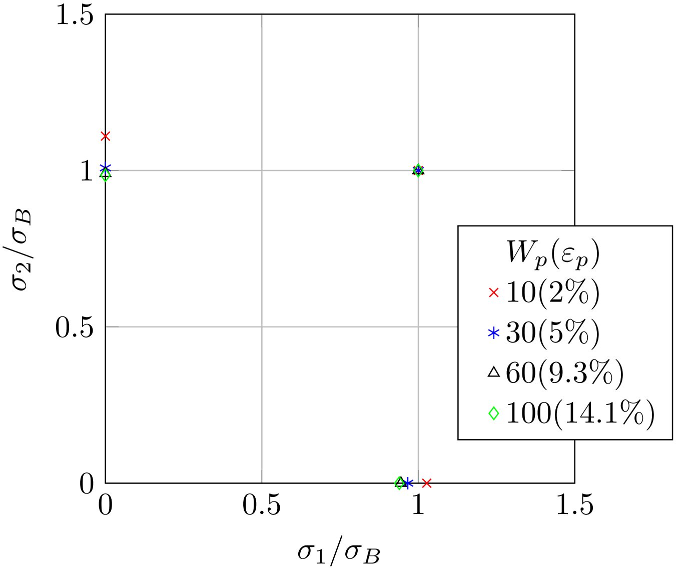

Figure 6.18: TRIP-780 plot on the π-plane of normalised flow stresses calculated at different Plastic Work. Corresponding plastic strain from uniaxial tensile test at 0° is reported in parenthesis.

YLD2000-2D coefficients:	
α_1	1.0203
α_2	1.0310
α_3	1.0610
α_4	1.0209
α_5	1.0301
α_6	0.8157
α_7	1.0273
α_8	1.1346
a	6

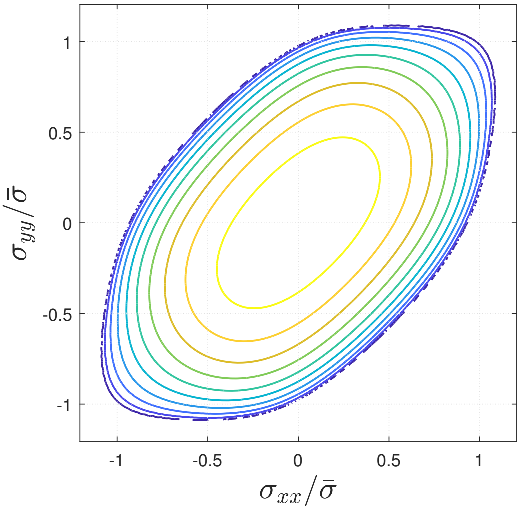

Figure 6.19: Anisotropy coefficients and predicted tricomponent yield surface for TRIP-780 steel.

whose analysis settings and measured resolution are indicated in Table 6.11. A subset of 31 pixels is chosen to guarantee a proper recognition of speckle pattern along the loading path, while the step size is selected to 5 pixels, such that an AOI of 115 × 271 measurement points for each time step is obtained.

DIC technique	3D correlation
Pre-filtering	Gaussian-Kernel 5
Subset (pixel)	31
Stepsize (pixel)	5
Correlation criterion	ZNSSD
Shape function	Affine
Interpolation function	Bicubic spline
Strain computation	Gradient
Performance analysis	
Spatial resolution	1.0912 mm (31 pixel)
Resolution (pixel)	0.0672

Table 6.11: Settings used for the DIC measurements and performance analysis on TRIP-780 notched specimens.

Strain fields (Figure 6.20) are derived from displacements according to Hencky definition. Also for TRIP steel raw data are submitted to spatial smoothing over 9 measurement points (Figure 6.21), in order to have two strain data fields to employ for VFM and to compare.

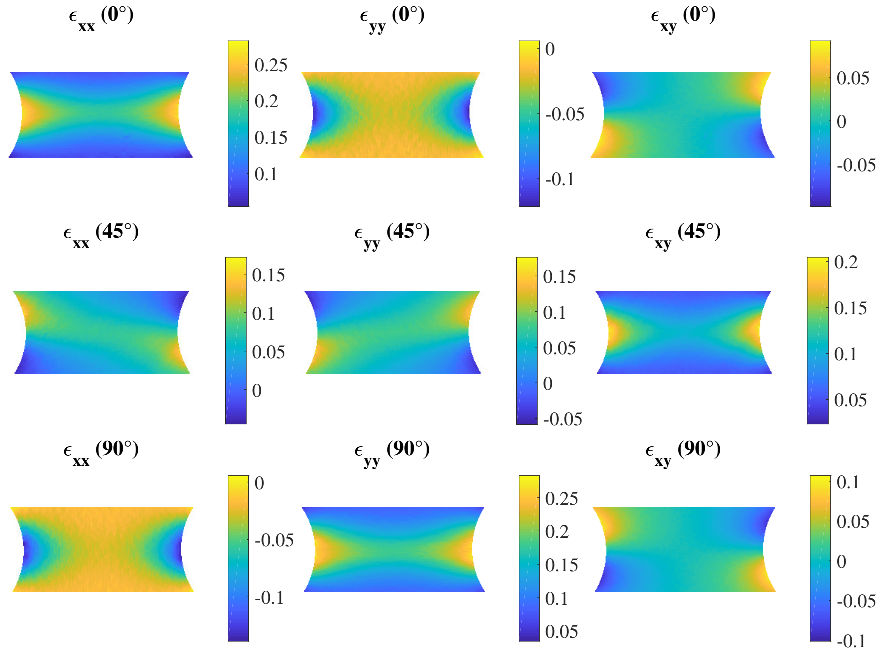

Figure 6.20: Example of measured strain fields on TRIP-780 specimens' surfaces at different material orientations. The reference frame is local.

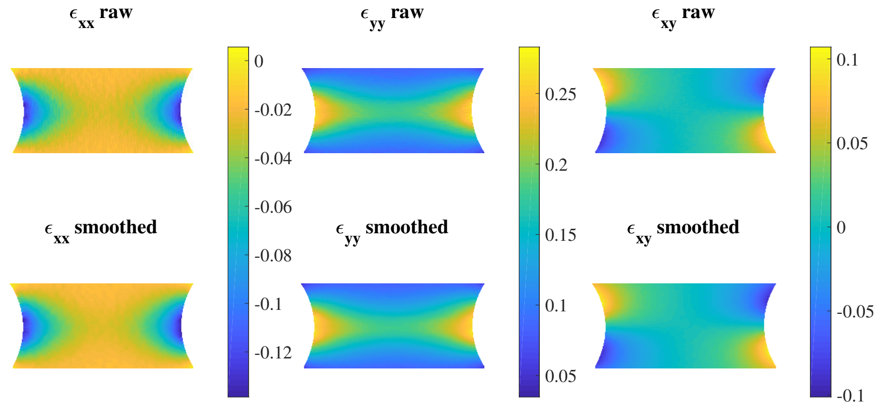

Figure 6.21: Effects of smoothing application on strain fields for TRIP-780 specimen oriented at 90° with respect to RD.

Minimization of VFM cost function is focused on the eight α_i coefficients of YLD2000-2D yield function, get involving 30 time step along the loading path. Also here, initial guess material parameters are taken equal to 1. After 2 h 50 min of computational time, the outcoming of non-linear VFM procedure are listed in Table 6.12.

	Raw data	Smooth. data
α_1	1.0102	1.0212
α_2	1.0127	1.0222
α_3	0.9794	0.9555
α_4	0.9803	0.9868
α_5	1.0148	1.0220
α_6	0.9869	0.9739
α_7	1.0355	1.0437
α_8	1.0886	1.1222
a	6	
	Cost Function score:	
Φ	2193	2270

Table 6.12: Identified YLD2000-2D coefficients with non-linear VFM for TRIP-780.

6.3.3 Comparison of identification results

From the comparison of predicted yield surfaces at σ_{xy} null (Figure 6.22), the ones calculated from VFM identified parameters before and after spatial smoothing predict the same yield stress at RD and TD, while differs at equi-biaxial stress state. At equi-biaxial point, the Yield surface from VFM applied on smoothed data seems to be in accordance with the reference one from standard procedure, nonetheless there is no conformity between them for 0° direction. Anyway, the main discrepancy can be observed for the plane strain stress state.

Nevertheless, observing flow stress prediction capabilities (Figure 6.23a), there is still a lack to cover experimental flow stresses at 0° and 45° with respect to RD. It can be noted that also the YLD2000-2D calibrated with the standard procedure has some difficulties to reach 30° and 75° orientations; in such cases the YLD2004 material model is more suitable compared to YLD2000 [57, 99, 100].

R-value prediction is capable of reproducing the same trend of the reference curve, and there is a difference with experimental values of 0.07, 0.130 and 0.137 at 0°, 45° and 90° respectively.

Albeit the TRIP-780 is a mild anisotropic material, also here the comparison

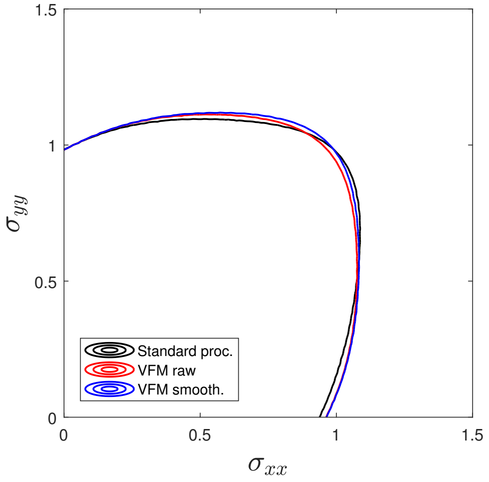

Figure 6.22: Comparison of predicted yield surfaces obtained employing the standard procedure, the VFM on raw and spatially smoothed strain data for TRIP-780. The yield surfaces are normalised by the TD.

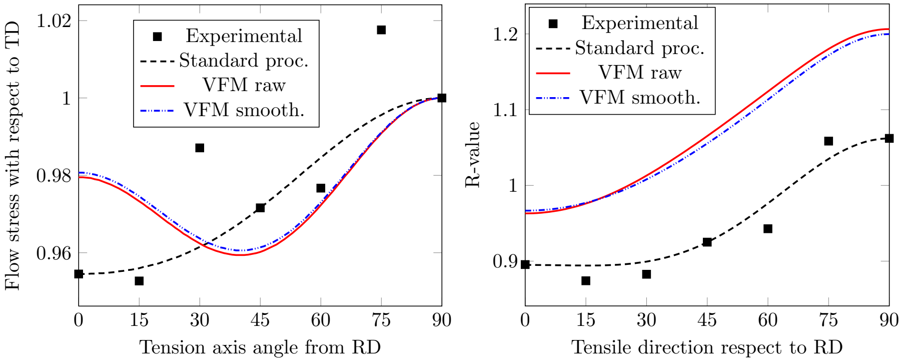

(a)

(b)

Figure 6.23: Comparison of anistropy of uniaxial yield stress with respect to the TD flow stress (a) and of R-value (b) for TRIP-780, measured experimentally and predicted with YLD2000-2D. Characterization is achieved using the standard procedure and also VFM on the two strain data sets. All reported values are normalised by the TD.

of predicted equi-biaxial point offers differences of 1.13% in case of raw strain data employed in the VFM and 0.05% for smoothed strain fields (Table 6.13).

Standard	VFM raw	VFM smooth.
1.0177	1.0037	1.0182

Table 6.13: Comparison of predicted flow stress at the equi-biaxial stress state for TRIP-780.

Chapter 7

Conclusions and future developments

The present thesis relates on the characterization of sheet metal anisotropic plasticity models using the VFM as inverse methodology for identification of material mechanical properties. Such calibration method, when coupled with a full-field measurement technique, offers several advantages compared to other standard procedures. Basically, it permits to gather a lot more of informations about material state from a single test employing specimens capable of generating complex stress states. This can reduce, for instance, the number of required stress to calibrate a complex material model. Moreover, it is inherently faster compared to other inverse identification methods like the Finite Element Model Updating (FEMU), where material parameters identification is achieved by performing iteratively a Finite Element Analysis of the test until numerical results match the experimental data.

However, the non-linear VFM applied procedure on anisotropic plasticity still has some open issues. Since the identification of material properties is achieved by solving a non-linear problem with the minimization of cost function, stress integration algorithm plays a crucial role in both goodness of results and computational time to reach the identification. Secondly, it is strictly dependent from the accuracy of experimental strain data. Missing or wrong data points on the specimen edge and other experimental uncertainties, for example, decisively contributes to the success of model characterization. Furthermore, the identification of complex anisotropic plasticity models is not studied into detail, and those aspects that concern the selection of Virtual Fields, the type and number of tests to employ, and sensitivity to material behaviour represent a challenging research topic.

The aim of this research activity, thus, is to contribute to the investigation of such problems, deeply analysing the benefits and the drawbacks of non-linear VFM application to characterize anisotropic plasticity behaviour of metals.

VFM, and inverse identification techniques in general, represent a powerful tool thanks to their ability to employ a large amount of material data. Consequently, they offers new suggestion and ideas for experimental procedures development. So, this research activity was also extended in parallel to study new experimental protocols.

In the following, the previous chapters are summarised and discussed.

7.1 The Direct Method for integration of elasto-plastic constitutive equations

The computation of the stress field from the strain history is a well-known problem in elasto-plasticity. The stress depends on a non-linear way on the strain history and, in general, a closed form solution to obtain stress from strain does not exist. The problem is tackled by using numerical algorithms that are basically founded on the determination of incremental stress $\Delta\boldsymbol{\sigma}$ from the incremental strain $\Delta\boldsymbol{\varepsilon}$ using Newton-Raphson iterative schemes. However, their implementation in a wider inverse identification framework is computationally heavy, and their use on experimental data has to face different issues. For instance, submitting too large strain increments can not ensure convergence, requesting then to increase the number of iterations or to decrease the size of strain increments; furthermore, in case of DIC strain measurement data, the Elastic Predictor–Plastic Corrector Methods are strongly sensitive to noise, which has the typical order of magnitude of elastic strain increments.

For this reasons, a new computational algorithm for stress reconstruction from strain data is formalised. This computational method is defined *Direct*, since it permits to retrieve the stress state directly from plastic strain increment exploiting the mutual relation between Plastic Flow Rule and yield surface.

Validation is carried out employing two anisotropic plasticity models, the traditional Hill48 and the advanced YLD2000, both in plane stress condition. Accuracy assessment is made comparing stress and equivalent plastic strain calculated via Direct Method with Finite Element Analysis numerical data, showing proper and accurate results in large strain plasticity. The study about the influence of strain increments exhibits how the proposed algorithm is able to reconstruct the stress state independently from the number of measurement steps during the loading path. This characteristic makes the Direct Method particularly attractive since it can achieve convergence even with a single large plastic increment. In the experimental activity some intrinsic uncertainties affect the strain measurement and cannot be totally eliminated. Therefore, the Direct Method is tested by reproducing numerically noisy strain maps. Also, in this case, the algorithm shows a robust stress integration, especially in case of noise in the range of elastic strain (i.e. $10^{-4}\,\varepsilon$).

Nevertheless, the main drawback of the proposed integration scheme concerns stress calculation when the strain increment is too small. In such case, in fact, the elastic part is not negligible compared to the plastic one, thus the assumption that total strain increment is equal to the plastic strain increment can lead to errors. This condition occurs at early stages of plastic deformation or when increment reduces its size due to incipient unloading phase.

The computational time benchmarking represents, also, another important characteristic. In this case the comparison involves two programming languages that are widely diffused in industrial and academic fields, the high level language MATLAB® and the lower *Fortran95*. For both, implementation of Direct Method algorithm considerably reduces computational time, showing a clear independence from strain increment size.

Under the presented results, in this thesis work all stress calculations in the VFM inverse method involve the Direct integration scheme.

7.2 Development and validation of new experimental protocols

Chapter 5 reports a quite wide research activity, which main goal is represented by the design and the evaluation of new testing protocols for material inverse identification. Moreover, all experimental procedures have the common employment of Digital Image Correlation as full-field measurement technique.

Nowadays DIC is widely used in many experimental applications, and it is capable of accurately measuring shape changes in both 2D and 3D cases. However, it can only trace and measure displacements fields on the surface of the sample during the test, while the informations in the bulk of material are inaccessible. For this reason the Internal Mesh Generation Method (IMG) is proposed. Basically, the method creates nodal points regularly distributed involving an interpolation method based on Bézier curves. When large deformation occurs, the position of such nodal points changes, according to surface displacement field. In this way, in fact, it is possible to evaluate the strain localization that occurs in metal specimens subjected to plastic deformation, hence allowing to get a better insight of phenomena like necking initiation and fracture propagation.

Here, the IMG method is applied on a standard cylindrical specimen, approaching the analysis first on numerical data, then on a real experiment. The former investigation was conducted on a numerical model whose anisotropic behaviour of material is described by the Hill48 model, finding a good agreement in terms of positioning prediction, with an average error of 0.09 mm.

Hence, the IMG method is a applied in a real test. For this propose, a special 360° DIC set-up is used. Speaking strictly, this DIC set-up is able to measure the 3D displacement field in the 3D space moving a single camera in a circular sledge. In particular, considering two consecutive images, the stereo-DIC correlation can be performed on their overlapping ROI thanks to an opportune calibration pattern placed on the bottom of specimen.

The method confirms its feasibility on such application. However, some remarks must be pointed out. It is necessary to pre-process displacement data at first, involving interpolation, to ensure a regularly distributed grid of data. So, the measurement must contain a dense distribution of points. Moreover, the IMG method is intrinsically mesh dependent.

The research activity was also implicated in the design of new experimental test for sheet metals through-thickness behaviour that can be employed in identification methods such as the VFM and FEMU. In particular, here, the VFM is used as a diagnostic instrument to assess the feasibility of new testing procedure. Basically, the idea was to extend the Unnotched Iosipescu test to large deformations, considering that the apparatus must contain samples obtained from a thin metal sheet and it must guarantee an adequate field of view for the optical measurement.

So, as first step, a numerical model reproducing the whole testing system was built to determine these aspects: specimen and grips geometrical specifications, the generated stress and strain fields. Moreover, metal sheet anisotropy was described by Hill48 material model.

The considered specimen thickness (2 mm), makes the DIC technique particularly challenging since the full-field measurement must correctly capture the generated strain field. Thus, simulated experiments are employed to observe the effectiveness of DIC results. So, synthetic images are generated starting from a real speckle pattern which size is comparable to the specimen thickness, involving the displacement fields obtained from FEA to deform the reference image.

DIC measurement is applied on this set of synthetic images, and the outcoming strain maps display measurement problems in proximity of borders. So, a practical way to deal with this mismatching, without compromising the equilibrium, is to substitute wrong measurement points with the closer correct ones.

Therefore non-linear VFM is used to identify the Hill48 parameter that regulates the through-thickness shear behaviour. Comparing identification results with the reference one that is inserted in the FEA simulation, the following conclusions can be pointed out: an exact measurement of strain fields on specimen edge can strongly distort the identification results, however, their correction (when it is possible) can effectively help to improve identification outcomes.

Also, the investigation is extended to evaluate the stress state at different values of specimen's width by means of numerical simulations on 3D model. In fact, the initial width of 5 mm makes the stress state closer to the plane strain condition, which makes the proposed experimental protocol more suitable to the FEMU identification. However, reducing the width to 2 mm (as the specimen's thickness) makes the stress state closer to the plane stress, and, thus, to be employed with the non-linear VFM. As future development, the proposed experimental protocol must be verified in a real test in order to have a final response on its feasibility.

The final section of Chapter 5 is dedicated to the experimental validation of a former study. Here, a numerical simulator based on non-linear VFM is built to optimize the geometry of specimens involved in the identification of hardening behaviour through VFM. The peculiarity of this numerical procedure lies within the fact that 2D DIC measurement chain is numerically reproduced in the simulated experiment, including experimental uncertainties as noise, out-of-plane movements and variable lighting conditions. Also here, the VFM is employed as diagnostic tool, with the aim to improve the DIC experimental set-up; specifically, all inserted specimen's geometries are classified according to their identified hardening curve.

Three geometries with antipodal identification scores are selected from this first numerical study. Then, an experimental campaign is performed to validate predictions of the aforementioned optimization protocol. In order to have a statistical significance, 9 specimens for each geometry are obtained from the same blank of AISI304 steel. Hence, the strain fields measured with DIC are submitted to VFM, and their identification performances are evaluated in terms of RMSE error, which is compared to the reference hardening curve calibrated from uniaxial tensile specimen. Observing the results, all three geometries display a good accuracy until 2% of equivalent plastic strain. However, when equivalent plastic strain increases, the geometry with the worst score from the numerical analysis displays an higher error and larger standard deviation of results; on the other hand, the best designed configuration demonstrates to have the most robust results, confirming the simulator outcoming predictions.

This successful experimental validation opens the door to the application of this numerical protocol to several problems. First, this geometrical optimization procedure can be improved by implementing more sophisticated optimization algorithms, such as Genetic Algorithms or the Simplex Method. Moreover, since in this study the isotropic behaviour of material is assumed, a natural further development is represented by considering anisotropic plasticity models.

7.3 Identification of anisotropic plasticity models: the YLD2000-2D

The aim of Chapter 6 is to provide a detailed experimental activity to investigate capabilities of VFM to identify the constitutive parameters of an advanced linear transformation-based anisotropy yield function: the YLD2000-2D. In particular, the non-linear VFM procedure is compared to the standard calibration protocol, which is used as touchstone for the prediction of material behaviour. The study is carried out on two AHSS steels, the BH340 and TRIP 780, largely employed in automotive industry for body and structural parts making.

According to the standard procedure, the calibration of the eight α_i material parameters requires the employment of equi-biaxial stress state. In this case, the latter is achieved by means of hydraulic bulge test.

On the other side, the VFM is performed involving the strain fields obtained from tensile test on double notched specimens cut at three different material orientations. Moreover, three Virtual Fields are manually introduced for the identification, following the common stiffness-based selection of Virtual Fields.

The VFM, fed by heterogeneous strain fields from notched specimens at three different directions, is able to calibrate the YLD2000-2D model. However, there are some differences in the prediction of flow stress tensile properties, whose maximum deviations are relatively small (4% for the BH-340 and 2.6% for TRIP-780 considering the 0°). Such notched specimens do not provide data from the equi-biaxial stress state; albeit both tested materials do not have a strong anisotropy, identified parameters by means of VFM predict an equi-biaxial yield stress that is similar to the one obtained from the standard calibration procedure.

Also, the parameters calibrated with VFM are capable to reproduce the R-value experimentally measured trend, however, a maximum difference of 7% and 12% is found for BH340 and TRIP780 respectively. Spatial smoothing can help to improve the accuracy of results, however, more efforts must be devoted to improve the strain measurement, especially along the notches' edges, where strain magnitude is higher. Secondly, the VFM uses an heterogeneous strain field to identify the material parameters, whose impacts on each parameter is not still investigated. This actually motivates more the implementation of automatically generated Virtual Fields based on the parameters' stress sensitivity [50].

Finally, a further consideration must be pointed out. The VFM represents an incredibly powerful tool, that is also very attractive for industrial applications, since it permits to reduce the number of tests required to characterize even complex material models. Nonetheless, the reduction of tests limits its potentiality. So, as future development, the non-linear VFM cost function can be improved by including additional experimental data as, for instance, plane strain state, pure shear, and even the equi-biaxial stress state from bulge test.

Bibliography

[1] Y.-M. Deng and K.L. Edwards. The role of materials identification and selection in engineering design. *Materials & Design*, 28(1):131–139, 2007.

[2] M. Rossi, G.B Broggiato, and S. Papalini. Application of digital image correlation to the study of planar anisotropy of sheet metals at large strains. *Meccanica*, 43:185–199, 2008.

[3] S. Coppieters, S. Cooreman, H. Sol, P. Van Houtte, and D. Debruyne. Identification of the post-necking hardening behaviour of sheet metal by comparison of the internal and external work in the necking zone. *Journal of Materials Processing Technology*, 211(3):545–552, 2011.

[4] S. Avril, M. Bonnet, A.-S. Bretelle, M. Grédiac, F. Hild, F. Ienny, F. Latourte, D. Lemosse, P. Pagano, E. Pagnacco, and F. Pierron. Overview of identification methods of mechanical properties based on full-field measurements. *Experimental Mechanics*, 48(381-402), 2008.

[5] H. E. Tresca. Mémoire sur l'écoulement des corps solids. In *Mémoire Présentés par Divers Savants*, pages 75–135. Acad. Sci. Paris, 1872.

[6] R. von Mises. Mechanik der plastischen formünderung von kristallen. *ZAMM*, 8:161–185, 1928.

[7] J. Chakrabarty. *Theory of Plasticity.* Elsevier Butterworth-Heinemann, 3 edition, 2006.

[8] A. Anandarajah. *Computational Methods in Elasticity and Plasticity.* Springer-Verlag New York, 1 edition, 2010.

[9] W. Han and B. D. Reddy. *Plasticity: mathematical theory and numerical analysis*, volume 9 of *Interdisciplinary applied mathematics.* Springer, 2 edition, 2012.

[10] Jacek J. Skrzypek and Artur W. Ganczarski. *Mechanics of anisotropic materials.* Springer, 2015.

[11] D. Banabic. *Sheet Metal Forming Processes.* Springer, 2010.

[12] Dorel Banabic. *Multiscale modelling in sheet metal forming.* ESAFORM Bookseries on Material Forming. Springer, 2016.

[13] W. Prager. Recent developments in the mathematic theory of plasticity. *Journal of Applied Physics*, 20(3):235–241, 1949.

[14] W. Prager. The theory of plasticity - a survey of recent achievements. *Proc. Inst. Mech. Eng.*, 169:41, 1955.

[15] G. Broggiato, F. Campana, and L. Cortese. The chaboche nonlinear kinematic hardening model: calibration methodology and validation. *Meccanica*, 43:115–124, 2008.

[16] F. Yoshida and T. Uemori. A model of large-strain cyclic plasticity describing the Bauschinger effect and workhardening stagnation. *International Journal of Plasticity*, 18(661-686), 2002.

[17] F. Barlat, J.J. Gracio, M.-G. Lee, E.F. Rauch, and G. Vincze. An alternative to kinematic hardening in classical plasticity. *International Journal of Plasticity*, 27:1309–1327, 2011.

[18] R. Hill. A theory of yielding and plastic flow of anisotropic metals. *Proceedings of the Royal Society of London. Series A, Mathematical and Physical Sciences*, 193(1033):281–297, 1948.

[19] W. T. Lankford, S. C. Snyder, and J. A. Bausher. New criteria for predicting the press performance of deep drawing sheets. *Trans. Am. Soc. Metals*, 42:1197–1232, 1950.

[20] F. Barlat, Brem J.C., J.W. Yoon, K. Chung, R.E. Dick, D.J. Lege, F. Pourboghrat, S.H. Choi, and E. Chu. Plane stress yield function for aluminum alloy sheets — part 1: theory. *International Journal of Plasticity*, 19:1297–1319, 2003.

[21] R.W. Logan and W.F. Hosford. Upper-bound anisotropic yield locus calculations assuming <111>-pencil glide. *International Journal of Mechanical Sciences*, 22:419–430, 1980.

[22] J.W. Yoon, F. Barlat, R.E. Dick, K. Chung, and Kang T.J. Plane stress yield function for aluminum alloy sheets — part ii: FE formulation and its implementation. *International Journal of Plasticity*, 20:495–522, 2004.

[23] K. Chung, M.-G Lee, D. Kim, C. Kim, M.L. Wenner, and F. Barlat. Spring-back evaluation of automotive sheets based on isotropic-kinematic hardening laws and non-quadratic anisotropic yield functions part i: theory and formulation. *International Journal of Plasticity*, 21:861–882, 2005.

[24] J.W. Yoon, F. Barlat, R.E. Dick, and M.E. Karabin. Prediction of six or eight ears in a drawn cup based on a new anisotropic yield function. *International Journal of Plasticity*, 22:174–193, 2006.

[25] S. Coppieters and T. Kuwabara. Identification of post-necking hardening phenomena in ductile sheet metal. *Experimental Mechanics*, 54:1355–1371, 2014.

[26] M. Rossi, F. Pierron, and M. Štamborská. Application of theVirtual Fields Method to large strain anisotropic plasticity. *International Journal of Solids and Structures*, 97-98:322–335, 2016.

[27] F. Dunne and N. Petrinic. *Introduction to Computational Plasticity.* OUP Oxford, 2006.

[28] M. Ortiz and J.C. Simo. An analysis of new class of integration algorithms for elastoplastic constitutive relations. *International Journal for Numerical Methods in Engineering*, 23:353–366, 1986.

[29] J.W. Yoon, D.Y. Yang, K. Chung, and F. Barlat. A general elasto-plastic finite element formulation based on incremental deformation theory for planar anisotropy and its application to sheet metal forming. *International Journal of Plasticity*, 15:35–67, 1999.

[30] J.W. Yoon, D.Y. Yang, and K. Chung. Elasto-plastic finite element method based on incremental deformation theory and continuum based shell elements for planar anisotropic sheet materials. *Computer Methods in Applied Mechanics and Engineering*, 174:23–56, 1999.

[31] M. Ortiz and E.P. Popov. Accuracy and stability of integration algorithms for elastoplastic constitutive equations. *International Journal for Numerical Methods in Engineering*, 21:1561–1576, 1985.

[32] M.L. Wilkins. *Calculation of elasto-plastic flow.* University of California Lawrence Radiation Laboratory, 1963.

[33] J. Lee, M.-G. Lee, F. Barlat, and J. H. Kim. Stress integration schemes for novel homogeneous anisotropic hardening model. *Computer Methods in Applied Mechanics and Engineering*, pages 73–92, 2012.

[34] J. Lee, D. Kim, H.J. Bong, F. Barlat, and M.-G. Lee. Stress update algorithm for enhanced homogeneous anisotropic hardening model. *Computer Methods in Applied Mechanics and Engineering*, 286:63–86, 2015.

[35] M. Rossi and F. Pierron. Identification of plastic constitutive parameters at large deformations from three dimensional displacement fields. *Computational Mechanics*, 49:53–71, 2012.

[36] A. Gorry. General least-squares smoothing and differentiation by the convolution (Savitzky-Golay) method. *Anal. Chem.*, 62:570–573, 1990.

[37] D. Banabic, H.-J Bunge, Pöhlandt, and A.E. Tekkaya. *Formability of metallic materials.* Springer Berlin, 2000.

[38] Isaac Armidror. Scattered data interpolation methods for electronic imaging systems: a survey. *Journal of Electronic Imaging*, 11(2):157–176, 2002.

[39] A. Güner, C. Soyarslan, A. Brosius, and A.E. Tekkaya. Characterization of anisotropy of sheet metals employing inhomogeneous strain fields for Yld2000-2d yield function. *International Journal of Solids and Structures*, 49:3517–3527, 2012.

[40] J. Kajberg and G. Lindkwist. Characterisation of materials subjected to large strains by inverse modelling based on in-plane displacement fields. *International Journal of Solids and Structures*, 41:3439–3459, 2004.

[41] M. Fardmoshiri, M. Sasso, E. Mancini, G. Chiappini, and M. Rossi. Identification of constitutive model parameters in hopkinson bar tests. In *Residual Stress, Thermomechanics & Infrared Imaging, Hybrid Techniques and Inverse Problems*, volume 9 of *Conference Proceedings of the Society for Experimental Mechanics Series*, 2017.

[42] S. Cooreman, D. Lecompte, H. Sol, J. Vantomme, and D. Debruyne. Identification of mechanical material behaviour through inverse modeling and DIC. *Experimental Mechanics*, 48(4):421–433, 2008.

[43] M. Meuwissen, Oomens, F. C., Baaijens, R. Petterson, and J. Janssen. Determination of the elasto-plastic properties of aluminium using a mixed numerical–experimental method. *Journal of Materials Processing Technology*, 75:204–211, 1998.

[44] E. Florentin and G. Libineau. Using constitutive equation gap method for identification of elastic material parameters: technical insights and illustrations. *International Journal on Interactive Design and Manufacturing*, 5:227–234, 2011.

[45] D. Claire, F. Hild, and S. Roux. A finite element formulation to identify damage fields: The equilibrium gap method. *International Journal for Numerical Methods in Engineering*, 62:189–208, 2004.

[46] Michel Grédiac and François Hild. *Full-field measurements and Identification in Solid Mechanics.* Wiley, 2012.

[47] F. Pierron and M. Grédiac. *The Virtual Fields Method.* Springer, 2012.

[48] M. Grédiac and F. Pierron. Applying the Virtual Fields Method to the identification of elasto-plastic constitutive parameters. *International Journal of Plasticity*, 2005.

[49] T. Guèlon, E. Toussaint, J.B Le Cam, N. Promma, and M. Grédiac. A new characterization method for rubber. *Polymer Testing*, 28:715–723, 2009.

[50] A Marek, F.M. Davies, and F. Pierron. Sensitivity-based virtual fields for the non-linear Virtual Fields Method. *Computational Mechanics*, 60:409–431, 2017.

[51] Oliver Faugeras. *Three-dimensional computer vision: a geometric viewpoint.* MIT Press, 1993.

[52] L. Cortese, T. Coppola, F. Campanelli, F. Campana, and M. Sasso. Prediction of ductile failure in materials for onshore and off-shore pipeline applications. *International Journal of Damage Mechanics*, 23:104–123, 2014.

[53] L. Cortese, F. Nalli, and M. Rossi. A nonlinear model for ductile damage accumulation under multiaxial non-proportional loading conditions. *International Journal of Plasticity*, 85:77–92, 2016.

[54] T. S. Smith, B. K. Bay, and M. M. Rashid. Digital volume correlation including rotational degrees of freedom during minimization. *Experimental Mechanics*, 42:272–278, 2002.

[55] B. K. Bay, T. S. Smith, D. P. Fyhrie, and M. Saad. Digital volume correlation: three-dimensional strain mapping using x-ray tomography. *Experimental Mechanics*, 39:217–226, 1999.

[56] Marco Rossi and Fabrice Pierron. Identifcation of the plastic behaviour in the post-necking regime using a three dimensional reconstruction technique. *Key Materials Engineering*, 504:703–708, 2012.

[57] F. Barlat, H. Aretz, J.W. Yoon, M.E. Karabin, J.C. Brem, and R.E. Dick. Linear transfomation-based anisotropic yield functions. *International Journal of Plasticity*, 21:1009–1039, 2005.

[58] F. Barlat, J.W. Yoon, and O. Cazacu. On linear transformations of stress tensors for the description of plastic anisotropy. *International Journal of Plasticity*, 23:876–896, 2007.

[59] N. Deng, T. Kuwabara, and Korkolis Y.P. Cruciform specimen design and verification for constitutive identification of anisotropic sheets. *Experimental Mechanics*, 55:1005–1022, 2015.

[60] K. Denys, S. Coppieters, M. Seefeldt, and D. Debruyne. Multi-DIC setup for the identification of a 3d anisotropic yield surface of thick high strength steel using a double perforated specimen. *Mechanics of Materials*, 100:96–108, 2016. FEMu inverse methodology.

[61] F. Pierron, G. Vert, R. Burguete, S. Avril, R. Rotinat, and M. Wisnom. Identification of the orthotropic elastic stiffnesses of composites with the Virtual Fields Method: sensitivity study and experimental validation. *Strain*, 43:250–259, 2007.

[62] M. Rossi and F. Pierron. On the use of simulated experiments in designing tests for material characterization from full-field measurements. *International Journal of Solids and Structures*, 49:420–435, 2012.

[63] M. Badaloni, M. Rossi, G. Chiappini, P. Lava, and D. Debruyne. Impact of experimental uncertainties on the identification of mechanical material properties using DIC. *Experimental Mechanics*, 55(8):1411–1426, 2015.

[64] Michele Badaloni. *Optimization and design of tests for material characaterization using simulated experiments.* PhD thesis, KU Leuven / UNIVPM, 2016.

[65] C. Bender and Förstner. Direct solution for computing cylinder from minimal sets of 3d points. *Computer Vision - ECCV 2006*, (135-146), 2006.

[66] P. W. Bridgman. *Studies in large plastic flow and fracture*, volume 177. McGraw-Hill, 1952.

[67] G. Mirone. A new model for the elastoplastic characterization and the stress-strain determination on necking section of tensile spcimen. *International Journal of Solids and Structures*, 41(13):3545–3564, 2004.

[68] K. Genovese, L. Cortese, M. Rossi, and D. Amodio. A 360-deg Digital Image Correlation system for materials testing. *Optics and Lasers in Engineering*, 82:127–134, 2016.

[69] ASTM D5379/D5379M 05 : Standard test method for shear properties of composite materials by the v-notched beam method, 2005.

[70] Fabrice Pierron. Saint-venant effects in the Iosipescu specimen. *Journal of Composite Materials*, 52:61–72, 1998.

[71] F. Pierron and A. Vautrin. Accurate comparative determination of the in-plane shear modulus of t300/914 using the Iosipescu and 45 ° off-axis tests. *Compos. Sci. Technol.*, 52:61–72, 1994.

[72] Fabrice Pierron and Michel Grédiac. Identification of the through-thickness moduli of thick composites from whole-field measurements using the Iosipescu fixture. *Compos Part A: Appl Sci Manufac*, 31(4):309–318, 2000.

[73] M. Kumosa and Y. Han. Non-linear finite-element analysis of Iosipescu specimens. *Composites Science and Technology*, 59(4):561–573, 1997.

[74] P. Lava, S. Cooreman, S. Coppieters, M. De Strycker, and D. Debruyne. Assessment of measuring errors in DIC using deformation fields generated by plastic FEA. *Opt. Laser Eng.*, 47:747–753, 2009.

[75] Y.Q. Wang, M.A. Sutton, H.A. Brook, and H.W. Schreier. Quantitative error assessment in pattern matching: effects of intensity pattern noise, interpolation, strain and image contrast on motion measurements. *Strain*, 45:160–178, 2009.

[76] P. Lava, S. Cooreman, S. Coppieters, M. De Strycker, and D. Debruyne. Study of systematic errors in strain fields obtained via DIC using heterogeneous deformation generated by plastic FEA. *Optics and Lasers in Engineering*, 48:457–468, 2010.

[77] P. Wang, F. Pierron, M. Rossi, P. Lava, and O. Thomsen. Optimized experimental characterization of polymeric foam material using DIC and the Virtual Fields Method. *Strain*, 52(1):59–79, 2016.

[78] Robert G. Keys. Cubic convolution interpolation for Digital Image Processing. *IEEE Transactions on Acoustics, Speech, and Signal Processing*, 29:1153–1160, 1981.

[79] M.A Sutton, J.J. Orteu, and Schreier H.W. *Image correlation for shape, motion and deformation measurements.* Springer, 2009.

[80] S. Avril, M. Grédiac, and F. Pierron. Sensitivity of the Virtual Fields Method to noisy data. *Computational Mechanics*, 34(6):439–452, 2004.

[81] F. Pierron, S. Avril, and V. The Tran. Extension of the virtual fields method to elasto-plastic material identification with cyclic loads and kinematic hardening. *International journal of Solids and Structures*, 47:2993–3010, 2010.

[82] R.H. Byrd, M.E. Hribar, and J. Nocedal. An interior point algorithm for large-scale nonlinear programming. *SIAM Journal on Optimization*, 9(4):877–900, 1999.

[83] N. Suoto, A. Andrade-Campos, and S. Thuillier. Mechanical design of a heterogeneous test for material parameters identification. *International Journal of Material Forming*, 2016.

[84] M. Badaloni, A. Lattanzi, M. Rossi, P. Lava, and D. Debruyne. A simulator to optimize the experimental set-up for elasto-plastic material characterization. In *Conference Proceedings of the Society for Experimental Mechanics Series*, volume 4, pages 97–103, 2017.

[85] M. Rossi, F. Barlat, F. Pierron, M. Sasso, and A. Lattanzi. Identification of the Yld2000-2d model with the Virtual Fields Method. In *Conference Proceedings of the Society for Experimental Mechanics Series*, volume 9, pages 51–57, 2016.

[86] N. Suoto, S. Thuillier, and A. Andrade-Campos. Design of an indication to characterize and classify mechanical tests for sheet metals. *International Journal of Mechanical Sciences*, 101-102:252–271, 2015.

[87] J.H. Kim, F. Barlat, F. Pierron, and M.G. Lee. Determination of anisotropic plastic constitutive parameters using the Virtual Fields Method. *Experimental Mechanics*, 54:1189–1204, 2014.

[88] F. Pierron, S. Avril, and V. The Tran. Extension of the Virtual Fields Method to elasto-plastic material identification with cyclic loads and kinematic hardening. *International Journal of Solids and Structures*, 47:2993–3010, 2009.

[89] J. Fu, F. Barlat, and J.-H. Kim. Parameter identification of the homogeneous anisotropic hardening model using the Virtual Fields Method. *International Journal of Material Forming*, 2015.

[90] M.O. Andar, T. Kuwabara, S. Yonemura, and A. Uenishi. Elastic–plastic and inelastic characteristics of high strength steel sheets under biaxial loading and unloading. *ISIJ International*, 50(4):613–619, 2010.

[91] Y. Yu, Z. Yang, J. Chen, and D.O. Northwood. Numerical simulation of press forming of an automotive body structural component using St13 and BH340 steel sheets. In *WIT Transactions on the Built Environement*, number 112, pages 53–62, 2010.

[92] G. Gutsher, H.-C. Wu, G. Ngaile, and T. Altan. Determination of flow stress for sheet metal forming using the viscous pressure bulge (vpb) test. *Journal of Materials Processing Technology*, 146:1–7, 2004.

[93] J.Y. Lee, F. Barlat, R.H. Wagoner, and M.G. Lee. Balanced biaxial testing of advanced high strength steels in warm conditions. *Experimental Mechanics*, 53:1681–1692, 2013.

[94] ISO 16808:2014 : Determination of biaxial stress-strain curve by means of bulge test with optical measuring systems, 2014.

[95] F. Barlat, Y. Maeda, K. Chung, M. Yanagawa, J. C. Brem, Y. Hayashida, D. J. Lege, K. Matsui, S. J. Murtha, S. Hattori, R. C. Becker, and S. Makosey. Yield function development for aluminium alloy sheets. *Journal of the Mechanics and Physics of Solids*, 45(11/12):1727–176, 1997.

[96] F. Barlat, R. C. Becker, Y. Hayashida, Y. Maeda, M. Yanagawa, K. Chung, J. C. Brem, D. J. Lege, K. Matsui, S. J. Murtha, and S. Hattori. Yielding description for solution strengthened aluminium alloys. *International Journal of Plasticity*, 13(4):385–401, 1997.

[97] M. Rossi, P. Lava, F. Pierron, D. Debruyne, and M. Sasso. Effect of DIC spatial resolution, noise and interpolation error on identification results with the vfm. *Strain*, 51:206–222, 2015.

[98] M. Rossi, M. Sasso, G. Chiappini, D. Amodio, and F. Pierron. Performance assessment of inverse methods il large strain plasticity. In *Conference Proceedings of the Society for Experimental Mechanics Series*, volume 8, pages 259–265, 2014.

[99] S.C. Soare and F Barlat. A study of the Yld2004 yield function and one extension in polynomial form: a new implementation algorithm, modeling range, and earing predictions for aluminum alloy sheets. *European Journal of Me*, 30:807–819, 2011.

[100] F. Grytten, B. Holmedal, O.S. Hopperstad, and Borvik T. Evaluation of identification methods for Yld2004-18p. *International Journal of Plasticity*, 24:2248–2277, 2008.

Vita Auctoris

Personal

Name Attilio Lattanzi

Date of Birth 16 June 1989

Place of Birth San Benedetto del Tronto (AP), Italy

Citizenship Italian

Education

Ph.D. in Industrial Engineering Università Politecnica delle Marche
2014 - 2017

M.D. in Mechanical Engineering Università Politecnica delle Marche
Final grade mark: 110/110 magna cum laude
2011 - 2014

B.D. in Mechanical Engineering Università Politecnica delle Marche
2007 - 2011

Scientific certificate Liceo Scientifico *G. Peano*, Nereto (Italy)
2002 - 2007

Awards

- *AIAS Juniores Award 2016*

List of publications

The research activity done during the three years of doctorate brought the following publications:

International Journals:

- M. Rossi, A. Lattanzi, F. Barlat. A general linear method to evaluate the hardening behaviour of metals at large strain with full-field measurements. *Strain*, Article in press, 2018.
- M.Rossi, L. Cortese, K. Genovese, A. Lattanzi, F. Nalli, F. Pierron. Evaluation of volume deformation from surface DIC measurement. *Experimental Mechanics*, Article in press, 2018.

International Conference Proceedings:

- M. Badaloni, A. Lattanzi, M. Rossi, P. Lava, D. Debruyne. A simulator to optimize the experimental set-up for elasto-plastic material characterization. In *Conference Proceedings of the Society for Experimental Mechanics Series*, volume 4, pages 97-103, 2017.
- M. Rossi, F. Barlat, F. Pierron, M. Sasso, A. Lattanzi. Identification of the YLD2000-2D model with the Virtual Fields Method. In *Conference Proceedings of the Society for Experimental Mechanics Series*, volume 9, pages 51-57, 2016.

National Conference Proceedings:

- A. Lattanzi, M. Rossi, D. Amodio. Un rapido modello computazionale per l'integrazione della tensione a partire da dati di deformazione in condizioni generiche di plasticità. 46° *Convegno Nazionale AIAS*, 6-9 Settembre 2017, Pisa, Italia.
- M. Rossi, A. Lattanzi. Un rapido modello computazionale per l'integrazione della tensione a partire da dati di deformazione in condizioni generiche

di plasticità. 46° *Convegno Nazionale AIAS*, 6-9 Settembre 2017, Pisa, Italia.

- A. Lattanzi, M. Badaloni, L.M. Mattucci. Ottimizzazione di provini per l'identificazione del comportamento elasto-plastico di lamiere tramite il Virtual Fields Method e la Correlazione Digitale di immagini. 45○ *Convegno Nazionale AIAS*, 7-10 Settembre 2016, Trieste, Italia.
- M. Rossi, A. Lattanzi, D. Amodio, A. Angelini. Sviluppo di un sistema di prova per lo studio del comportamento a taglio di lamiere lungo lo spessore. 45° *Convegno Nazionale AIAS*, 7-10 Settembre 2016, Trieste, Italia.
- M.Badaloni, A. Lattanzi. Sugli effetti dei cambiamenti di luce nella caratterizzazione di materiali tramite tecnica DIC. 44° *Convegno Nazionale AIAS*, 2-4 Settembre 2016, Messina, Italia.
- A. Lattanzi, M.Badaloni. Identificazione di modelli avanzati di plasticità anisotropa mediante il virtual fields method. 44° *Convegno Nazionale AIAS*, 2-4 Settembre 2016, Messina, Italia.